UNIVERSITÀ DEGLI STUDI DI BRESCIA

DOTTORATO DI RICERCA IN TECHNOLOGY FOR HEALTH

settore scientifico disciplinare

(Ing-Inf/06)

CICLO

XXXV

TITOLO TESI

CONTRAST-ENHANCED MICRO-COMPUTED TOMOGRAPHY AND IMAGE PROCESSING INTEGRATED APPROACH FOR MICROSTRUCTURAL ANALYSIS OF BIOLOGICAL SOFT FIBROUS TISSUES

NOME DEL DOTTORANDA

FATEHIA BUSHARA GARMA BUSHARA

NOME DEL SUPERVISORE

Prof. NICOLA FRANCESCO LOPOMO

Prof. ALBERTO SIGNORONI

2023

DEDICATION

I dedicate my thesis to my family and many friends.

A special feeling of gratitude to my loving parents: Bushara Garma and

Hikmet Mohamed Ahmed whose words of encouragement.

My sister Fawzia and my brother Mohamed have never left my side, and my aunt Omalhassan Mohamed Ahmed.

For dear husband Amgad who has been such a supportive and kind person. Thank you with all of my heart.

I also dedicate this dissertation to my best friends who have supported me throughout the process: Maha Almoona, Arwaa AlaaEldeen, and Alaa Ali.

I dedicate this work and give special thanks to my teachers.

ACKNOWLEDGEMENT

ABSTRACT

In the musculoskeletal system, tendons and ligaments play an important role in ensuring mobility and stability. These tissues are primarily composed of collagen and present a highly fibrous structure. Highlighting the microstructure components of ligaments and tendons in three-dimensional (3D) images is crucial for extracting meaningful information impacting basic science and orthopaedic applications. In particular, the mechanical properties of the fibrous microstructures are strongly influenced by their volume fraction, orientation, and diameter. However, determining the 3D fibre orientation and diameter is challenging.

In this picture, this thesis aimed at integrating microcomputed tomography (microCT) and image processing approach to identify and enhance microstructural information about biological soft fibrous tissues, including volume and orientation.

The overall procedure was first applied on human hamstring tendon and bovine collateral ligament samples. In a first phase, specific sample preparations – including either a chemical dehydration, or by 2% of phosphotungstic acid (PTA) in water (H_2O) or in 70% ethanol (EtOH) solution – were tested to enhance image contrast of these specific soft tissues. Further, using the scanned data, a novel image processing technique based on 3D Hessian multiscale filter for highlighting fibrous structures was developed to obtain quantitative fibre information. Interestingly, for any strategy of tendon/ligament sample preparation, the proposed approach was adequate for detecting and characterizing fascicle features. The test results showed the fibre arrangement strongly aligned along the main longitudinal direction in the human hamstring tendon more than fibres on the bovine collateral ligament.

Moreover, this technique was further applied in order to determine how the human Anterior Cruciate Ligament (ACL) responds to uniaxial loads with respect to increasing values of strain, considering both a healthy tissue and a one under pathological conditions, i.e., acquired from a patient with osteoarthritis. Also in these cases, the integrated approach was valuable and reliable in identifying orientation and

size of present fascicles and, thus, through a structural mechanical model - based on specific constitutive law - to estimate the elastic modulus of these tissues. In fact, stress-strain curves were estimated, obtaining a value of elastic modulus of 60.8 MPa and 7.7 MPa for the healthy and pathological ACLs, respectively.

In conclusion, a novel contrast enhancement microCT protocol was designed and preliminary validated for the microstructural analysis of biological soft fibrous tissues. In a peculiar application to ACL, the information obtained with the protocol was used to implement a mechanical model of fibrous tissues, thus estimating the biomechanical behaviour of the healthy and pathological tissues.

SOMMARIO

Nel sistema muscolo-scheletrico, tendini e legamenti svolgono un ruolo importante al fine di garantire mobilità e stabilità. Questi tessuti sono composti principalmente da collagene e presentano una struttura altamente fibrosa. Evidenziare i componenti della microstruttura di legamenti e tendini in immagini tridimensionali (3D) è di fondamentale importanza per estrarre informazioni significative che posso avere ripercussioni sulla scienza di base e sulle applicazioni ortopediche. In particolare, le proprietà meccaniche delle microstrutture fibrose sono fortemente influenzate da alcune caratteristiche geometriche, come il volume *fraction*, l'orientamento e il diametro; tuttavia, determinare l'orientamento e il diametro della fibra 3D è impegnativo.

In questa prospettiva, questa tesi mirava ad unire tomografia microcomputerizzata (microCT) ed elaborazione delle immagini in un approccio integrato al fine di identificare e migliorare le informazioni microstrutturali sui tessuti biologici fibrosi, includendo i dati di volume e orientamento.

La procedura complessiva è stata applicata per la prima volta su campioni di tendine del ginocchio umano e su legamento collaterale bovino. In una prima fase, sono state testate preparazioni specifiche del campione, inclusa una disidratazione chimica o preparato di acido fosfotungstico (PTA) al 2 % in acqua (H_2O) o in soluzione di etanolo al 70% (EtOH), così da migliorare il contrasto dell'immagine di questi specifici tessuti. Inoltre, utilizzando i dati scansionati, è stata sviluppata una nuova tecnica di elaborazione delle immagini basata sul filtro 3D hessiano multiscala per evidenziare le strutture fibrose ed ottenere informazioni quantitative sulle fibre. È interessante notare che, per qualsiasi strategia di preparazione del campione di tendini/legamenti, l'approccio proposto è risultato adeguato a rilevare e caratterizzare le proprietà del fascicolo. I risultati del test hanno mostrato che la disposizione delle fibre è fortemente allineata lungo la direzione longitudinale principale nel tendine del tendine, più delle fibre del legamento collaterale bovino.

Inoltre, questa tecnica è stata ulteriormente applicata al fine di determinare come il Legamento Crociato Anteriore (LCA) umano risponda a carichi uniassiali rispetto a valori crescenti di deformazione, considerando sia un tessuto sano che uno in condizioni patologiche, cioè acquisito da un paziente con l'artrosi. Anche in questi casi, l'approccio integrato si è rivelato valido ed affidabile nell'individuare orientamento e dimensione dei fascicoli presenti e, quindi, attraverso un modello meccanico strutturale - basato su specifiche leggi costitutive - nello stimare il modulo elastico di questi tessuti. Sono state infatti stimate le curve sforzo-deformazione, ottenendo un valore di modulo elastico di 60.8 MPa e 7.7 MPa rispettivamente per il LCA sano e patologico.

In conclusione, è stato progettato e validato in via preliminare un nuovo protocollo microCT per il miglioramento del contrasto dedicato all'analisi microstrutturale dei tessuti molli biologici con caratteristiche fibrose. In una peculiare applicazione al LCA, le informazioni ottenute con il protocollo sono state utilizzate per implementare un modello meccanico dei tessuti fibrosi, stimando così il comportamento biomeccanico dei tessuti sani e patologici.

Table of contents

1 INTRODUCTION

1.1 General overview

Ligaments and tendons play a crucial role within the musculoskeletal system [1]. Both these anatomical components are defined as dense fibrous connective tissues that present similar structures but differ in function [2]; ligaments connect bone to bone and provide joint stability [3], whereas tendons connect muscle to bone, and thence are responsible for joint movement [4]. Ligaments and tendons are composed of linearly arranged collagen fibrils assembled into fibers; the fibers are hierarchically organized into fiber bundles, and the bundles into fascicles. Collections of fascicles form the entire tendon or ligament structure [5,6,7]. The bundles are structurally oriented in the axial loading direction of the tissue.

The hierarchical microstructure of ligaments and tendons significantly impacts on their mechanical behavior and inherently defines their physio-pathological function; in this frame, fundamental parameters that are required – among the others - to characterize these structures include fibers diameter and orientation. The measurement of these parameters can be challenging in this context, due to the small dimensional scales and because collagen fibers are distributed extremely close to each other, and therefore high-resolution imaging methods are required [8]. Furthermore, the microstructural organization of these tissues is extremely varied on both local and global scales [9]. Hence, it is highly recommended to use adequate instruments, such as microtomography (microCT), capable of providing a high-resolution imaging approach addressing three-dimensional (3D) volumetric analysis. Furthermore, such an approach could readily be applied to characterize the effect of development, disease, or damage and repair in ligaments and tendons, as well as in collagen-rich tissue-engineering constructs [10].

Although microCT imaging modality is widely used for the study of hard tissues, on the other hand, the visualization of soft tissues is still a challenging matter due to their low X-ray attenuation; in order to solve this issue, in the last decade the use of contrast

agents has been reported as a main solution able to overcome this limitation [11,12,13]. This perspective led to the definition of contrast-enhanced microCT (CE-microCT) approach [14]. However, contrast agents and drying methods have not yet been concurrently investigated on tendon/ligament samples addressing CE-microCT approach.

Therefore, to visualize and quantify differences in the 3D internal structure of tendons and ligaments, we first used microCT imaging to identify key geometrical differences in the arrangement of fascicles within human hamstring tendon (HH) and collateral bovine ligament (CB) that had either been treated through chemical dehydration [15] or 2% of phosphotungstic acid (PTA) staining in two solutions: water (H_2O) and 70% ethanol (EtOH) [16,17]. Thus, the staining with these contrast agents provides 3D visualization of fiber bundles in a tendon and ligament. The resulting scans were evaluated and compared with the corresponding histology sections for the HH tendon.

In addition, ligaments and tendons can adjust to mechanical changes caused by loading, injury, or disease [19]. For example, the microstructure of the anterior cruciate ligament (ACL) is mainly responsible for its mechanical properties. Especially the directional distribution of the fiber system influences the tensile strength [20]. In order to assess both the effects of mechanical tensioning on the ACL microstructure and the influence of the pathology on the tissue response, we used mechanical model mainly based on constitutive laws [21]. Hence, the mechanical behavior of the ACL microstructures under healthy or pathological condition which exposed to specific stress was studied and analyzed based on microCT imaging.

Contrast enhancement usually focuses on sample preparation but working on image acquisition and processing can be a further step to improve the identification of the microstructure of fibrous soft tissues. Indeed, applying a 3D microstructure detection technique on microCT images is crucial for extracting meaningful information impacting basic science and orthopedic applications. In fact, the detection of fascicles is considered challenging in image processing tasks. Several complications arise from

the organization of complex 3D networks, irregular circular structures of varying sizes, and similarity to textured noises. In addition, it becomes more complicated to handle fibers in 3D due to structural issues or computational burdens [22]. Consequently, various scales of local information have been considered when selecting filters that characterize tubular structures (i.e., fibers/fascicles) for low contrast and noisy images. Thus, a 3D Hessian method has been proposed to potentiate structures of interest in several scales to analyze them quantitatively. In addition, several parameters defining fascicles including orientation and diameter, as well as a variety of image analysis algorithms, have been proposed for computing these parameters from microCT data.

Summarizing, the proposed techniques provide improved qualitative and quantitative analysis of the microstructure of tendons and ligaments; this study aimed to propose a novel CE-microCT protocol by (i) comparing phosphotungstic acid (PTA) - as contrast agent specific to highlight collagen fibers with respect to hexamethyldisilazane (HMDS) chemical drying used for sample preparation and (ii) developing an image processing pipeline, for improving image contrast so as to highlight fibrous structural arrangement. Without loss of generality, the protocol was applied on human hamstring tendon and collateral bovine ligament for improved 3D visualization and quantitative microstructural analysis. Moreover, microstructural information obtained through the proposed approach was used to support the deployment of a mechanical model, so as to describe ACL fibers bundle alignment during controlled strain test. In order to further our understanding of the connection between fascicle alignment and the mechanical properties of the ACL, we modelled its behavior under various loads, considering its microstructure, and we proposed an explanation of how the fascicle alignment relates to the mechanical properties of the ACL. It is further worth noting that, we implemented visualization tools in order to clearly analyze and interpret our data, including the maximum intensity projection and an arbitrary cross section of the 3D data.

1.2 The statement of the problem

The hierarchical microstructure of ligaments and tendons plays a critical role in their mechanical behavior and physiological function. To develop accurate mechanical models to describe soft tissue behavior, it is necessary to measure key parameters such as fiber diameter and orientation distribution. MicroCT imaging offers a powerful tool for visualizing and measuring these parameters, but the accurate identification and measurement of individual fibers can be challenging, particularly when fibers are closely distributed relative to the imaging resolution and contrast enhancement protocols. Therefore, the problem to be addressed in this study is to develop an image processing methodology that can reliably identify and measure the diameter and orientation of individual fibers in ligaments and tendons using microCT images. Accurate measurements of these parameters will allow for the development of more precise mechanical models of soft tissue behavior, ultimately improving our understanding of the complex microstructural influences on ligament and tendon function.

1.3 Research motivation

ACL rupture is one of the most severe knee injuries among athletes. The most common treatment is surgical reconstruction with an autografted tendon. Unfortunately, reconstructed knee joints often exhibit different mechanical behaviors to healthy joints. The microstructural differences between the ACL and the graft leads to variation in mechanical performance. Hence, microCT imaging can be used to acquire images of these soft tissues to help in the fibers bundle characterization process. Possible parameters of interest can include fiber diameters and fiber orientation distribution.

1.4 Objectives

The general objective of this work was to develop an integrated approach including experimental and computational methods and algorithms to analyze and quantify microstructure components of tendons and ligaments by exploiting microCT images.

Specific objectives are:

- To propose a CE-microCT protocol for the visualization and quantification of differences in the 3D internal structure of tendons and ligaments (e., orientation and diameter).

- To deploy a specific micromechanical constitutive model based on fiber features, so as to support the analysis of stress-strain relationship under mechanical loading.

- To study the mechanical behavior of fascicles under physiological condition and analyze the pathological influence on tissue mechanical response.

1.5 Novelty of the study

A novel component of this study is the application of CE-microCT protocol to fibrous structures (ligament and tendon) and the development of an image processing pipeline that enhances the contrast of the image in order to highlight fibrous structural arrangement. A mathematical model was also implemented to analyze fiber bundle alignment as a function of strain levels for pathological and healthy ACL microCT images.

1.6 Thesis organization

This project consists of six chapters. Chapter one is an overall introduction to the context and the need the study aim to solve, chapter two gives the state of the art, the theoretical background is reported in chapter three, the research methodology is described in chapter four, whereas the main obtained findings and discussion of these results are given in chapter five; finally, chapter six is devoted for overall conclusions and recommendations for further developments.

2 STATE OF THE ART

2.1 Contrast Enhanced-microCT

In recent years, microCT has become a promising tool for studying the microstructures of soft tissues such as tendons and ligaments. This non-invasive imaging technique provides 3D images of fibrous soft tissues that can be used to qualitatively assess the structure of the tissues themselves and quantify important parameters concerning fibrous structure, like fiber diameter and orientation. However, although this imaging modality has been widely used for the study of hard tissues - e.g., bone - on the other hand, the visualization of soft tissues is still a challenging matter due to their low X-ray attenuation; in order to solve this issue, in the last decade the use of contrast agents has been reported as a feasible solution able to overcome this limitation [11,12,13]. This perspective led to the definition of contrast-enhanced microCT (CE-microCT) [14].

In this picture, scientific literature suggested the use of different approaches, including iodine potassium iodide solution (Lugol's iodine solution - I_2KI), phosphotungstic acid (PTA), phosphomolybdic acid (PMA), and ioxaglic acid (Hexabrix) in different solutions (phosphate buffered saline – PBS, water, ethanol EtOH) as contrast agents for the 3D visualization of soft tissues [16,17,18,23,24,25].

Furthermore, several scientific studies compared the enhancing performance of different agents by applying them on different soft tissues. In Balint et al. the contrast agents I_2KI, PTA, and PMA were evaluated for staining lateral collateral ligaments, medial collateral ligaments and anterior cruciate ligaments in porcine model [16]; this study, however, highlighted that I_2KI staining was able to visualize ligaments in 3D, but was not ideal for individual collagen fibers, and further noticeable shrinkage of tissues could be demonstrated. Disney CM *et al.* studied the intervertebral discs using the I_2KI, PTA, and PMA as a contrast agent. The PTA and PMA have successfully contrasted the collagenous structures, however with incomplete staining penetration, moreover the technique induced macroscopic structural changes [26]. Karhula et al.

focused on the effect of the X-ray attenuation with collagen content using PTA and ioxaglic acid [27], while Ravagli et al. showed the possibility of highlighting fascicles in rat sciatic and pig vagus nerves [28]. According to Sartori et al., PTA can reveal the individual fibers of the tendon when the spatial and contrast resolutions are high enough. In fact, they were able to visualize collagen fiber bundles in an Achilles tendon enthesis stained with demineralized PTA. However, the main limitation of using PTA is tissue shrinkage due to its acidic nature. Thus, the use of such an agent will affect the fibers measurements like thickness or volume in tendon or ligament [23]. An additional strategy for enhancing contrast in soft tissue imaging, alternative to the use of contrast agents, stands in sample drying [14].

However, contrast agents and drying methods have not yet been concurrently investigated on tendon/ligament samples addressing CE-microCT approach. Moreover, contrast enhancement usually focuses on sample preparation, but working on image acquisition and processing can be a further step to improve the identification of the microstructure of fibrous soft tissues.

2.2 Anterior cruciate ligament

Although the ACL injury has been extensively studied, the mechanical behavior of the ACL microstructures has not yet been well explored. The published reports have focused on assessment of changes occurring in the ACL structure as a response to a mechanical stress [10], In a comparative study between the porcine patellar tendon and ACL, the orientation of fascicles relative to their respective longitudinal axes was measured. The results revealed that the fascicles in the patellar tendon were oriented at an angle of approximately 4°, with a standard deviation of 2°. On the other hand, the fascicles in the ACL were found to be oriented at an angle of approximately 24°, with a standard deviation of 10°. These findings, reported in reference [18], provide valuable insight into the structural differences between these two tissues and may have implications for understanding their mechanical properties and function.

Focusing on the importance of microstructure, using X-ray computed tomography with a nanoscale resolution on electrospun poly(caprolactone) nanofiber samples, Chiverton, John P., et al. [8], developed automated measurement techniques based on Hessian filter; the entropy of the orientation distributions was found to be higher in a range of scales for the randomized fiber sample. Further, McLean, James P., et al. [9] proposed an algorithm for quantifying fiber orientation and visualizing it in optical coherence tomography (OCT) images. The method was able to measure dominant fiber orientation more profoundly within the bovine ACL than similar methods. According to Beisbayeva, Zhuldyz, et al. [29], ACL tissue biological and structural directly influence their function. The transmission electron microscopy (TEM) images of injured ACL tissues clearly demonstrated that collagen fibers are regularly arranged in parallel wave patterns along the longitudinal direction. A healthy bovine ACL exhibited an organized collagenous fiber structure. In contrast, an injured one is therefore characterized by an unaligned or aligned randomly along the axis of the tissue. Injuries were associated with a change in collagen fibril diameter distribution in bovine ACL, with a subsequent decrease in average diameter. Fiber diameter distributions of Polycaprolactone (PCL) scaffolds are similar to native and injured ACLs. In addition, they evaluated the mechanical characteristics of healthy ACL tissue by exposing the specimens to increased extensional deformation until failure as well as for the PCL scaffold for aligned and unaligned nanofibers structures.

Chakraborty et al. [30] investigated the stress-strain behavior of the ACL under uniaxial loads applied with various strain rates based on Mooney-Rivlin constitutive model for hyperelastic material and the Prony Series model for a viscoelastic material. Despite this, the study revealed that it was complicated to establish a relationship between Prony series coefficients and strain rates. In contrast, Mooney-Rivlin's five parameter hyperelastic model seems to produce a good correlation between experimental and predicted stress-strain curves.

Wan et. al. [31] developed a three-dimensional finite element model of an intact tibiofemoral joint. In order to investigate the effect of changing the ACL constitutive

model under different joint loads (such as anterior tibial force, varus tibial torque, and valgus tibial torque), three ACL constitutive models were compared. By using different ACL constitutive equations, they found that joint kinematics were affected by both deformation direction and load type.

Based on the assumption that all collagen fibers in the ligament are parallel, De Vita et al. [32] developed a structural constitutive model that correlates the gross mechanical response of the ACL to the collagen fibers' mechanical response. Pioletti et al. [33] developed a biomechanical model based on elastic and viscous potentials. As a result, the constitutive law satisfies thermodynamic principles for large deformations. With human cruciate ligaments and patellar tendons, three parameters - two for elasticity and one for viscosity - were sufficient to accurately fit the non-linear stress-strain curves.

To bridge the gap in this research area we aimed to develop algorithms that are capable of measuring specific features of ACL fascicles, i.e., diameter and orientation, so as to support the analysis of the tissue under physiological and pathological conditions. In particular we tried to deploy and extend the use of the mechanical model proposed by [21].

3 THEORETCAL BACKGROUND

3.1 Introduction

Tendons, ligaments, and joint capsules are three of the most important structures that surround and connect joints. Despite being mechanically passive (i.e., not contracting and producing motion as muscles), each of these structures contributes to joint movement and stability [34].

Ligaments and joint capsules, which connect bones to bones, enhance mechanical stability of joints, guide joint motion, prevent excessive motion, and enhance proprioception. Joint capsules and ligaments act as static restraints. Tendons attach muscles to bones, transmit tensile loads to bones, maintain body posture, and facilitate joint motion. A muscle-tendon unit acts as a dynamic restraint, allowing muscles to be prepositioned at an optimal distance from joints without increasing muscular length [34].

This chapter discusses the following aspects of tendons and ligaments:

- Ligament and tendon structure
- Biomechanical properties of ligament and tendon
- Biomechanical properties and behavior following injury.

3.2 Ligament and tendon structure

As tendons extend from muscle to bone, they transmit the tensile load that is generated by muscular contractions or passive elongation. Additionally, they prevent joints from becoming unstable. Tendons are defined as dense connective tissue. They consist of a collagenous extracellular matrix dominated by parallel fibers and tenocytes, which are metabolically active fibroblasts. A fibril is formed by combining several collagen molecules in a quaternary structure. In this way, organized collagen molecules form units of microfibrils, subfibrils, and fibrils, Figure (3.1). The fibrils join together further to form collagen fibers, which are visible under the light microscope, Figure (3.2). The fibers assemble further into bundles and tenocytes are elongated in rows between these

bundles, which are oriented in the direction of the mechanical load, figure (3.3). Fibril segments can range in length from a few microns to approximately 100 μm with diameters that vary with the shape of the fibril [35]. Fiber bundles are irregular in shape and vary in diameter, ranging from 150 to 500 μm [36].
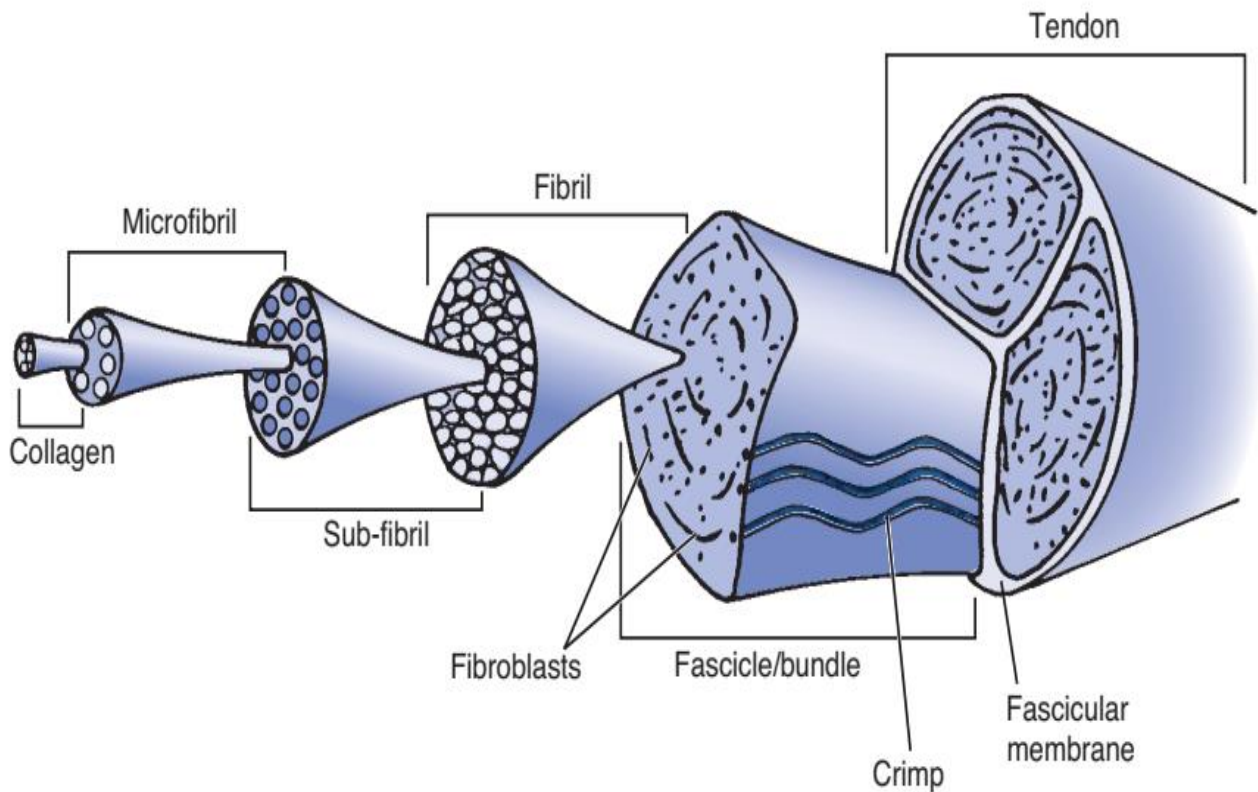

Figure 3. 1: Schematic representation of the microarchitecture of a tendon [34].

During tensile loading, their characteristic undulated shape, called crimp, figure (3.3), allows them to straighten out this wavy configuration [35,37]. These tissues may exhibit nonlinear viscoelastic properties due to the interaction between the crimp and the fibrous extracellular matrix (e.g., toe region of deformation).

Ligaments have the same general composition as tendons with a few key differences, figure (3.4). Similar to tenocytes, ligaments have fibroblasts that are found within the ligament substance aligned with the collagen fibrils, figure (3.5). Like tenocytes, ligamentous fibroblasts also form an extensive network with other cells via cytoplasmic extensions that are linked by gap junctions [34].

The extracellular matrix is also composed mainly of type I collagen, although in contrast to tendons, the fibers are not parallel and are multidirectional, figure (3.3). Most are in line with the axis of the ligament. Although ligaments generally sustain tensile loads in one predominant direction, they may also bear smaller tensile loads in other directions, which suggests that the fibers are interlaced even if they are not completely parallel, figure. (3.3 b). Thus, the specific orientation of the fiber bundles varies to some extent among the ligaments and depends on the specific function of the ligament [39].
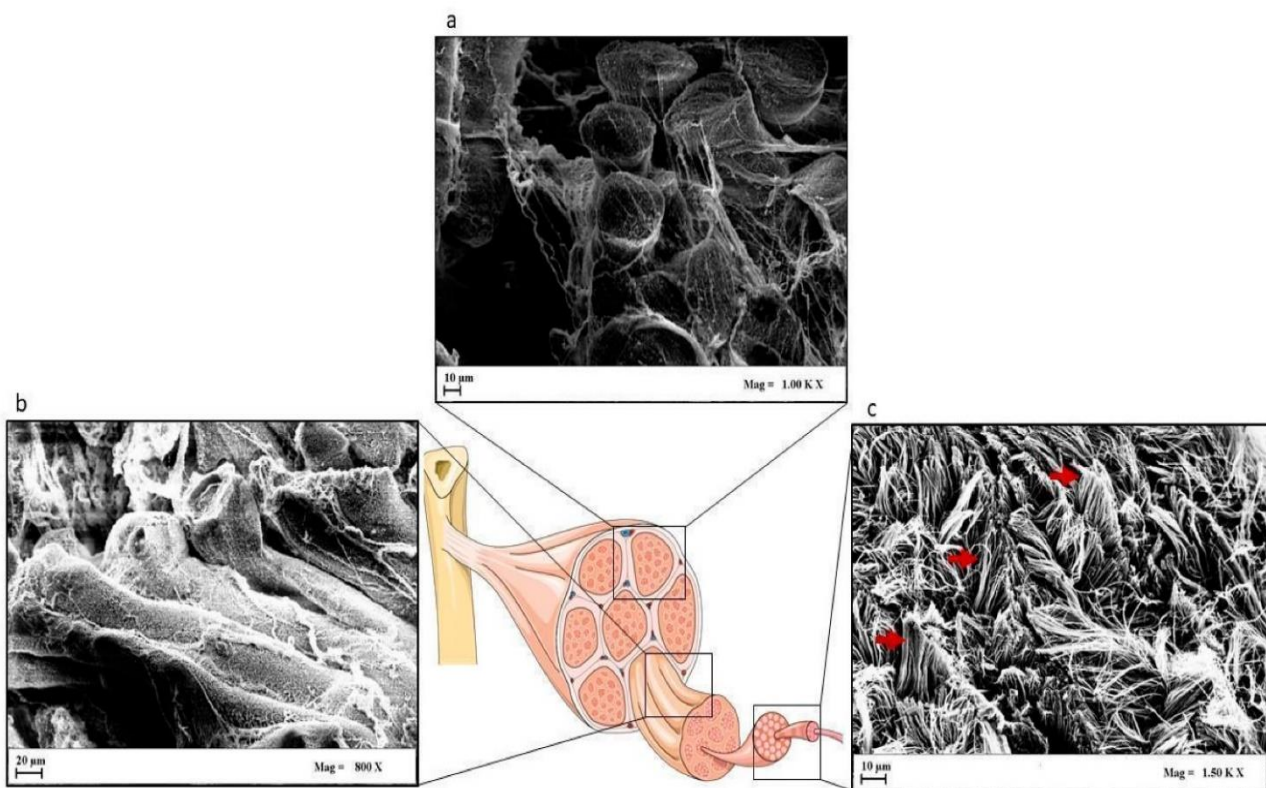
Figure 3. 2: Hierarchical arrangement of the structure of tendons: (a) Scanning electron microscopy (SEM) of a transverse section of collagen fiber bundles (scale bar = 10 μm); (b) SEM image of longitudinal collagen bundles in which their parallel arrangement along the longitudinal axis of the tendon is clearly shown; each collagen bundle is surrounded by the endotenon (scale bar = 20 μm); (c) SEM image that shows the multiple collagen fiber bundles that make up the tendon [38].

Figure 3. 3: Schematic diagram of the structural orientation of the fibers of tendon (A) and ligament (B); insets show longitudinal sections. In both structures the fibroblasts are elongated along an axis in the direction of function. Adapted from [40,34].

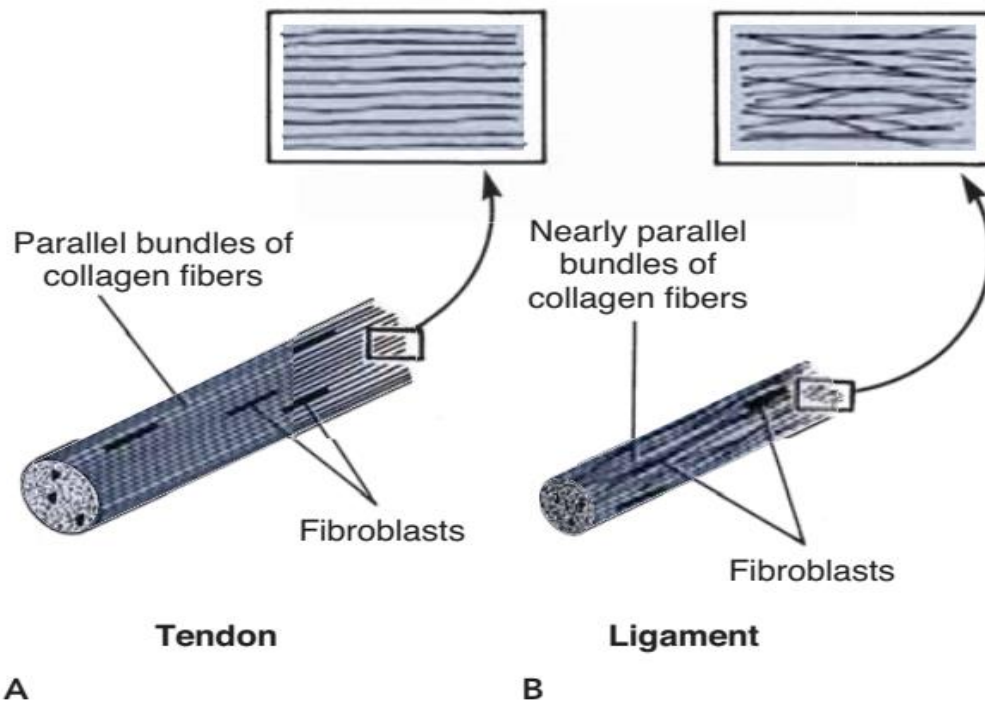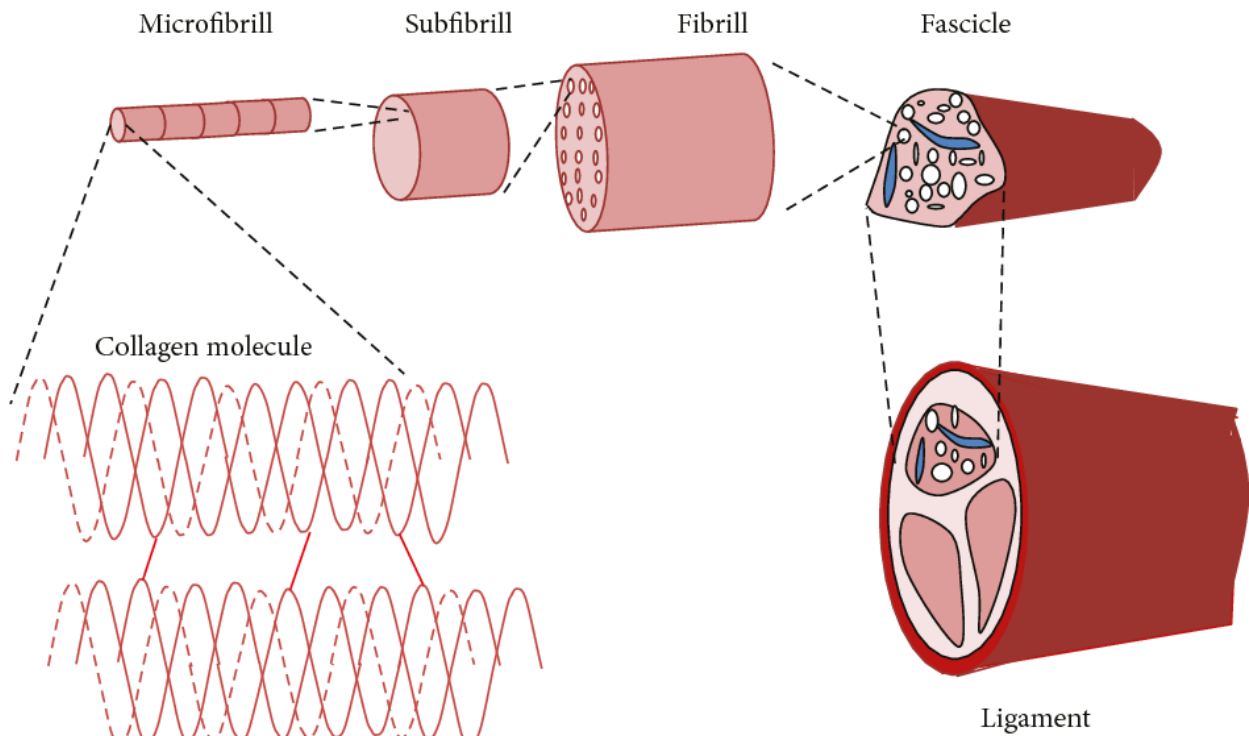Figure 3. 4: Schematic representation of the microarchitecture of a ligament [20].

	Fibres (60–70%)			Ground substances (20–30%)	
	Collagen I	Collagen III	Elastin	Glycosaminoglycans & proteoglycans adhesion proteins	Water
Ligament	70–80%	10%	Varies with ligaments	1–5%	>95%
Tendon	95–99%	1–5%	Values not reported scarce	<2%	<95%
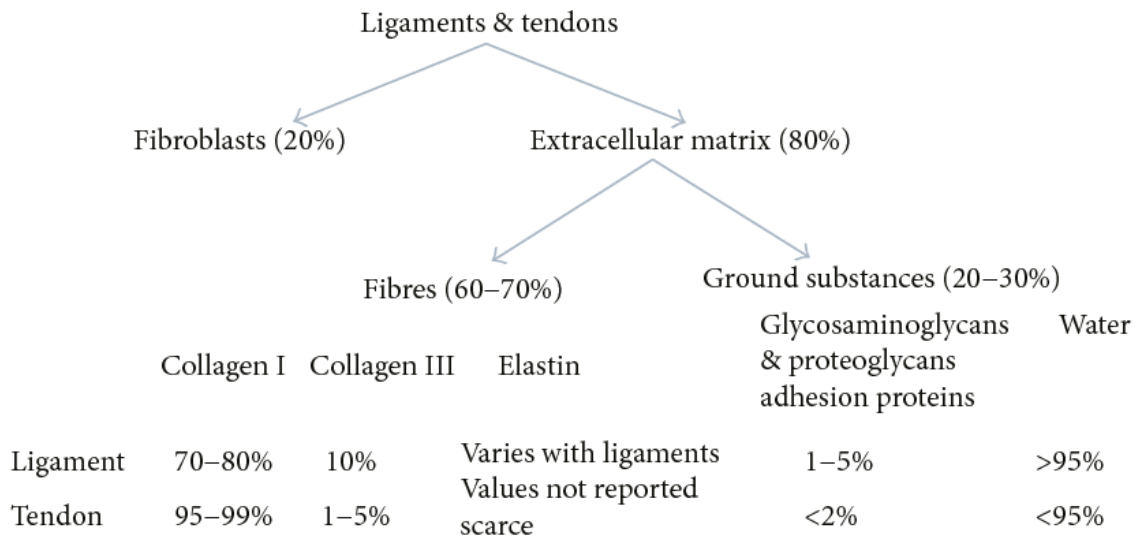
Figure 3. 5: The composition of tendon and ligament [20].

The histology of tendon and ligament is shown in figure (3.6). Under the light microscope, fibrils show a wavy pattern in the resting phase that disappears when stretch forces are applied and resumes to their original configuration after the force is removed [19].

Figure 3. 6: Histology of tendon (A) and ligament (B), The collagen fibers of tendon and ligament are highly aligned [19].

3.3 Biomechanical properties of ligament and tendon

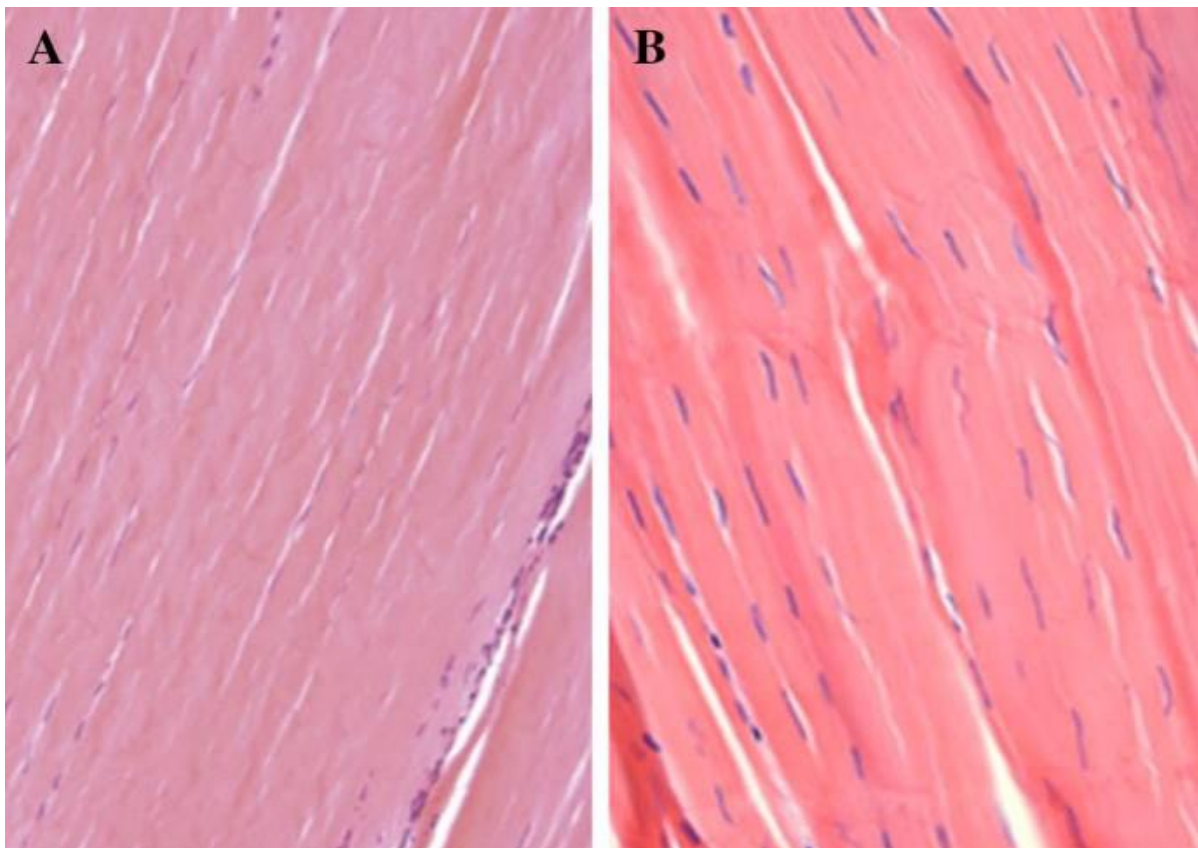Ligament and tendon present excellent mechanical resistance due to their collagen fiber arrangement. During movement, collagen fibers are arranged longitudinally, transversely, and horizontally to provide good buffer capacity. Indeed, tendons and ligaments are made up of collagen fibers, which are ultrastructurally composed of collagen fibrils [19].

Tendons and ligaments are viscoelastic tissues that possess unique mechanical properties. Tendon fibers can withstand high tensile forces when muscles contract during joint motion. Nevertheless, they are sufficiently flexible to angulate around bone surfaces and to deflect beneath the retinacula to change the final direction of muscle pull. Ligaments are flexible and pliant, allowing natural movement of the bones they attach to, yet strong and inextensible enough to resist applied forces. Under normal and excessive loading, both structures sustain primarily tensile loads. When injury happens, the degree of damage corresponds to the rate of loading as well as the amount of load [34].

The biomechanical characteristics of tendons and ligaments are often evaluated by using mounted specimens such as a bone-ligament-bone specimen. However, recent advances have allowed some instrumentation to be used to measure in situ forces in humans. An example is the use of buckle transducers, instrumentation at insertion sites, magnetic resonance imaging, kinematic linkage measurements, and implantable transducers [41]. The use of other techniques like finite element modeling (FEM), elastographic imaging, and robotic/universal force-moment sensor testing is allowing us to gain an insight into the mechanics of tissues [42].

By analyzing the structural and mechanical properties of tendons and ligaments using the above techniques, load-elongation curves and stress-strain diagrams can be obtained.

3.4 Load-elongation curve

After loading a tendon or ligament to failure, the corresponding load-elongation curve provides information about its tensile capacity. As shown in figure (3.7 A), the slope of an elongation curve represents the stiffness of a structure (N/mm). It indicates how much load and or elongation the structure can handle before it fails. The ultimate load (N) is the maximum load placed on the structure before it fails. The ultimate elongation (mm) is the highest elongation of the complex at failure. Last but not least, the energy absorbed at failure (N/mm) represents the maximum amount of energy the complex can absorb [41]. Load-elongation curves have several regions that identify it, figure (3.7 A). In the load-elongation curve, the first region is called the "toe". This elongation is believed to be caused by a change in the wavy pattern or crimp figure (3.3) of relaxed collagen fibers. It is in this region that the tissue stretches easily, the collagen fibers lose their wavy appearance, and sliding occurs between the fibrils and fascicles as loading progresses [43]. Figure (3.8) shows the appearance of relaxed and loaded collagen fibers under an electron microscope.

In response to loading, the tissue stiffness increases and the tissue elongation changes. This region is called the elastic or linear region of the curve. It appears as a sudden increase in the slope of the curve following the toe region. When fiber bundles are pushed beyond the linear region, they fail unexpectedly. A curve can end abruptly or go downward due to irreversible changes (failure) [43]. A complete failure occurs rapidly when the specimen reaches its ultimate tensile strength, and the tendon or ligament's load-supporting ability is significantly reduced. During the elongation process, the tissue is stretched until it ruptures, and the resulting force (P) is plotted. The load value is designated as P_{lin} when the curve levels off toward the elongation axis. Yield points are reached at this value. Until the linear region ends, the area under the curve represents the energy uptake to P_{lin}.
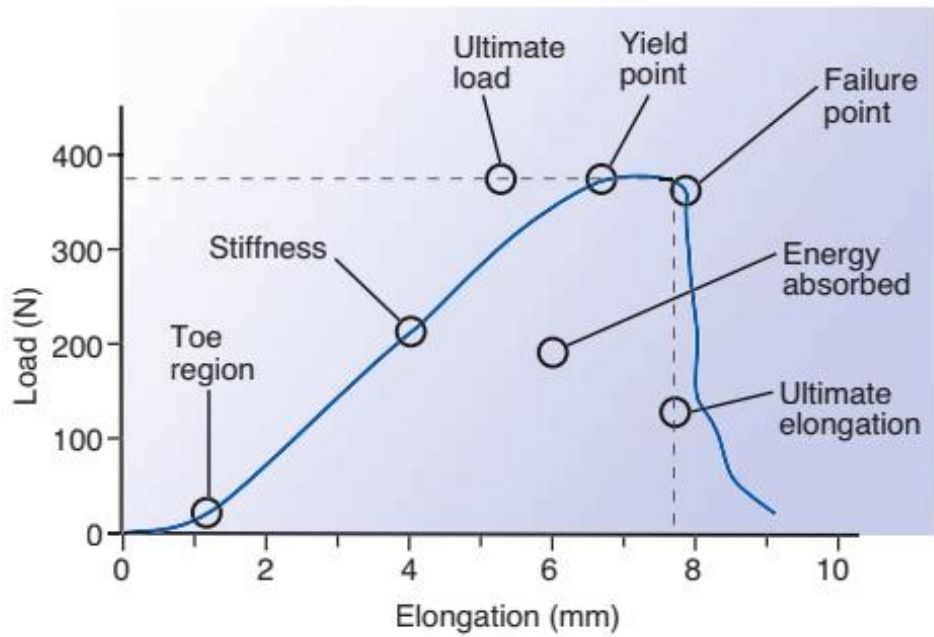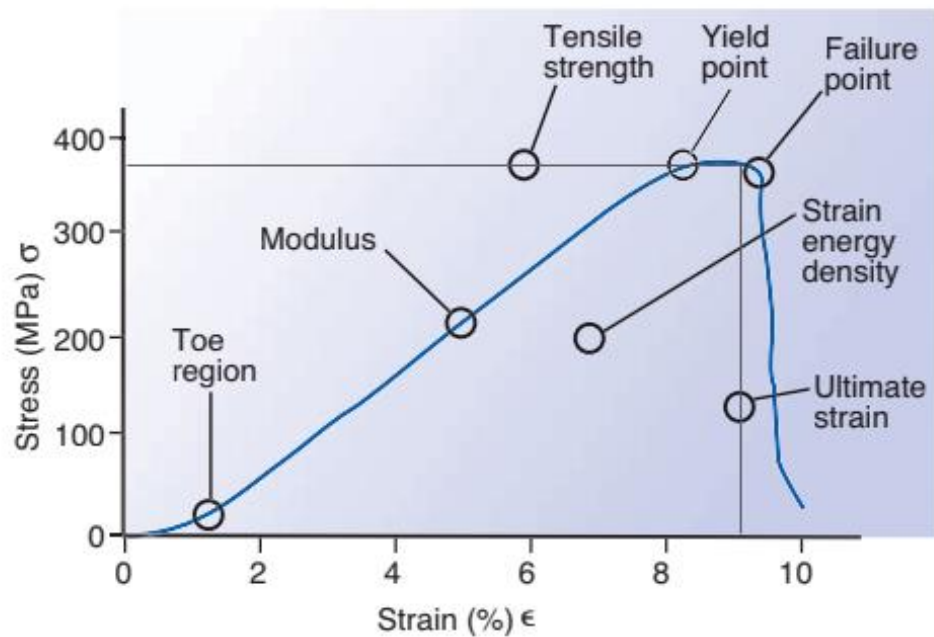
Figure 3. 7: (A) Load-elongation curve of a tendon-ligament structure after loading to failure. The X-axis is the elongation the structure suffers as a result of loading, measured in mm. The Y-axis is the tensile load applied to the tissue measured in newtons (N), (B) A stress-strain curve of a tendon/ligament structure under tensile loading. The X-axis is the percentage of deformation (elongation) expressed as strain (ε) and the Y-axis is the stress or load per unit of area (MPa) expressed as stress (σ), which refers to the tensile strength of the tissue A modulus of elasticity (N/mm^2 or MPa) is obtained from the linear slope of the stress-strain curve between two limits of strain (deformation) [34].

3.5 Stress-strain curves

Figure (3.7 B) shows stress-strain curves generated for tendon and ligament specimens subjected to tensile deformation. A stress-strain diagram depicts elongation as strain (ε), which is the deformation of the tissue calculated as a percentage of its original length. A stress (σ) is defined as the force per unit area (in this case, the total tensile load per unit of the cross-sectional area of the tendon or ligament). The paragraph describes the need to measure the cross-sectional area of a ligament for stress calculations. Laser micrometry is a reliable method for obtaining accurate measurements without distorting the soft tissue's cross-section. The technique involves rotating the specimen 180^0 while recording its profile widths using its shadow, and then digitally reconstructing the cross-sectional shape and area. According to figure (3.7 B), the linear slope between two limits of strain (deformation) is used to determine a modulus (N/mm^2 or MPa) from stress-strain curves. In this curve, the ultimate strain (in percentage) represents the strain at failure, the tensile strength (N/mm^2) represents the maximum stress achieved, and the strain energy density (MPa) represents the area under the stress-strain curve. This modulus of elasticity for tendons and ligaments has been determined in several investigations [44, 45], and it represents a linear and proportional relationship between load and deformation or stress and strain:

$$E = \frac{\sigma}{\varepsilon} \qquad (1)$$

where E = modulus of elasticity, σ = stress, and ε = strain.

Figure 3.9 depicts an example of ACL's biomechanical properties [20]. The stress-strain relationship of ACL obtained under tensile loading shows a three-phase graph consisting of (a) the toe region, (b) the linear region, and (c) the yield region. The crimp pattern in the collagen fibrils straightens out at low stresses, identifying the toe region [46]. Resistance force gradually rises in the linear region with elastic deformation. The yield region marks the beginning of permanent deformation [47]. Due to the breakage

of collagen fibrils, stress decreases at this point, eventually resulting in ligament rupture.

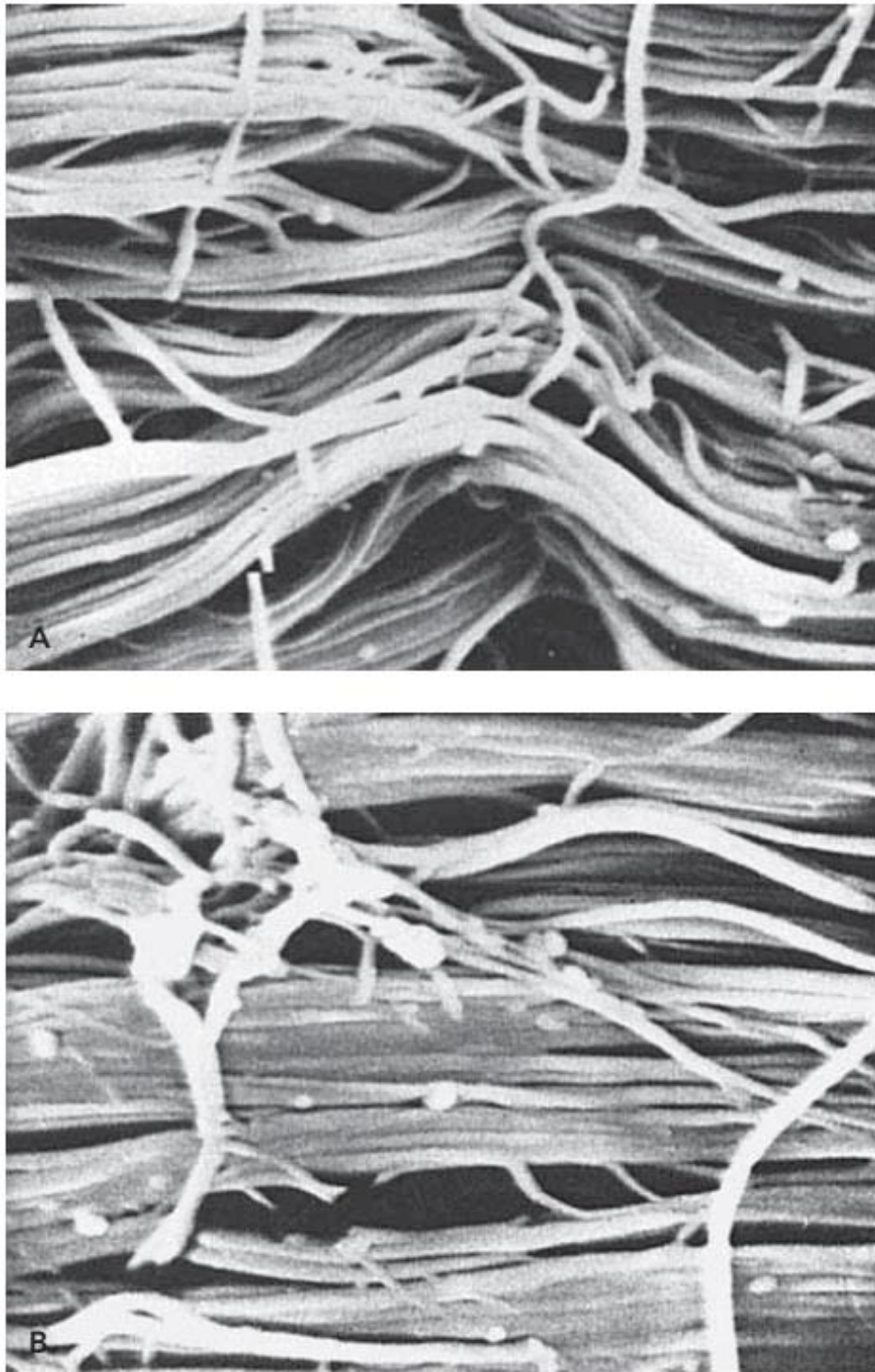Figure 3. 8: Scanning electron micrographs of unloaded (relaxed) and loaded collagen fibers of human knee ligaments (×10,000). A. The unloaded collagen fibers have a wavy configuration. B. The collagen fibers have straightened out under load [34].
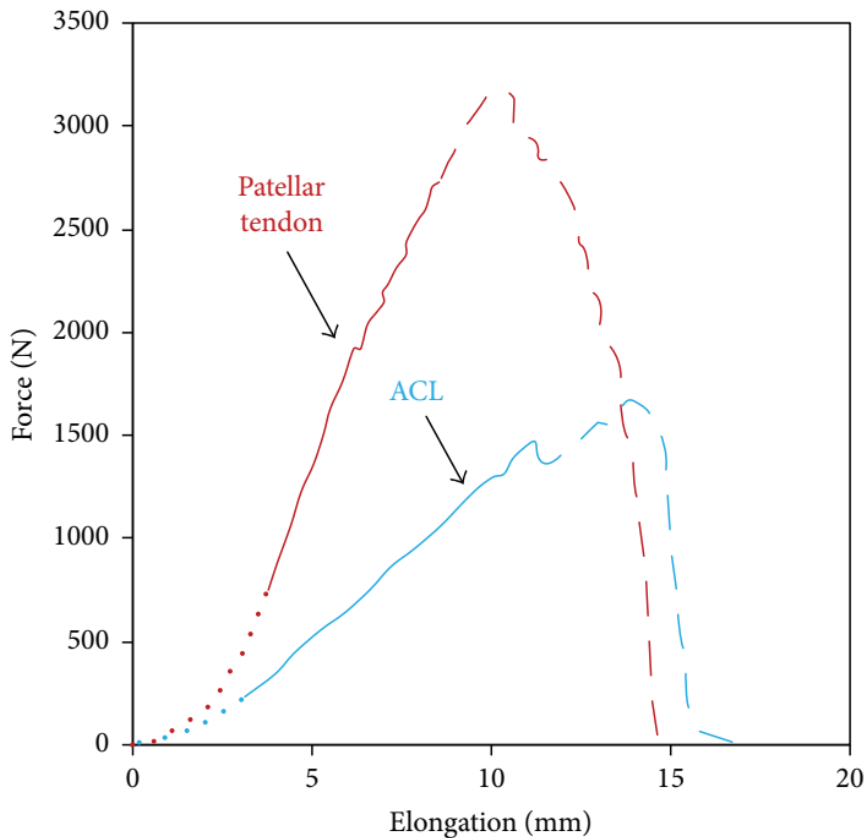
Figure 3. 9: Tensile strength of ACL and the patellar tendon [20]. The dotted lines represent the toe region, continuous lines represent the linear region, and dashed/broken lines represent the yield region.

3.6 Ligament failure and tendon injury mechanisms

Ligaments and tendons have similar injury mechanisms. They can be divided into two main groups or a combination of both: high levels of stress or load (such as when sudden external force is applied), high levels of strain (such as those resulting from overuse or repetitive microtrauma that exceeds the reparative process), or high levels of stress and strain (such as in contact-collision sports).

When a ligament *in vivo* is subjected to loading that exceeds the physiological range (injuries caused by high levels of stress), either microfailure occurs even before the yield point (P_{lin}) is reached (i.e., partial rupture of a ligament) or the ligament will undergo gross failure (complete rupture) if the P_{lin} is exceeded. The joint will simultaneously begin to displace abnormally and show signs of instability when this happens. It is also possible for this displacement to damage surrounding structures, such as the joint capsule, the adjacent ligaments, as well as the blood vessels that supply

them. Noyes et al. [48], explained the progressive failure of the ACL and displacement of the tibiofemoral joint by applying a clinical test, known as the anterior drawer test, to a cadaver knee until the ACL failed, Figure (3.10). The ligament elongated beyond its elastic region after the joint displaced several millimeters at maximum load. Despite its continuity, the ligament had suffered extensive macrofailure and microfailure as well as extensive elongation, resulting in structural and mechanical damage.
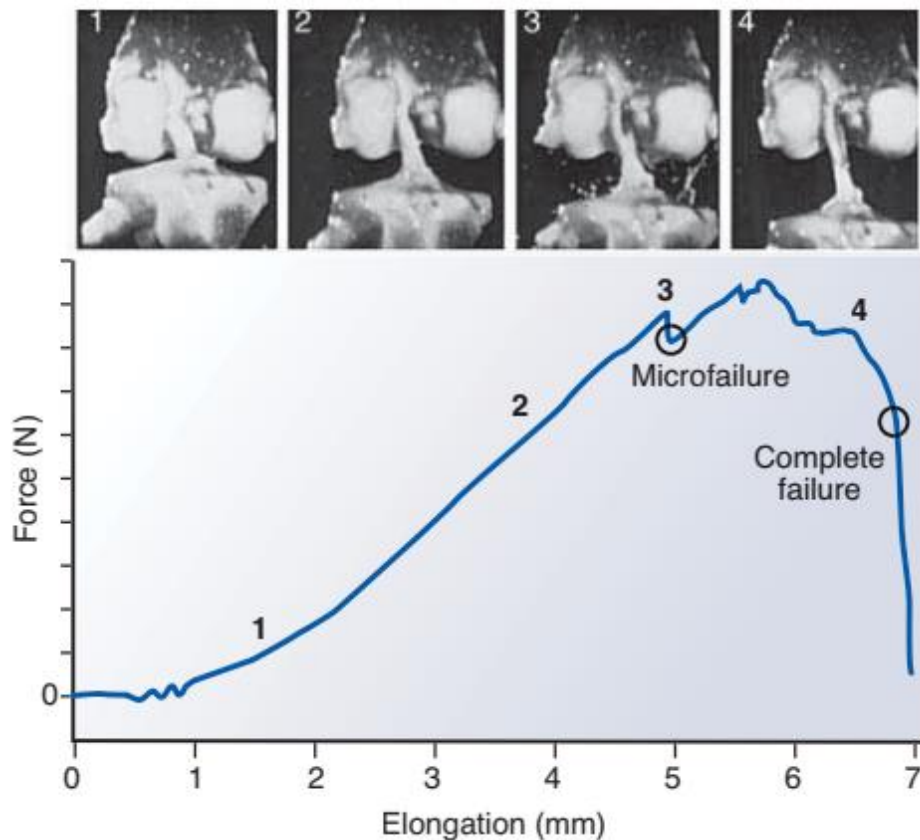
Figure 3. 10: Progressive failure of the anterior cruciate ligament from a cadaver knee tested in tension to failure at a physiologic strain rate [34].

Correlation of the results of this test *in vitro* with clinical findings sheds light on the microevents that occur in the ACL during everyday activities and during injuries of various degrees of severity. The experimental study of cadaver knees is depicted in Figure (3.11) corresponds to four load-displacement regions, representing (1) the load placed on the ACL during clinical tests of knee joint stability, (2) the load placed on this ligament during physiologic activity, (3) the force applied to the ligament and (4)

resulting permanent deformation from microfailure to complete rupture, Figure (3.11) [34].
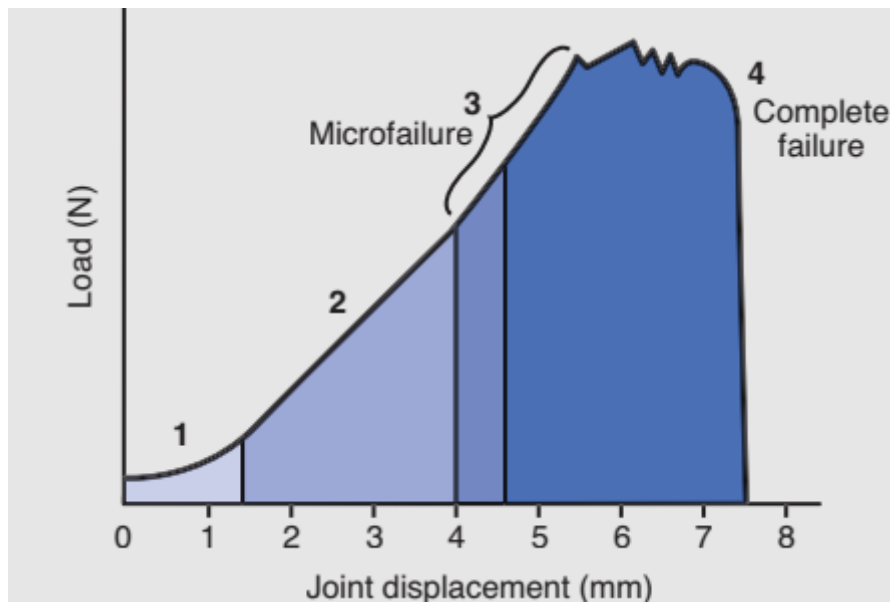
Figure 3. 11: This is a representation of a load (Y axis)- elongation (X axis) curve of a progressive failure of an ACL of the knee. Zone 1 represents the TOE region. Zones 2 and 3 represent the elastic and plastic regions, respectively. The microfailure starts as permanent deformation that begins in the plastic region. As the load/deformation continues, a complete failure is reached. The injury region represents microfailure and complete failure within the ligament [34].

4 MATERIALS AND METHODS

In this section, we introduce the proposed approach that was designed to enhance and support the analysis of tendon or ligament microstructures by exploiting microCT. Before explaining the proposed solution in detail, it is useful to provide more information about the background of the concepts that are applied in this study.

4.1 Background

4.1.1 Image normalization

Image normalization is a process that is used to change the range and distribution of pixel intensity values in an image for better perception and analysis [49]. The purpose of normalization is to enhance the image contrast. The percentile was used due to its capability to determine the input range based on the real intensities of the input image. For instance, if percentiles of 1 and 99 are used, the top and bottom 1% of pixel values will be clipped to 0.0 or 1.0. Consequently, intensity contrast will be normalized effectively. The cropped grayscale image can be normalized by dividing the observed intensity using percentile of the half of maximum intensity:

$$I = \frac{I}{prctile(I(I > 0.5 \times \max(I)), 90)} \qquad (1)$$

where the predefine MATLAB function prctile and max were used to calculate the percentile and the maximum intensity of the input image (I).

4.1.2 3D Hessian-based multiscale filtering

Tendon or ligament fascicles are irregular in shape and differ in diameter, ranging from 150 to 500 μm and settled along the longitudinal axis [26,50]. Hence, the enhancement or detection of fascicle microstructures in microCT scans is based on differential geometry and scale-space paradigm. The second order gradient with a Gaussian kernel (G) at multiple scales (σ) produces a response of local intensities [51]. This demonstrates the contrast between the regions inside and outside the scale range in the

direction of the derivative [52]. In other words by combining Gaussian convolution with the second derivative, the filter response is tuned to the specific width of fascicle.

Let $f(X)$ represents the intensity of a N-dimensional image at coordinate $X = [x_1, x_2, \dots, x_N]^T$. The Hessian of $f(x)$ at x and scale σ is then represented by a $N \times N$ matrix:

$$H_{i,j}(X,\sigma) = \sigma^2 f(X) * \frac{\partial^2}{\partial x_i \partial x_j} G(x,\sigma) \quad for \ i,j = 1,2,\dots N \tag{2}$$

$$G(X,\sigma) = \frac{1}{\left(\sqrt{2\pi\sigma^2}\right)^N} \exp\left(\frac{-X^T X}{2\sigma^2}\right) \tag{3}$$

Where $G(X,\sigma)$ is a N-dimensional Gaussian and $*$ denotes convolution.

Along the orientation of the fascicles, the image intensity remains constant. Blurring the image with Gaussian kernal along the tubular structure's orientation will not have any effect.

The Hessian matrix $H(f)$ of a 3D image $f(x_1, x_2, x_3)$ is given by:

$$H(f) = \begin{bmatrix} \frac{\partial^2 f}{\partial^2 x_1} & \frac{\partial^2 f}{\partial x_1 \partial x_2} & \frac{\partial^2 f}{\partial x_1 \partial x_3} \\ \frac{\partial^2 f}{\partial x_2 \partial x_1} & \frac{\partial^2 f}{\partial^2 x_2} & \frac{\partial^2 f}{\partial x_2 \partial x_3} \\ \frac{\partial^2 f}{\partial x_3 \partial x_1} & \frac{\partial^2 f}{\partial x_3 \partial x_2} & \frac{\partial^2 f}{\partial^2 x_3} \end{bmatrix} \tag{4}$$

Once the Hessian matrix is calculated, the Eigenvalue analysis is performed on the Hessian matrix.

Eigenvalues of the $H(f)$ are: $\lambda_1, \lambda_2, \lambda_3$; and λ_1 give the maximum second derivative value. Corresponding eigenvectors: e_1, e_2, e_3. For the fascicles e_1 represents the orientation along which the second derivative is maximum. Consequently, λ_1 represents the parallel curvature while λ_2 and λ_3 represent the orthogonal curvatures figure (4.1) [53,54].

Since the intensity of the image remains constant along the fascicle/fiber's orientation, $|\lambda_1|$ should be very close to zero.

$$|\lambda_1| \approx 0 .$$

It follows that at the center of the fascicle/fiber, the two eigenvalues should be approximately equal, and their absolute value should be much greater than zero.
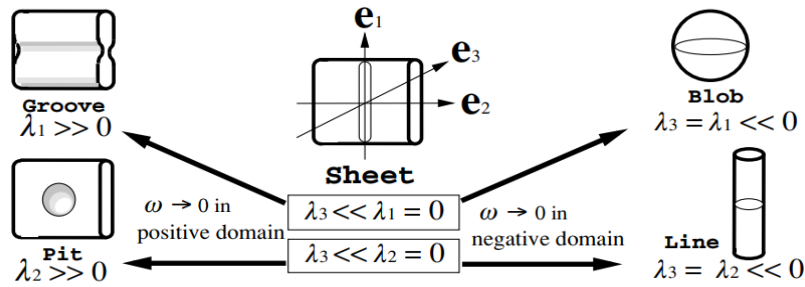
$$|\lambda_2| \approx |\lambda_3| \gg 0$$

Figure 4. 1: Schematic diagrams of measures of similarity to local structures. The roles of weight functions in representing the basic conditions of a local structure are shown. Sheet measure. The structure becomes blob-like, groove-like, line-like, or pit-like with transition from $\lambda3 \ll \lambda1 \simeq 0$ to $\lambda3 \simeq \lambda1 \ll 0$, $\lambda3 \ll \lambda1 \simeq 0 \, to \, \lambda1 \gg 0$, $\lambda3 \ll \lambda2 \simeq 0 \, to \, \lambda3 \simeq \lambda2 \ll 0$ or $\lambda3 \ll \lambda2 \simeq 0 \, to \, \lambda2 \gg 0$, respectively [55].

Then, the Frangi filter for the 3D images [51], is computed as follows:

$$S = \sqrt{\lambda_1^2 + \lambda_2^2 + \lambda_3^2} \quad , R_\beta = \frac{\lambda_1}{\sqrt{\lambda_2 \lambda_3}}, R_\alpha = \frac{\lambda_2}{\lambda_3}$$

A smaller value of S implies that the voxel belongs to background and a larger value of S implies that the voxel is close to the centerline of the fascicles. R_β discriminates the blob while R_α distinguishes tubular structures (i.e., fascicles). These quantities are involved in the following function:

$$V_\sigma = \begin{cases} 0, & \lambda_1, \lambda_2 > 0 \\ \exp\left(\frac{R_\beta^2}{2\beta^2}\right)\left(1 - \exp\left(\frac{R_\alpha^2}{2\alpha^2}\right)\right)\left(1 - \exp\left(\frac{S^2}{2C^2}\right)\right), & otherwise \end{cases} \qquad (5)$$

Where β, α and c are positive real user-defined parameters. If the magnitude of both eigenvalues is small, i.e., the local image structure is likely to be part of the background, then the vesselness (V_σ) measure will be small. If one eigenvalue is small

and the other is large, then the local structure is likely to be curvilinear and the (V_σ) measure is large. Then, the maximum V response is:

$$V = \max_{\sigma min \leq \sigma \leq \sigma max} V(\sigma)$$

The values of σmin and σmax are selected according to the corresponding lowest and highest expected size of the fascicles. Jerman, Tim, et al. [56] improved the filter response function in equation (6) by robust to low magnitudes of λ_2 and λ_3, the value of λ_3 at every scale (σ) was regulated as:

$$\lambda_\rho(\sigma) = \begin{cases} \lambda_3 & if\ \lambda_3 > \tau\ max_x\lambda_3(x,\sigma), \\ \tau\ max_x\lambda_3(x,\sigma) & if\ 0\ < \lambda_3\ \leq \tau\ max_x\lambda_3(x,\sigma), \\ 0 & otherwise. \end{cases} \qquad (6)$$

Where τ is a cutoff threshold between 0 and 1.

To normalize the response of proposed enhancement, function through the scales λ_ρ is calculated for each scale σ individually. For structures of very low contrast, which otherwise have low magnitude of λ_2 and λ_3 , a high value of results in a high difference between the magnitudes of λ_3 and λ_ρ is selected and thus controls the response. Therefore, the Jerman enhancement function is calculated as:

$$V_p = \begin{cases} 0 & if\ \lambda_2 \leq 0\ \vee \lambda_\rho \leq 0, \\ 1 & if\ \lambda_2 \geq \dfrac{\lambda_\rho}{2} > 0, \\ \lambda_2^2\ (\lambda_\rho - \lambda_2)\ \left[\dfrac{3}{\lambda_\rho + \lambda_2}\right]^3 & otherwise. \end{cases} \qquad (7)$$

Function (7) can be computed for both bright structures on dark background and dark structures on white background.

4.1.3 Morphological operation

Morphological operators are a set of non-linear filters to extract specific morphologies from the image [57]. They can be used in binary or gray scale images. The structuring element (SE) defines the morphological operator locality with specific dimension and

shape, such as line, circle, square, sphere and others. The specific selection of structuring element is key to morphological processing. The basic operators are dilation and erosion. Therefore, by combining these two operators we can further define two commonly used morphological filters.

4.1.4 Dilation and erosion

If $f(\vec{p})$ is a grey-scale or binary image and $B(\vec{p})$ is an arbitrary structuring element where $(\vec{p})$ implies the pixel position $[x, y, z]^T$ in the 3D images. Dilation ($\oplus$) can be described as the maximum of the pixels in a weighted neighborhood selected by the structuring element, and mathematically as follows:

$$(f \oplus B)(\vec{p}) = \sup_{X \in E}[f(X) + B(\vec{p} - X)] \qquad (8)$$

where 'sup' is the supremum and $X \in E$ denotes all points in Euclidean space within the image. Similarly, erosion ($\ominus$) can be defined as the minimum of the points in the neighborhood that match the structuring element:

$$(f \ominus B)(\vec{p}) = \inf_{X \in E}[f(X) + B(\vec{p} - X)] \qquad (9)$$

where 'inf' is the infimum. The effect of dilation is enlarging the boundaries of foreground pixels, while erosion eliminates irrelevant detail [58].

In Matlab, image dilation and erosion can be achieved by using predefined functions named ***imdilate*** and ***imerode***, respectively**.**

4.1.5 Opening and closing

When dilation and erosion are combined, opening and closing are possible. The first is erosion, followed by dilation with the same structuring element, and the second is reversal. As the opening removes small and isolated objects and preserves the background, the closing preserves bright features by removing small holes in the foreground.

Opening: $(f \circ B)(\vec{p}) = ((f \ominus B) \oplus B)(\vec{p})$ \qquad (10)

Closing: $(f \bullet B)(\vec{p}) = ((f \oplus B) \ominus B)(\vec{p})$ (11)

where an opening (∘) tends to break thin linking areas in an object, and a closing (•) tends to join narrow isthmuses between object [58].

In Matlab, image opening and closing can be achieved by using predefined functions ***imopen*** and ***imclose,*** respectively**.**

To sum up, opening is used for smoothening of contour and merging of narrow breaks. It eliminates the thin protrusions of the obtained image. On the other hand, closing is used for reducing internal noise of the obtained image. It eliminates the small holes from the obtained image.

4.1.6 Orientation and diameter estimation

To understand fascicle's structure and function; orientation, and diameter were extracted for each fascicle in the 3D volumetric binary image. Figures 4.2 and 4.3 illustrates the schematic diagram of the fibers organization in 3D plane. The predefined function ***regionprops3*** in Matlab was used to measure these features.

Orientation was estimated based on Euler angle and calculated with respect to z axis which represents the longitudinal plane Figure (4.4A); our orientation is represented by an angle θ between $0\,^o$ and $90\,^o$. For instance, we considered the fascicle more aligned if the theta equals or is close to 0 and inversely if it is away from zero. The organization of the fascicles is considered well alignment with the z axis if the orientation closes to zero.

Evaluation of the fiber diameter was done in3D, we used the ***"PrincipalAxisLength"*** value passing to ***regionprops3*** function. The lengths (in voxels) of the major axes of the ellipsoid that have the same normalized second central moments as the region, returned as 1-by-3 vector represent the three axis lengths ordered ascendingly.

Calculation of the diameter profile of an ellipsoid model: the smallest axes in (x,y) were extracted from the 3D image, and the diameter is estimated to be their average, Figure (4.4B).
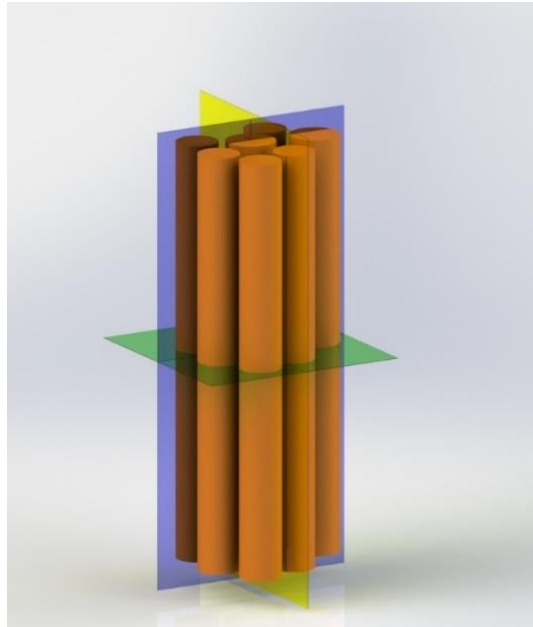

Figure 4. 2: Schematic diagram to illustrate the 3 planes among the fibers microstructures modeled as tube.
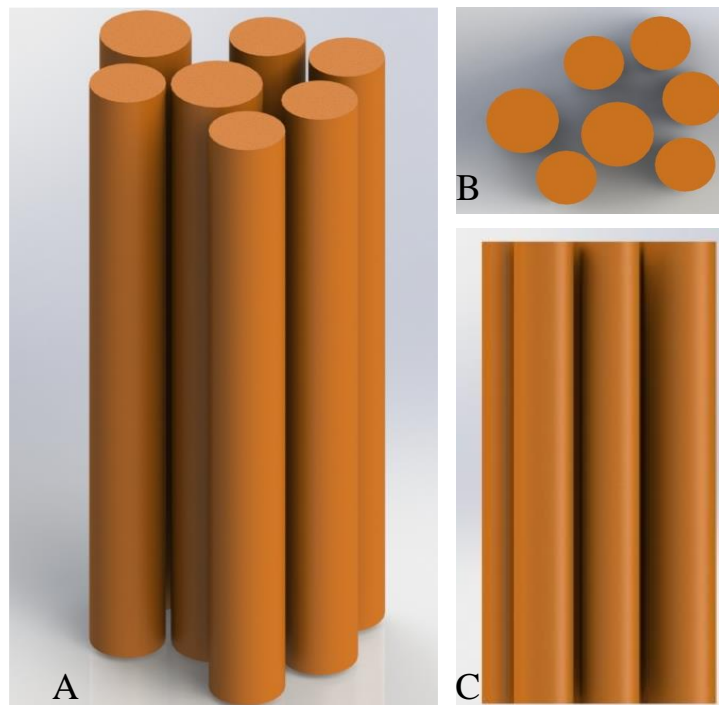

Figure 4. 3: Fibers model (A) 3D view (B) transversal view and (C) longitudinal view.
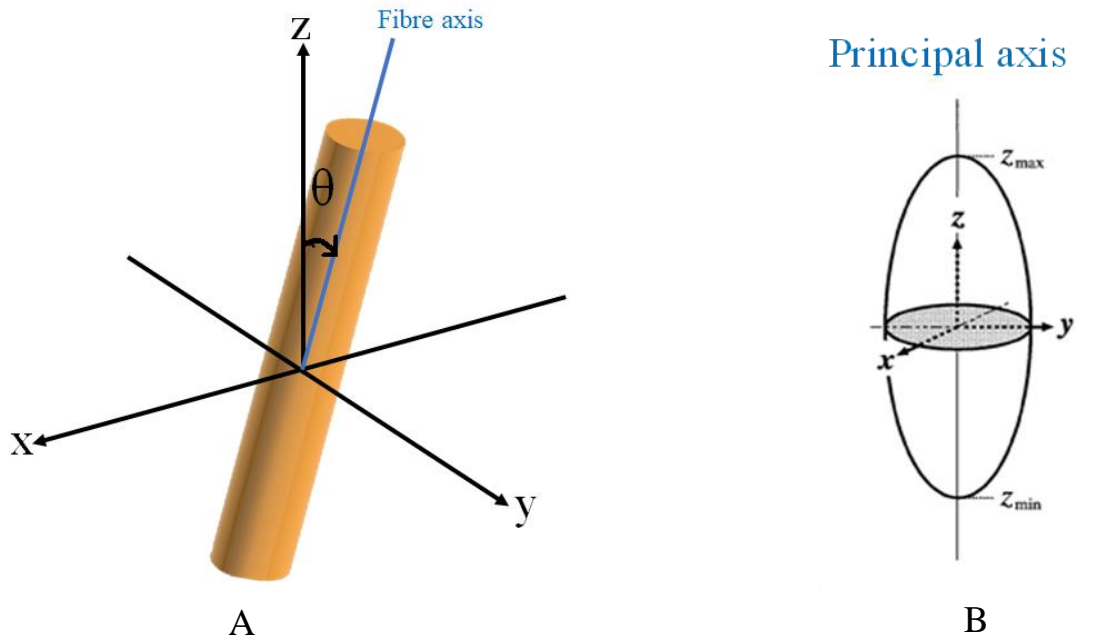
Figure 4. 4: A schematic of quantifying fiber/fascicle (A) orientation in 3D. The tube represents fiber. The angle θ is the angle of fiber with respect to z axis, (B) diameter.

4.2 Case study 1: Tendon and ligament

This case study has been partially reported in the Journal of Mechanics in Biology and Medicine, as "Contrast-Enhanced Microtomography for Volumetric Analysis of Microstructure in Ligaments And Tendons" By Bushara F., Maglio M., Marchiori G., Giavaresi G., Signoroni A., Guerrini F., Lopomo N.F. (ahead of print).

Highlighting the microstructure components of ligaments and tendons in 3D images is a crucial step for extracting meaningful information in several applications. In this study, microCT images were used for data acquisition after performing X-ray contrast enhancement on these soft tissues. Hence, two kinds of samples were used, human hamstring tendon and bovine ligament. To characterize these microstructures and their organization, important parameters including diameter and orientation were required. Therefore, a digital image processing algorithm was applied and implemented by dedicated routines (Matlab 2022b, The Mathworks, USA).

The proposed algorithm consists of three main stages: contrast enhancement, fascicles and fibers detection based on a multi-scale Hessian filter, and fibers orientation and diameter measurements. All the images in this study were acquired at the Laboratory

of Surgical Science and Technologies of the IRCCS Istituto Ortopedico Rizzoli, Bologna, Italy. First, all the specimens were specifically prepared for CE-microCT imaging approach; then image acquisition via microCT and image reconstruction were performed. A dedicated image processing and analysis procedure was designed and implemented for revealing tissue microstructures.

Figure (4.5) illustrates the block diagram of the proposed method to study the tendon and ligament microstructures based on microCT images.
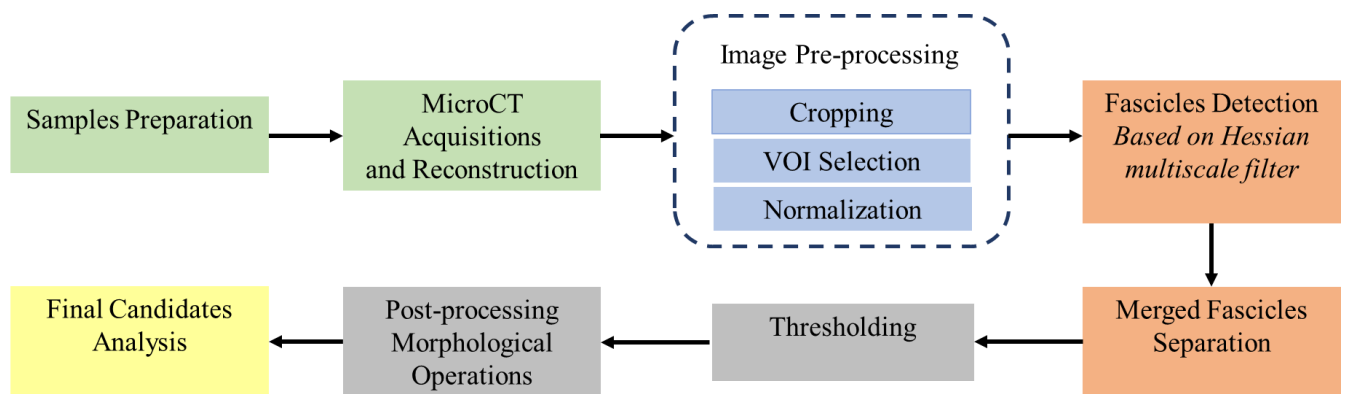

Figure 4. 5: Flowchart of the developed CE-microCt protocol. First, the sample preparation and *m*icroCt image acquisition and reconstruction. The second step, i.e., image preprocessing, is the major novelty of this work. Second: Hessian matrix of the processed images was computed Given the obtained eigenvalues, and Frangi's filter detected the fascicles. Next, the detected fascicle obtained using the frangi filter was enhanced with morphological filters. Third, thresholding was applied. Fourth: post-processing was required to obtain the well-defined fascicle on segmented structures, and finally: the fascicle features were calculated in 3D.

4.2.1 Tendon and ligament samples

Two kinds of samples were used in this study, human hamstring (HH) tendon and collateral bovine (CB) ligament (fresh and dried). A human hamstring tendon was collected from the International Bank of Musculoskeletal Tissues (Science Care, USA), in the context of a clinical study approved by the local Ethics Committee (IRCCS Istituto Ortopedico Rizzoli, Protocol "TISS-KNEE" 8425), while the bovine ligament came from a local abbatoir; they were stocked by fresh freezing at -20°C before testing. The samples were then thawed and measured by a caliper (specimen diameter of about 6 mm) for gross evaluations to point out any possible tissue alterations, e.g., shrinking or swelling figure (4.6).

Then, each sample was divided into two portions:

The first one was included in the PTA contrast group, cut in five sub-portions to obtain:

1. one segment for contrast with 2 % PTA in water solution (PTA in H_2O).

2. one segment for contrast with 2 % PTA in alcoholic solution (PTA in EtOH).

3. one segment not contrasted for histological transversal cut, adjacent to PTA in H_2O.

4. one segment not contrasted for histological transversal cut, adjacent to PTA in EtOH.

5. one segment not contrasted taken from the central portion for histological longitudinal cut.

The second one was entirely used for chemical drying with HMDS, then cut into two sub-portions and rehydrated to obtain:

1. one segment for histological transversal cut.

2. one segment for histological longitudinal cut.

Differently from chemical drying performed via HMDS [27], the reliability of histological processing of segments already contrasted with PTA is still not fully validated; for this reason, dedicated segments were employed for PTA group.
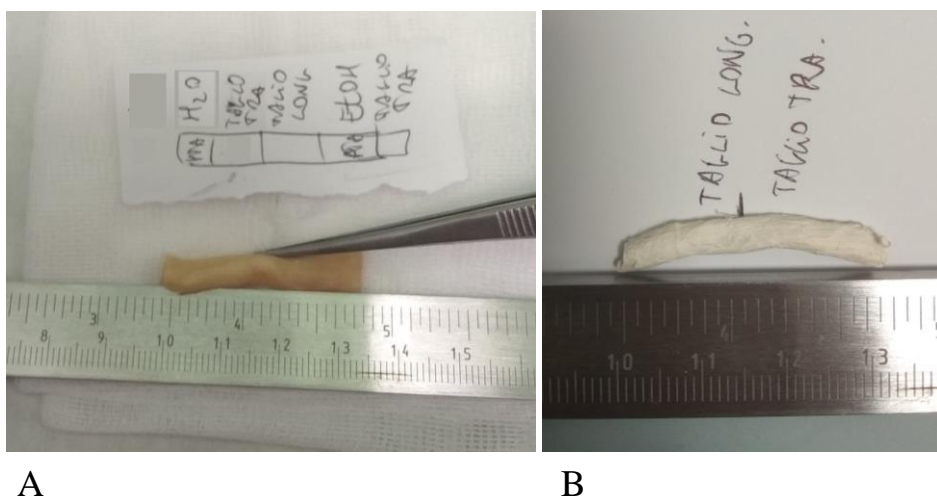

A   B

Figure 4. 6: Human Hamstring tendon sample: (A) The fresh sample, and (B) the HMDS dried sample. Reported units are in cm/mm.
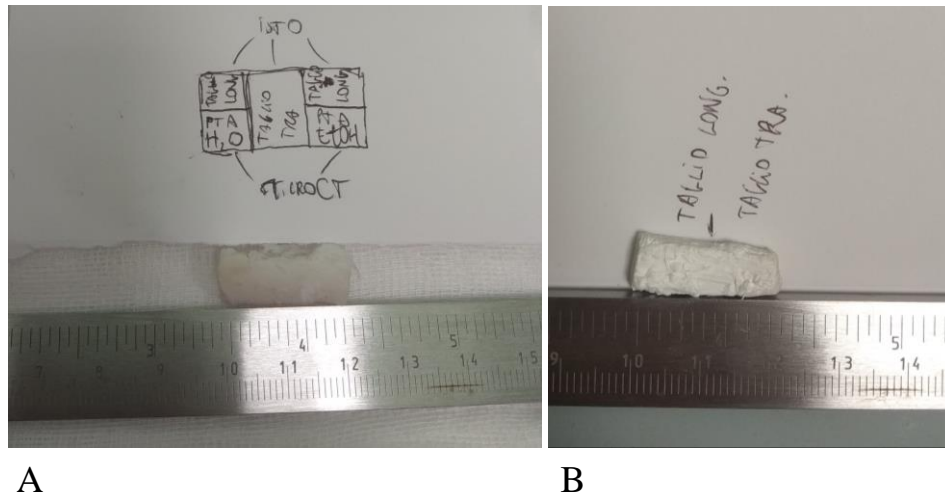
| A | B |

Figure 4. 7: Bovine Collateral ligament sample: (A) The fresh sample, and (B) the HMDS dried sample. Reported units are in mm/cm.

4.2.2 Sample Preparation

All the obtained tissue segments were fixed in 10% formalin (Sigma-Aldrich, US) for 48 hours at room temperature and rinsed in distilled water. Two different PTA contrast solutions were prepared dissolving the PTA in powder (Sigma-Aldrich, Saint Louis, Missouri, US) respectively in distilled water or 70% alcohol, up to a concentration of 2% PTA for each solution. The specimens were treated as follows:

1. for PTA contrasted group, segments were submerged in PTA in H_2O or PTA in EtOH solutions according to the defined scheme up to 5 days at room temperature.

2. for HMDS chemical dried group, segments were dehydrated in an increasing series of alcoholic solutions up to 100%, with step of 12 hours each, and finally exposed to HMDS (Sigma-Aldrich, US) for 4 hours and then left to dry under chemical hood for 48 hours [59].

4.2.3 MicroCT Acquisitions

After contrasting/drying, the samples were mounted within Eppendorf plastic tubes, filled by the specific PTA solution in the case of contrasted samples; to prevent movement during scanning. The samples were scanned in the (Skyscan 1172*Bruker*, Belgium) at a nominal resolution (pixel size) of 5 μm. In the case of PTA contrasted

samples, an aluminum filter 0.5 mm thick and an x-ray tube voltage of 70 kV were applied [60]. In the case of dried sample, no filter was used, and an x-ray tube voltage of 40 kV was applied [59].

Reconstruction was carried out with a modified Feldkampii algorithm using the SkyScanTM NRecon software (version 1.7.4.6, *Bruker*) accelerated by GPU. Ring artefact reduction (5 for PTA contrasted samples, 10 for dried sample) and beam hardening correction (30%) were applied. To optimize the tissue contrast in the reconstructed images, the contrast limits in the histogram of attenuation coefficient tuned. The lower contrast limit attenuation value was set to 0.02 to remove out-of-tissue signal in the case of the dried sample; it was set to 0.045 or 0.06 to remove out-of-tissue signal and EtOH or water absorption, respectively for sample in EtOH or in H_2O solution. The upper contrast limit was set to 0.09 (dried), 0.18 (EtOH) or 0.25 (H_2O), a value 10-20% higher than the maximum attenuation of the specific material of interest [61]. Reconstructed images were saved in 16-bit TIFF format.

In the case of PTA contrasted samples, for evaluating the progression of the contrast agent through the tissue, three scans after three different exposition periods were performed on the same sample, i.e., overnight, 3 days and 5 days.

4.2.4 Image preprocessing

Image preprocessing is an essential step before applying a 3D Hessian-based multi-scale filter. This step consists of image cropping followed by normalization.

- ▪ **Image Cropping**

This step reduced computational resources by selecting the most relevant regions of an image and excluding the unnecessary ones, such as non-informative noises. Therefore, cropping was accomplished by defining subjectively the best proposal window that includes the VOI. The cropping process involved a subjective determination of the optimal proposal window encompassing the VOI, accomplished using the Matlab predefined function ***imcrop3***. As an example, the original size of the human hamstring

HMDS dried image was (2460×2460×6721), and it was cropped to (1100×1100×6721), as illustrated in Figure (4.8).

- **Normalization**

The cropped image was normalized to enhance the contrast intensity. We follow the same technique described in section 4.1.1.
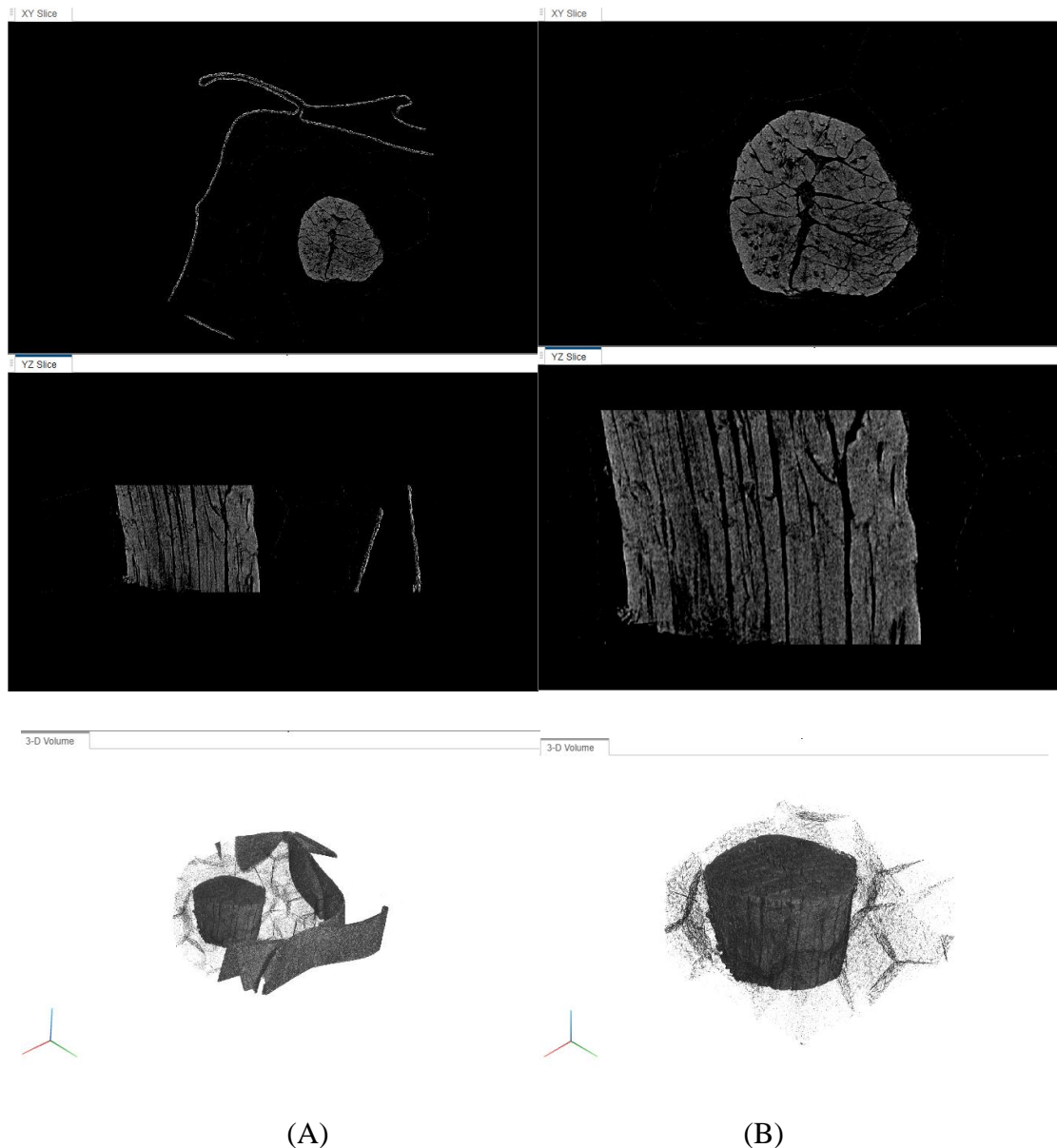

(A)   (B)

Figure 4. 8: MicroCT for Human Hamstring HMDS dried sample (A) original image XY plane size (2460×2460), and (B) cropped image in XY plane to size (1100×1100), from up to down show the transverse slice, longitudinal slice, and 3D volume rendering.

4.2.5 Microstructures enhancement and detection

Enhancement filtering was specifically designed for the detection of microstructures in tendons and ligaments. In particular, fascicle enhancement filters serve a dual purpose of reducing image noise and artifacts while detecting the fibers that make up the fascicles. To achieve this, a multi-scale tubular filtering approach based on the Hessian matrix is applied to the processed volume of interest (VOI). This provides both structural and directional information about the fascicles, enabling the detection of tubular objects at multiple scales. An improved filter by Jerman et al. [56] was used to detect tubular objects in the background while preserving microstructure details. Filter scales are experimentally determined for each specimen to optimize the detection process. With these methods, it is possible to detect fascicles and their principal directions accurately and efficiently, which is essential for understanding the biomechanics of tendons and ligaments.

4.2.6 Merged fascicles separation

The purpose of this step is to split the merged fibers and compensate for the discontinuity. Therefore, morphological opening was used to improve the VOI obtained from the previous step. The opening transformation is a morphological filter that exploits the structuring element to compute the morphological opening of the image. The opening used a flat structure element scanned over the VOI and every point in the center of the structure element is substituted with one of the pixel values (the lowest or highest pixel value) under the structure element depending on the operation (erosion or dilation).

The structure element was created in 3D using Matlab exchange files. For the opening line structuring element in 3D was used. The resulting image from the opening process dilated with sphere structure element in 3D with size of 10 voxel. In Matlab the structural element was created using the function *strel3d* [61].

4.2.7 Thresholding

A threshold was applied to distinguish the fascicles and the non-fascicles signals. Therefore, micro-CT images were binarized based on adaptive threshold of the processed images. Binary segmentation labels the image into two subsets corresponding to their intensity: foreground or background. It segments an image intensity as follows: if the intensity of a point is greater than the threshold, it is allocated to one label; otherwise it is assigned to the other label. The thresholding can eliminate fibers which were split mistakenly or microstructures that were erroneously labeled as fibers.

4.2.8 Morphological process

Due to the grouped nature of the microstructures of interest, detecting individual fascicles in the image was a challenge. Therefore, morphological filters were applied to separate touching fascicles to estimate the size and orientation of individual fascicles.

Morphological filters were used to track and connect fascicles. First: opening operation was applied to clean the data for the next step. Second: erosion was applied for the resulted image from the opening step to split merged fascicles followed by dilation to fill the hole and compensate the damaged fascicles. Finally, opening was applied again to emphasize the separation process of the fascicles.

4.2.9 Individual fascicle measurements

After the image thresholding process and 3D visualization of tendon and ligament fibers was completed, the resulting data were used to acquire the geometric attributes of the fibers in 2D such as diameter or in 3D such as orientation and volume. These measurements were displayed using histogram distribution. Measurements of segmented fascicles were calculated using the predefined function *regionprops3* in Matlab. The size of each fascicle was then measured in voxel size in 3D and converted to metric units for further analysis.

4.3 Case study 2: Anterior cruciate ligament (ACL)

Tendons and ligaments have adjustment capability to the changes in their mechanical behaviors related to loading, injury, or disease. This section describes the analysis of the variations in ACL fibrous microstructure among different levels of strain from 3D microCT images. The microstructures of the ACL are principally responsible for their mechanical properties. In particular, the directional distribution of the fiber system influences their tensile strength. In order to study the fascicles orientation at different given stretch levels on microCT images, highlighting fascicles structures was indispensable. Therefore, several quantities characterizing fascicles as well as a wide range of image analysis algorithms for computing these quantities from 3D data obtained by microCT have been proposed.

A brief description of the steps performed to enhance the grayscale contrast between the fascicles and non-fascicles parts of the ACL is shown in figure 4.9. We follow the same steps for the image processing and analysis of the case study 1 which are described in section 4.2 except to the preprocessing step due to difference in image acquisition. Then, the detected microstructures were analyzed to get the volume, diameter, and orientation respect to main axes of each fascicle. Furthermore, statistical analysis for the diameter like (variance) and for the orientation such as the (entropy and the energy) were computed. Finally, we built a mechanical model of ACL behavior during different tension levels for both healthy and pathological samples.
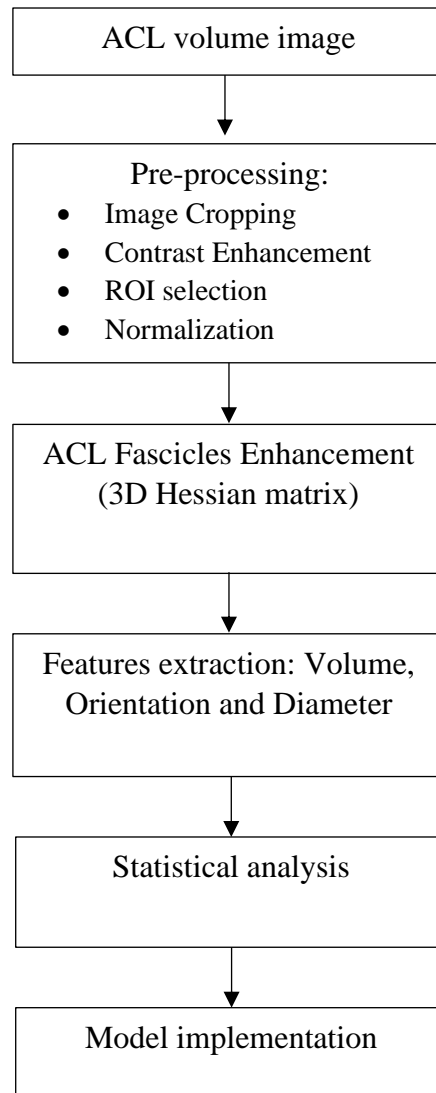
```
┌─────────────────────────────────┐
│         ACL volume image        │
└─────────────────────────────────┘
                 │
                 ▼
┌─────────────────────────────────┐
│  Pre-processing:                │
│   • Image Cropping              │
│   • Contrast Enhancement        │
│   • ROI selection               │
│   • Normalization               │
└─────────────────────────────────┘
                 │
                 ▼
┌─────────────────────────────────┐
│  ACL Fascicles Enhancement      │
│  (3D Hessian matrix)            │
└─────────────────────────────────┘
                 │
                 ▼
┌─────────────────────────────────┐
│  Features extraction: Volume,   │
│  Orientation and Diameter       │
└─────────────────────────────────┘
                 │
                 ▼
┌─────────────────────────────────┐
│       Statistical analysis      │
└─────────────────────────────────┘
                 │
                 ▼
┌─────────────────────────────────┐
│      Model implementation       │
└─────────────────────────────────┘
```

Figure 4. 9: Block diagram of proposed method for ACL microCT Analysis.

4.3.1 Anterior cruciate ligament images

Micro-CT images of ACL specimens used in this study were acquired by a research group involving IRCCS Istituto Ortopedico Rizzoli and Alma Mater Studiorum – University of Bologna, as described in Marchiori et al. [18]. The scans were done using Micro-CT system (Skyscan 1176). Two ACL samples were used including the healthy sample from a cadaver donor (aged 40 years) and the pathological sample sample from a patient (aged 69 years) that underwent total knee replacement due to primary osteoarthritis. Both specimens were tensioned at different, increasing levels of strain (i.e., 1, 2, 3, 4, 5, 6 and 8 %). In addition, a scan was done to the sample without load and was set to 0 level. Hence, the microCT dataset comprised of 8 scans for each sample. The spatial resolution was 9 μm^3 isotropic voxel. Each sample was about 5mm

in thickness, and 1 mm was cut from the upper and lower extremities slices that occupied the patch clamp. In addition, the slice size was 2300×2300 pixel for both specimens while the number of slices was 459 and 461of the healthy and pathological stacked volumes respectively.

4.3.2 Pre-processing

The pre-processing step involved performing operations on 2D images with coordinates (x, y) in the following sequence:

- **Image Cropping**

In this preprocessing step, the acquired images were cropped to a specific size of approximately $40\% \times 60\%$ to reduce the computational time required for subsequent analyses. The selection of the appropriate image size was performed subjectively based on the loading levels being investigated. This step was crucial to reduce the size of the region of interest (ROI) in the image, resulting in a more efficient and accurate analysis.

For instance, the original image size of 2300×2300 pixels in x and y axes was reduced to 1000×1500 pixels to focus on the relevant region of the tendon or ligament under investigation. This approach ensured that only the necessary information was retained while reducing the overall computational burden of subsequent analyses.

- **Adaptive contrast enhancement**

This step aimed to highlight the ROI from the background as well as to preserve the low intensity pixels in the ROI. Therefore, it is important to enhance the image contrast before converting it into black and white, equation (13) and (14). The enhanced output image, with such a type of enhancement, preserves the low intensity pixel [62].

$$I(x,y) \ = \ M(x,y) \ + \ H \ (f(x,y) \ - \ M(x,y)) \quad (13)$$

$$H \ = \ \alpha \frac{M}{\sigma(x,y)} \quad , \quad 0 < \alpha < 1 \quad (14)$$

where, $I(x,y)$ is pixel value after enhancement, $f(x,y)$ is the input image, $M(x,y)$ is the Global mean, $\sigma(x,y)$ is the standard deviation and H , α are contrast ratio and contrast gain control, respectively.

■ **ROI selection**

An additional step to remove background noise is using morphological operations. Several techniques were applied to contrast enhanced images to obtain masked images including the entire ROI. The enhanced volume was first binarized and then the *regionprops* function was used to select the biggest ROI which includes the ACL tissues. Following that, the holes on the ROI which were produced from the previous step were filled using closing operation. Therefore, we obtained a proper mask after clearing the borders. The masked images were then multiplied by the raw images to select the ROI.

4.3.3 ACL fascicles measurements

Each volume of interest was analyzed using morphometric analysis to understand how ACL tissue structure and function change under strain. Three morphological parameters were calculated, including volume, orientation, and diameter. A 3D volumetric binary image was used to extract these parameters for each fiber bundle. Hence, we converted the intensity volume into a 3D binary image format, labelled the connected components, and used the label matrix to calculate each object's features.

We used the volume to extract the well-defined fascicles as well as to calculate the volume fraction parameters that will be used to build a mechanical model of ACL under various loads along the axial axis of the sample.

Since fibers carry much of the strength and stiffness along the fiber axis directions, the orientation of fascicles in ACL has a significant impact on the ACL mechanical properties.

4.3.4 Mathematical model of ACL stress-strain response

The mechanical properties of ACL are strongly reliant on their microstructures. The characterization of the ACL at varying strain levels is crucial to model viscoelastic behavior [20]. In this study, a conistitutive model is presented and implemented to investigate the mechanical properties of ACL under physiological and pathological conditions. Therefore, we adopted the mathematical model described in [21] to study the ACL stress/strain relationship based on tissue hierarchy. ACL was modeled based on a microstructural method where the contributions of the fibers to tissue behavior were adopted. The volume of tissue to be modeled is made up of a population of fibers in various states of "crimp" in the undeformed configuration. The first assumption is that, in the pre-loaded state inside microCT, ACL started full uncrimped [18]. Moreover, the fibers are assumed to be oriented in a mostly longitudinal direction. Thus, fibers are assumed to behave according to a constitutive law given as:

$$\sigma_{33}(\lambda_3) = 2\pi\lambda_3^2 v_f E_f \int_0^{\pi/2} R(\phi)\left(1 - \frac{1}{\lambda}\right)\sin\phi\cos^2\phi\,d\phi \qquad (15)$$

where σ_{33} is the axial normal stress. Stress in the tissue is calculated by summing the contributions of each fiber in the cross-section area. E_f: fiber elastic modulus, v_f: the fiber volume fraction; in such a way, the fraction of the fibers oriented with a certain angle is weighted by their volume with respect to the total tissue volume. $R(\phi)$: the orientation probability distribution function (PDF) and $R(\phi)\sin\phi\,\Delta\phi$ gives the proportion of the population of orientations (ϕ) bounded by the elemental joint range between ϕ and $d\phi$. The strain transformation required to define fibril deformation λ at any orientation ϕ is given in equation (16)

$$\lambda = \left(\lambda_3^2\cos^2\phi + \frac{1}{\lambda_3}\sin^2\phi\right)^{\frac{1}{2}} \qquad (16)$$

where λ_3 is the axial stretch-ratio of the fiber given experimentally.

To simplified equation (15) we substituted the integral $(\int)$ by the summation $(\sum)$ operation and we obtained equation (17)

$$\sigma_{33}(\lambda_3) = 2\pi\lambda_3^2 v_f E_f \sum_1^N R(\phi)\left(1 - \frac{1}{\lambda}\right)\sin\phi\cos^2\phi\,\Delta\phi \qquad (17)$$

where [1 : N] are the ϕ intervals from 0 to $\pi/2$ with dimension $\Delta\phi$. $R(\phi)sin\varphi\Delta\phi$ is defined as the angular frequency at each interval N [63].

4.3.5 Model implementation for calculation of the elastic modulus

A custom Matlab script was developed to determine the elastic modulus E_f from microCT data in input to the constitutive model described above.

Specifically, stress was calculated as force divided by cross sectional area. The elastic modulus was estimated for the healthy and pathological ACL by applying a linear regression model to the stress/strain data obtained for each level of strain (T0 -T8).

4.3.6 Statistical analysis

For comparison of fibril diameters between healthy and pathological ACL tissues we used diameter variance, while for comparison between tensile properties of more and less longitudinally aligned fascicles we used an energy and entropy function.

5   RESULTS AND DISCUSSIONS

In this section, we present the results obtained by our proposed method of highlighting ligament or tendon microstructures based on CE-microCT and multiscale Hessian filter in case study 1. Then, the ACL stress-strain relationship model based on the highlighting of the microstructural organization of the tissue is demonstrated in case study 2.

5.1 Case study 1: tendon and ligament

In this work, we presented a CE- microCT protocol addressing the need for clearly identifying the microstructure of soft fibrous tissues, such as tendons and ligaments. The main novelty of this work relies in targeting contrast enhancement by not only preparing the samples for optimal X-ray absorption, but also by selecting the best scanning protocols and integrating the whole analysis with a dedicated image processing protocol so as to optimize the identification of sample microstructure. In fact, the aim of this study was to demonstrate the feasibility of the proposed protocol from the starting phase of sample preparation to the final phase of volumetric image analysis letting for future works a proper quantitative validation. The proposed protocol was applied to a human hamstring tendon and a bovine collateral ligament, which results in being paradigmatic for the microstructure of soft fibrous tissues.

Specimens were subjected to sample preparation, followed by tomographic scan acquisition and data processing for 3D tomographic image reconstruction and finally segmentation and morphometric analysis.

5.1.1 The effect of contrast enhancement strategies

MicroCT images reconstruction and 3D rendering showed that the implemented HMDS drying protocol was able to fully contrast the tissue, Figure (5.1) illustrates the human hamstring tendon, while Figure (5.2) illustrates the bovine collateral ligament. On the other hand, , for contrast agent strategy, the obtained images showed that the

tissue should be exposed to the PTA solutions for at least 5 days to obtain a full contrast diffusion, see figures (5.3 and 5.4).
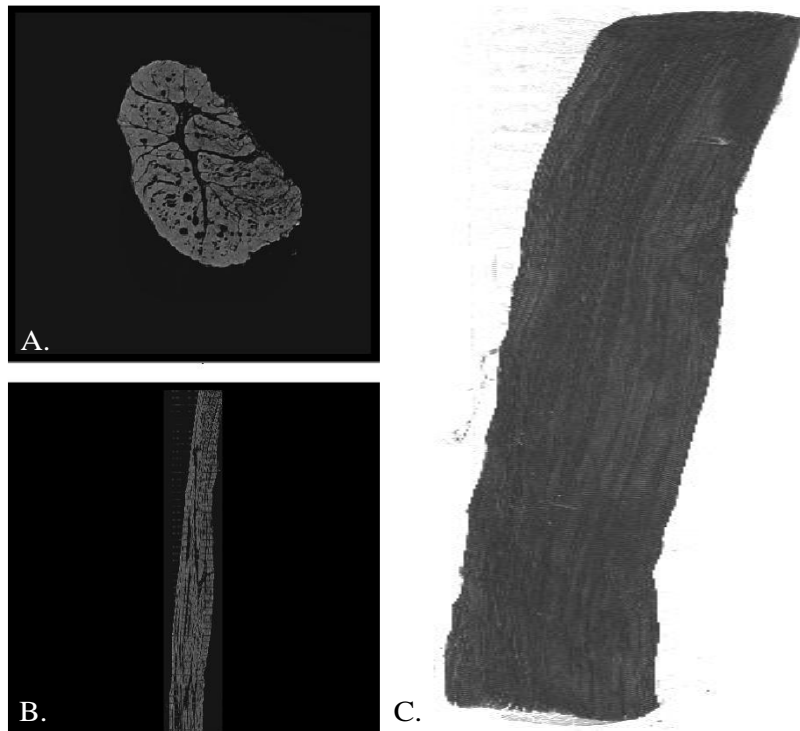
Figure 5. 1. MicroCT images of HMDS dried human hamstring tendon. (A) transversal mid slice, (B) sagittal mid slice and (C) 3D volume rendering.
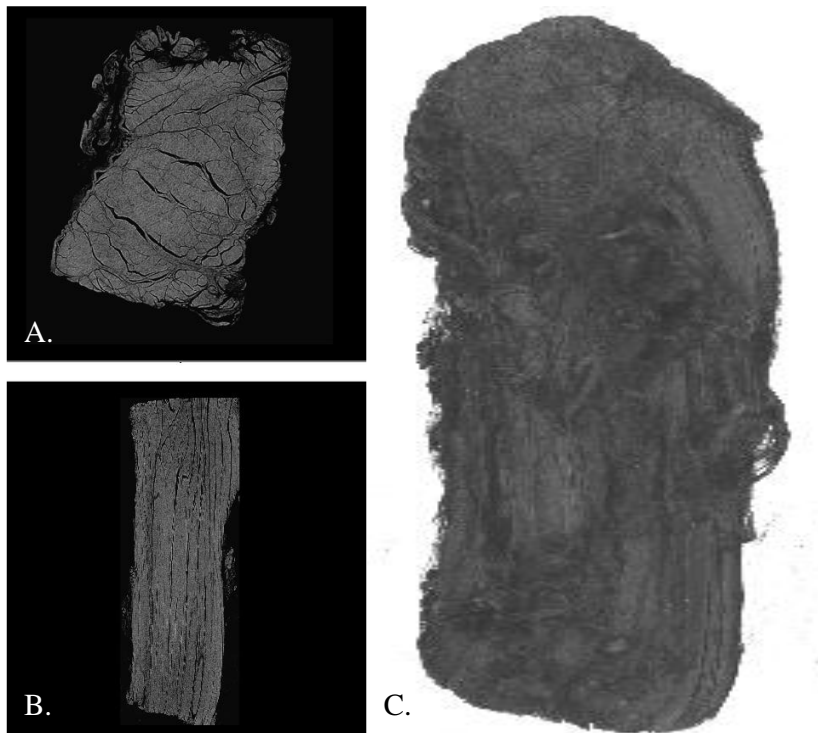
Figure 5. 2: MicroCT images of HMDS dried human hamstring tendon. (A) transversal mid slice, (B) sagittal mid slice and (C) 3D volume rendering.

In fact, Figure (5.3) and Figure (5.5) highlight the mid sections of the samples concerning the two contrast PTA protocols, i.e., in EtOH and H_2O, underlining the effects of temporal exposition. The same temporal progression can be qualitatively followed in Figure (5.4 and 5.6). The difference in optimal staining time, at the same concentrations, between the EtOH and water solution could be due to the difference in diffusion of water faster than EtOH. The use of PTA-staining overnight highlighted only the outer boundary of the tissues by microCT (Figure 5.3 and 5.5(A,D,G,J)). The visible portion of the fibrous tissues was found to increase with increasing staining duration (Figures 5.3 and 5.5). However, not all the sample exposed to PTA in EtOH was visible even after staining for 5 days (Figures 5.3 and 5.5(C,F,I,L)), with a central core remaining unstained.
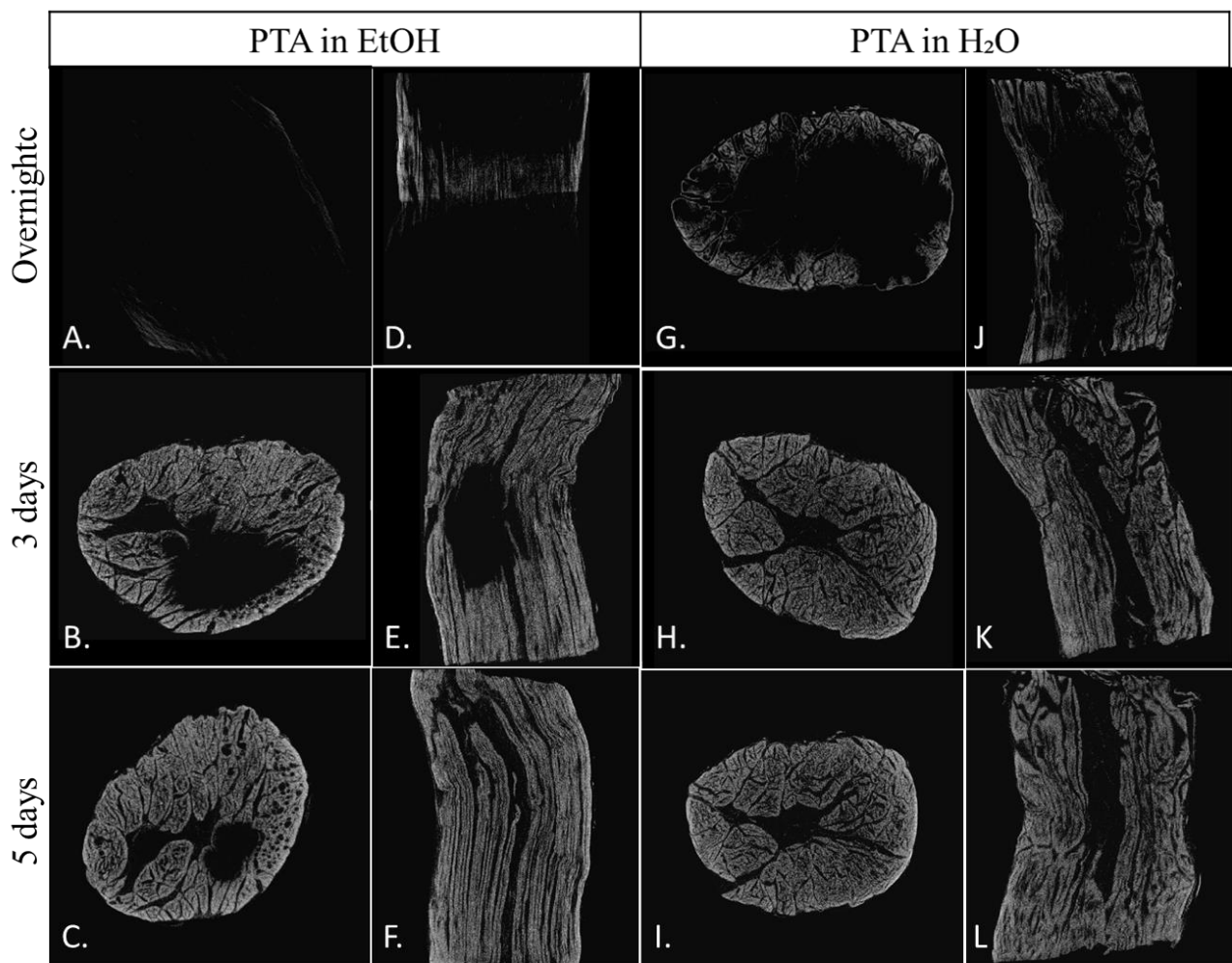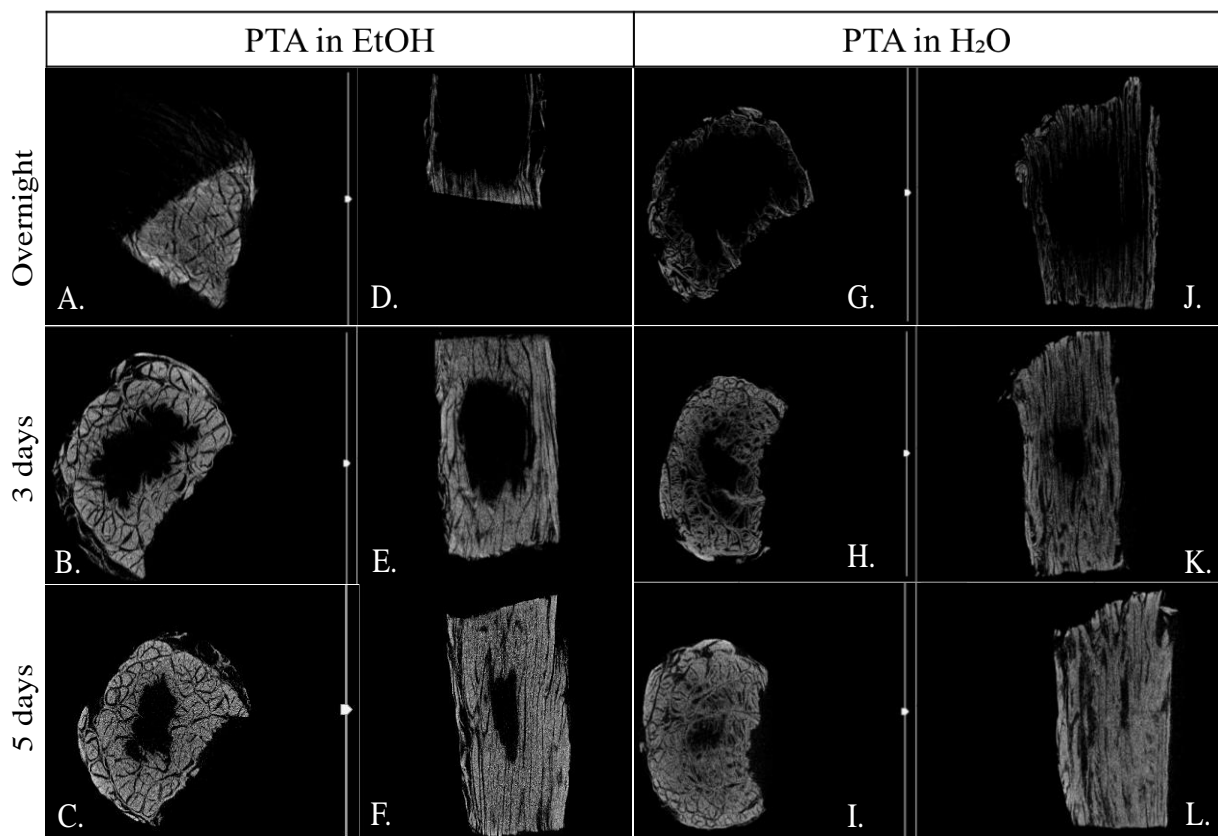

Figure 5. 3: Mid slices of microCT images of human hamstring tendon contrasted by 2% PTA in EtOH or in H_2O Overnight, for three days, and five days: (A-C) cross-sections and (D-F) longitudinal sections of PTA in EtOH; (G-I) cross-sections and (H-L) longitudinal section.
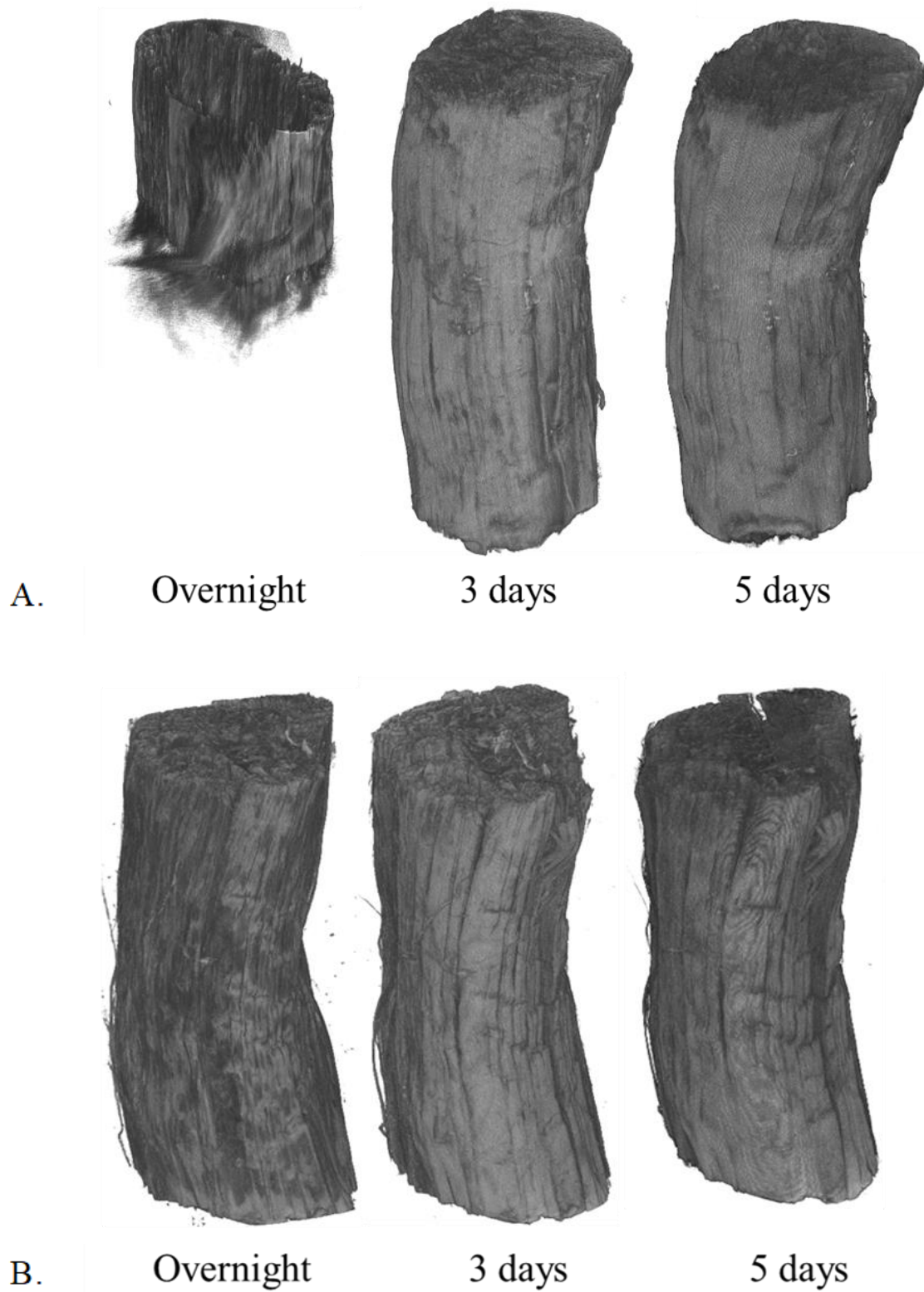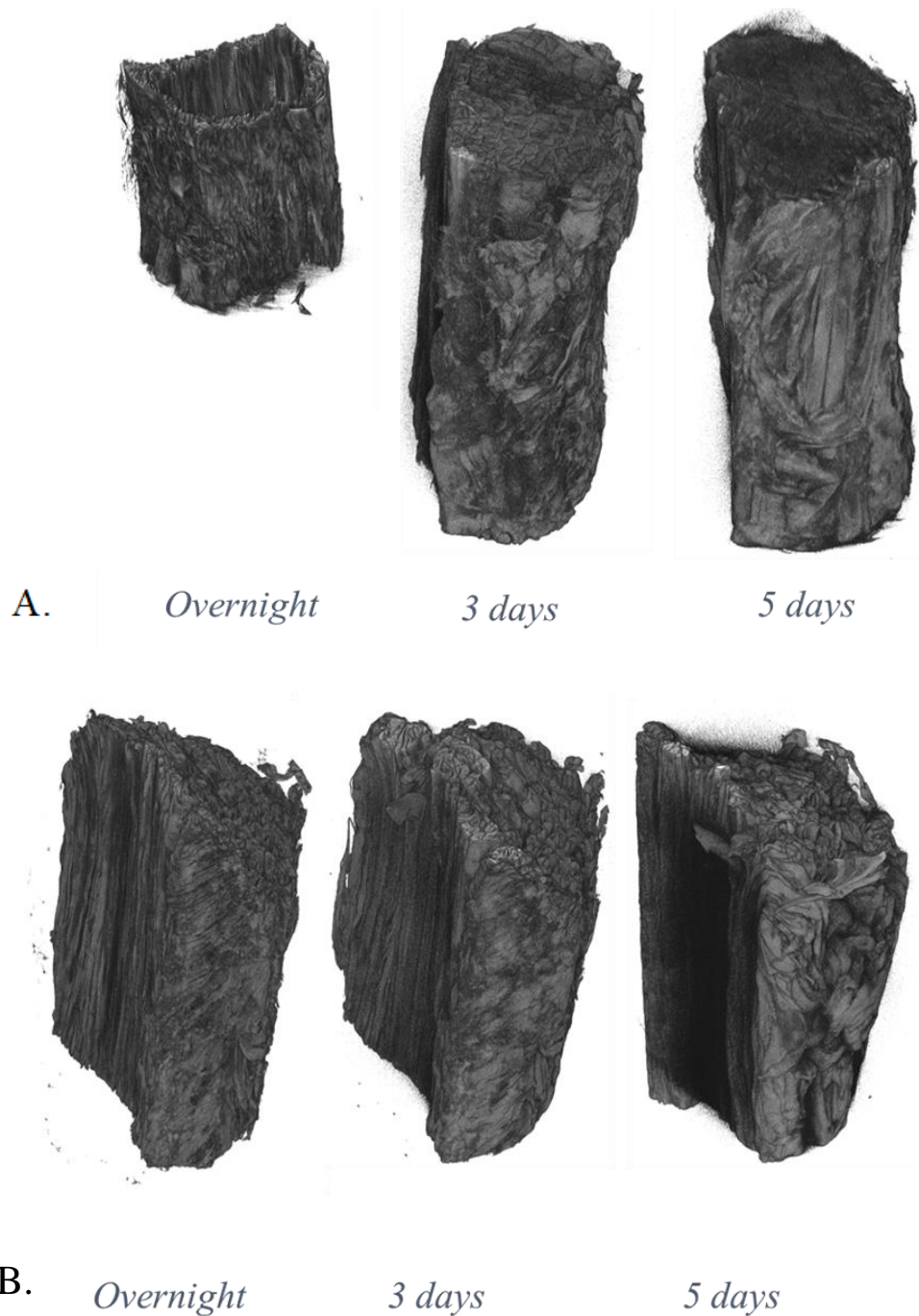
Figure 5. 4: 3D renderings of human hamstring tendon (A) PTA in EtOH and (B) PTA in H_2O contrasted sample at the three different exposure periods.

MicroCT resulted in contrasted tissue images for every tested sample preparation strategy, i.e., by exposition to PTA contrast agent in ethanol or in water solution, or by chemical drying. In this frame, it is worth discussing two main aspects, i.e., the workload for sample preparation and the possible tissue alteration due to the processes themselves. For what concerns the first issue, the workload was comparable between the different contrast enhancing strategies in terms of costs, times (about a week) and ease of preparation, as many steps are identical to those routinely used in the processing protocols of biological samples addressing histological analysis. Regarding the second aspect, a certain tissue "compaction" was more evident for chemical drying respect to PTA contrast; moreover, PTA in water could be less stiffening with respect to the other strategies, and thus preferable in terms of mechanical alteration [18].

Figure 5. 5: Mid slices of microCT images of bovine collateral ligament tendon contrasted by 2% PTA in EtOH or in H_2O Overnight, for three days, and five days: (A-C) cross-sections and (D-F) longitudinal sections of PTA in EtOH; (G-I) cross-sections and (H-L) longitudinal section.

A.   *Overnight*   *3 days*   *5 days*

B.   *Overnight*   *3 days*   *5 days*

Figure 5. 6: 3Drenderings of Bovine collateral ligament (A) PTA in EtOH and (B) PTA in H_2O contrasted sample at the three different exposure periods.

The microstructures of human hamstring tendon and bovine collateral ligament appear as grouped fascicles on microCT longitudinal sections, thus highlighting fibers bundles organized parallelly along the tendon main longitudinal axis. On the other hand, fibrous arrangement is less clear on transversal sections, overall, in the case of chemical drying. Indeed, even if collagen is the main matrix constituent, PTA solution is collagen

selective, whereas tissue chemical drying also maintains other solid components, see figures (5.1, 5.2, 5.3 and 5.5).

5.1.1 Computerised microstructures enhancement and processing

Raw microCT images were processed to highlight the microstructure of the tissue, in particular to reveal fibers/fascicles. Our first step was to select a VOI that includes only tissues to reduce execution time and to select the most contrasted and properly defined portion of the sample. Throughout all samples, this step was performed subjectively. Figure (5.7) illustrates an example of this step for the human hamstring tendon. Next, the VOI was normalized before applying the Hessian filter to enhance contrast. The third step was to apply the 3D Hessian filter. Figures (5.8, 5.9 and 5.10) illustrate the maximum input projection (MIP) of the normalized image and the processed image after applying the hessian filter of the human hamstring tendon while Figures (5.11, 5.12 and 5.13) are related to the bovine collateral ligament. In addition, the obtained microCT image contains some merged bundles that need to be split, so we used an open morphological operation with a 3D line structure element to overcome this issue.
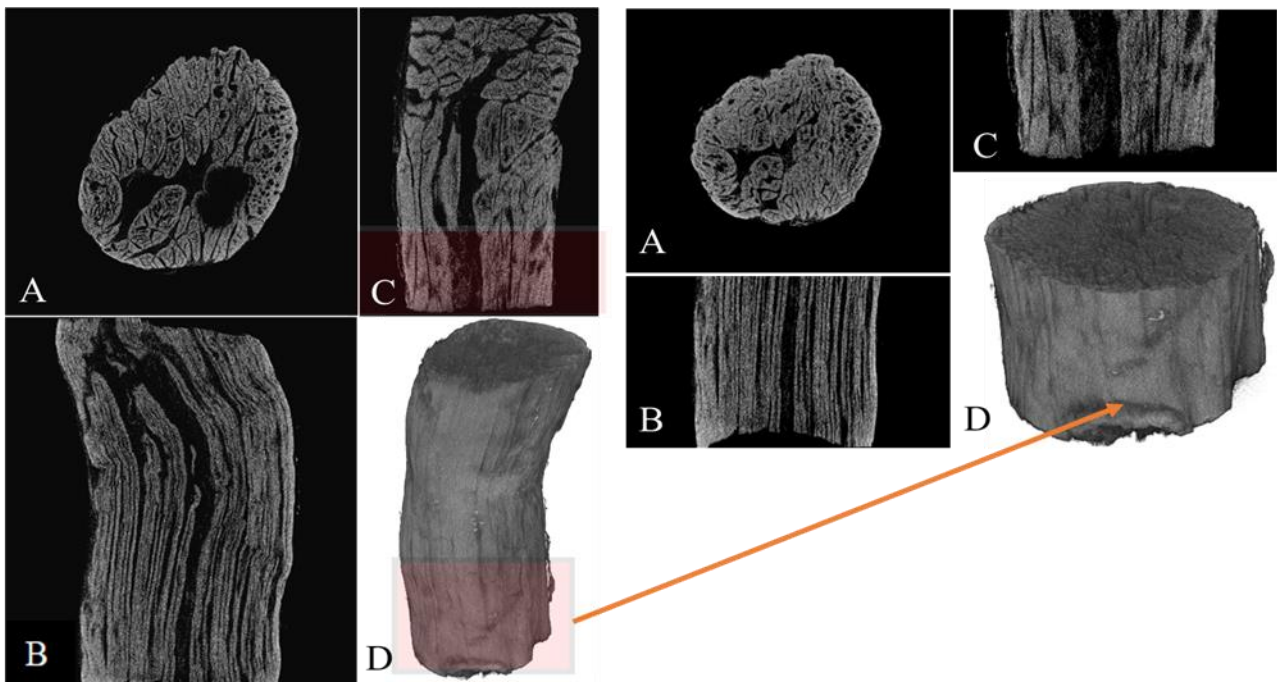
Figure 5. 7: An example the VOI selection of human hamstring tendon staining with PTA in EtOH: (A) transversal, (B) sagittal and (C) lateral views of the mid slice, and (D) 3D volume rendering.

MIP of the input image after normlization

MIP of the output image (Hessian)

Figure 5. 8: MIP of the human hamstring tendon PTA in H_2O (upper) normalize volume, and (lower) Hessian enhancement volume.

MIP of the input image after normlization
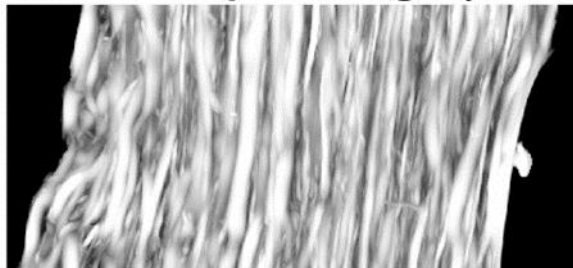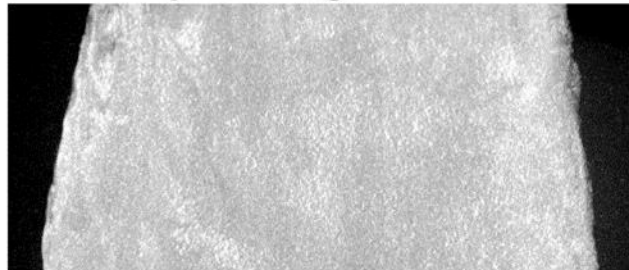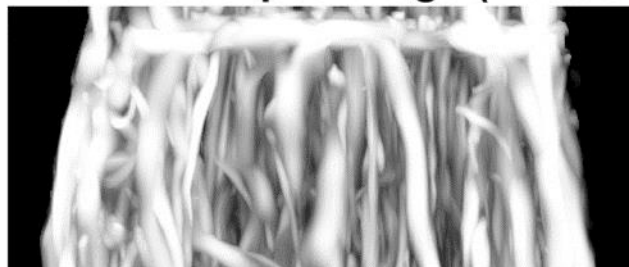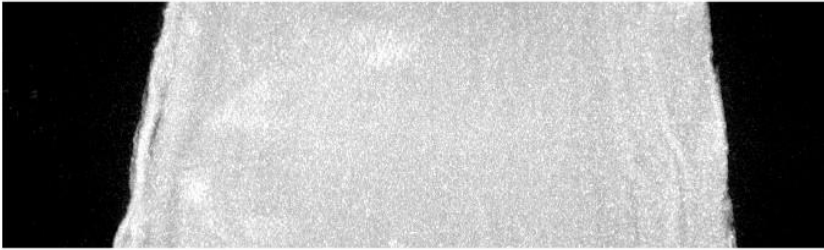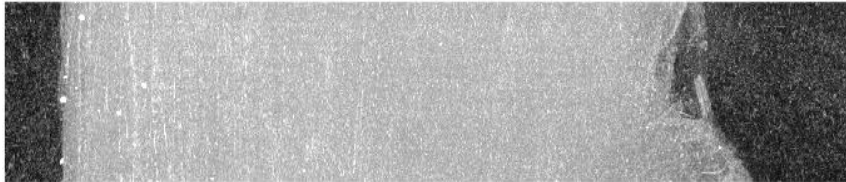

MIP of the output image (Hessian)
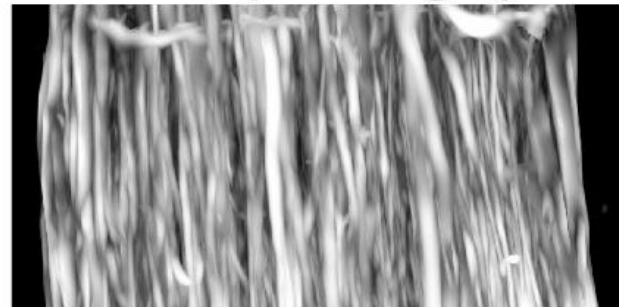
Figure 5. 9: MIP of the human hamstring tendon PTA in EtOH (upper) normalize volume, and (lower) Hessian enhancement volume.

MIP of the input image after normlization
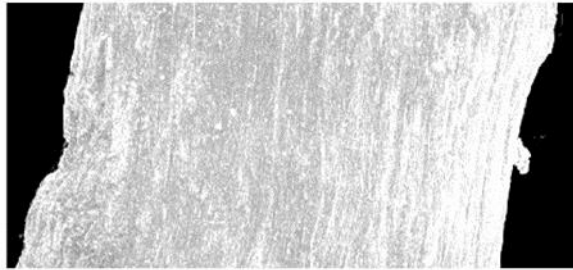
MIP of the output image (Hessian)

Figure 5. 10:MIP of the human hamstring tendon HMDS dried (upper) normalize volume, and (lower) Hessian enhancement volume.

MIP of the input image after normlization

MIP of the output image (Hessian)

Figure 5. 11: MIP of the bovine collateral ligament PTA in H_2O (upper) normalize volume, and (lower) Hessian enhancement volume.

MIP of the input image after normlization

MIP of the output image (Hessian)

Figure 5. 12: MIP of the bovine collateral ligament PTA in EtOH (upper) normalize volume, and (lower) Hessian enhancement volume.

MIP of the input image after normlization

MIP of the output image (Hessian)

Figure 5. 13: MIP of the bovine collateral ligament HMDS (upper) normalize volume, and (lower) Hessian enhancement volume.
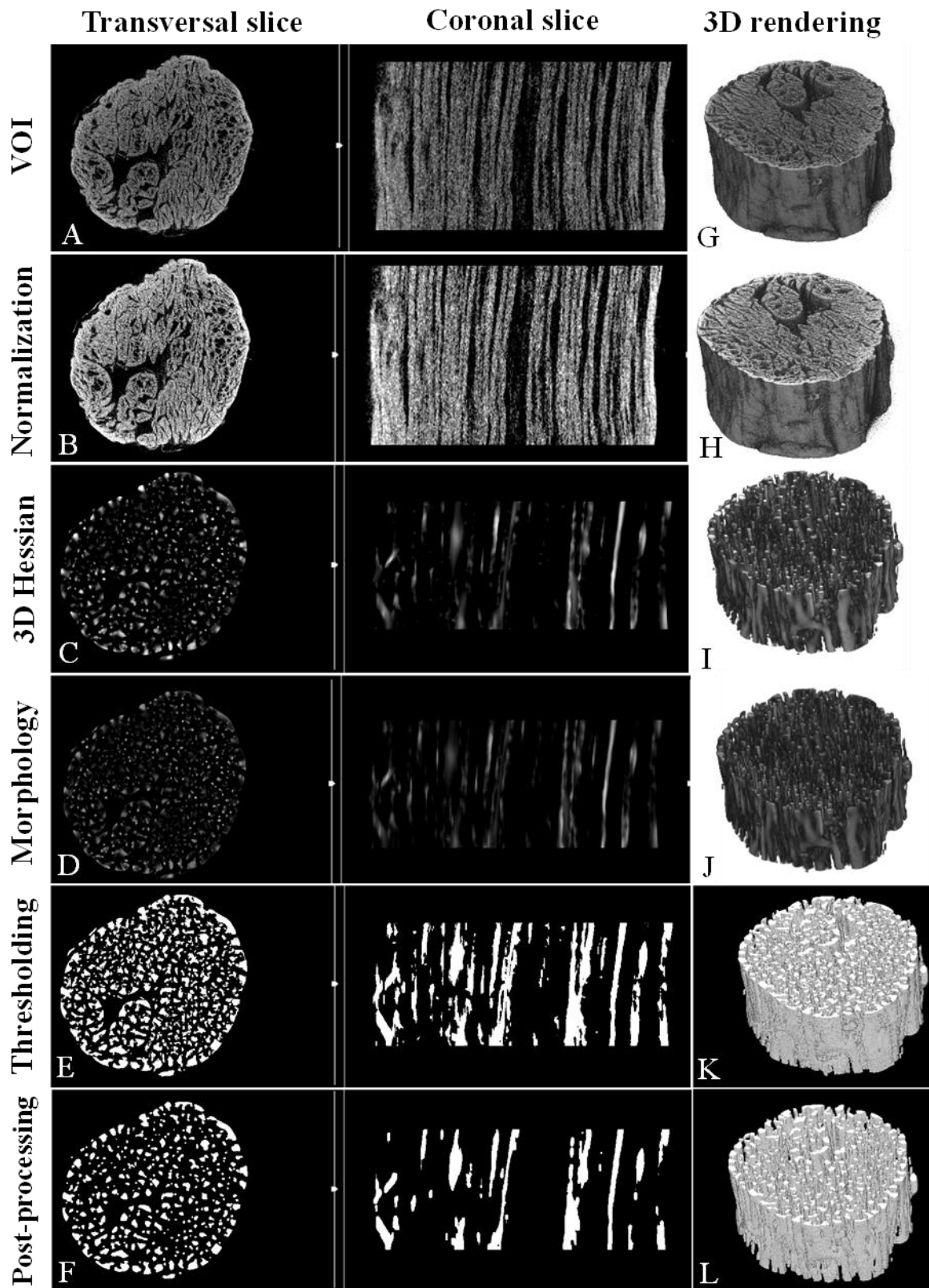
Figure 5. 14: Image processing steps to reveal the tendon fibers/fascicles by CE-microCT. (A-F) are the transversal and longitudinal 2D views of a middle slice: (A) raw microCT images; (B) contrast enhancement using normalization; (C) fascicles segmentation based on 3D Hessian multiscale filter; (D) Morphological operation to split merged structures and emphasise their edges; (E) thresholding to convert image into binary scale for the purpose of features extraction; (F) post-processing step including morphological enhancement; (G-L) are the corresponding 3D rendering visualizations.
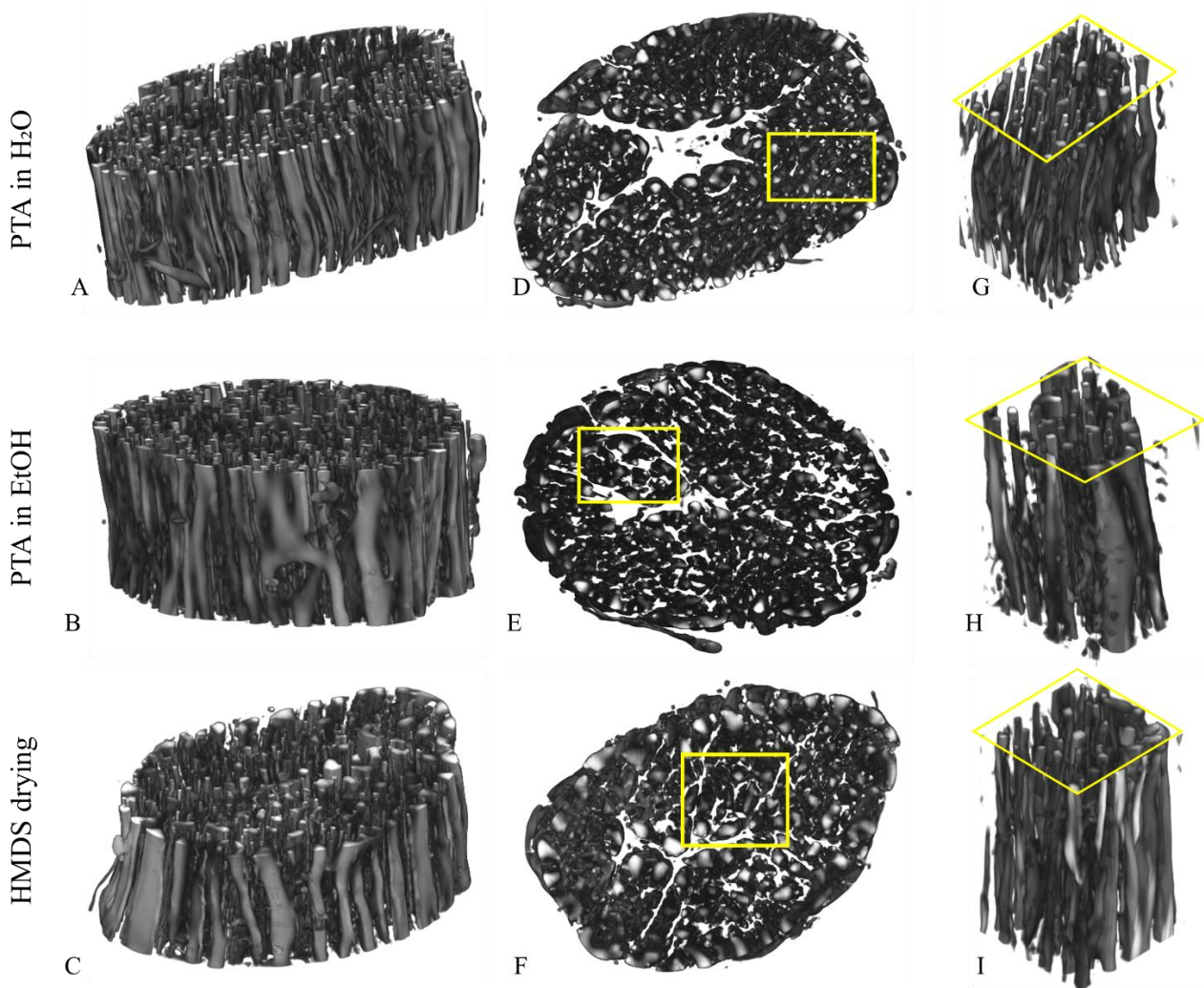
Figure 5. 15: Human hamstring tendon fascicles enhancement using 3D Hessian filter. 3D rendering visualization of the microCT processed images: (A,D,G) P TA in H_2O, (B,E,G) P TA in EtOH and (C,F,I) HMDS dried sample; (A-C) prospective view, (D-F) cross-sectional view, and (G-I) sub-volumes magnified to highlight the presence of tendon fascicles.

A threshold was applied to distinguish the fascicles from the non-fascicles signal. Therefore, CT images were binarized based on adaptive threshold on the processed images. Due to the grouped nature of the microstructures of interest, detecting individual fascicles in the image was a challenge. Therefore, morphological filters were then applied to separate touching fascicles to estimate the size and orientation of individual bundles, see Figures (5.14, E, F, and K, L). By further focusing on the microCT image processing, we can underline two macroscopic effects: (i) tissue image contrast becomes comparable when considering both PTA exposed samples and chemical dried ones; (ii) a fibrous structure is highlighted and can be segmented for any tissue sample, within a sort of "skeletonization" approach. By using the proposed

approach, fibers/fascicles become well separated and identifiable, although several small portions of the tissue can be lost, see Figures (5.14 and 5.15).

In order to compare the different tissue contrast strategies and the effect of image processing, contrast profiles on transversal Figure (5.16) and longitudinal Figure (5.17) sections were drawn on raw and processed microCT images. Focusing on reconstructed microCT images, the contrast between tissue material and background/voids was more enhanced by PTA approach with respect to chemical drying as example for human hamstring tendon (see Figures 5.16 and 5.17).

5.1.2 Analysis of fibres diameter and orientation

Following binarization steps, well-defined fascicles were selected according to the following criteria:

1. The objects with small volumes were excluded since they are are probably artifacts, or at least not fibers.

2. The largest objects, which are the merged fascicles, were excluded.

The final candidates (i.e., fibers/fascicles) are obtained and can be analyzed for geometrical characteristics; in particular, for each tissue sample, the microstructure was described by the distribution of fiber diameters with respect to perpendicular axis and orientations with respect to the longitudinal axis, Figure (5.18 and 5.19). Nevertheless, transverse processed sections show the microstructures as irregular circular structures of varying sizes; for this reason, in this form of the protocol, orientations measurements appear more reliable than diameters for the same revealed microstructural elements. Indeed, orientation analysis seems to quantitatively confirm what we qualitatively observed above, i.e., a strong fibrous alignment along the longitudinal axis of the specimen, without underling important differences between contrast strategies. Moreover, compared to the tendon, the ligaments fibers are arranged in a less parallel fashion (Figure 5.18 and 5.19).

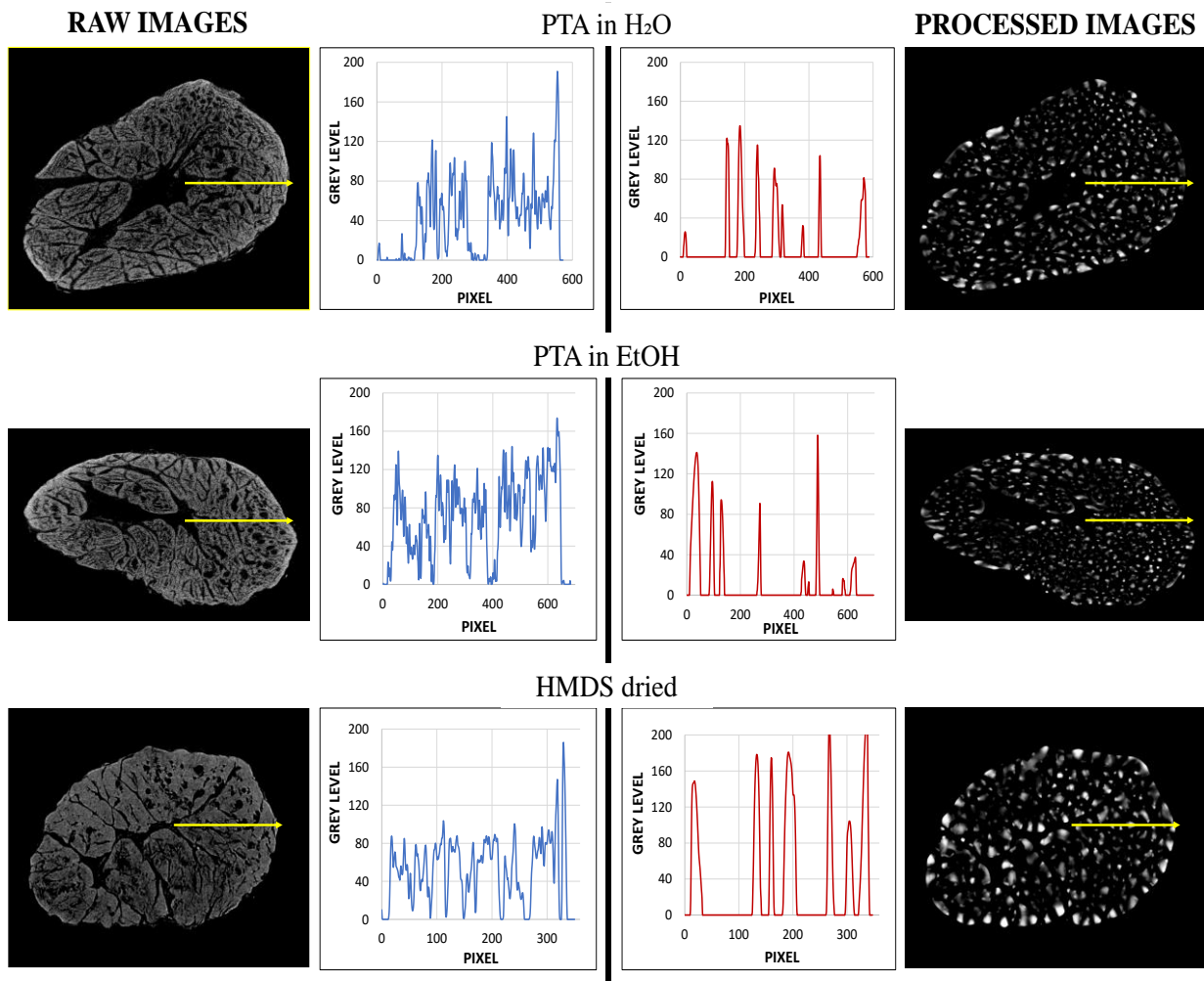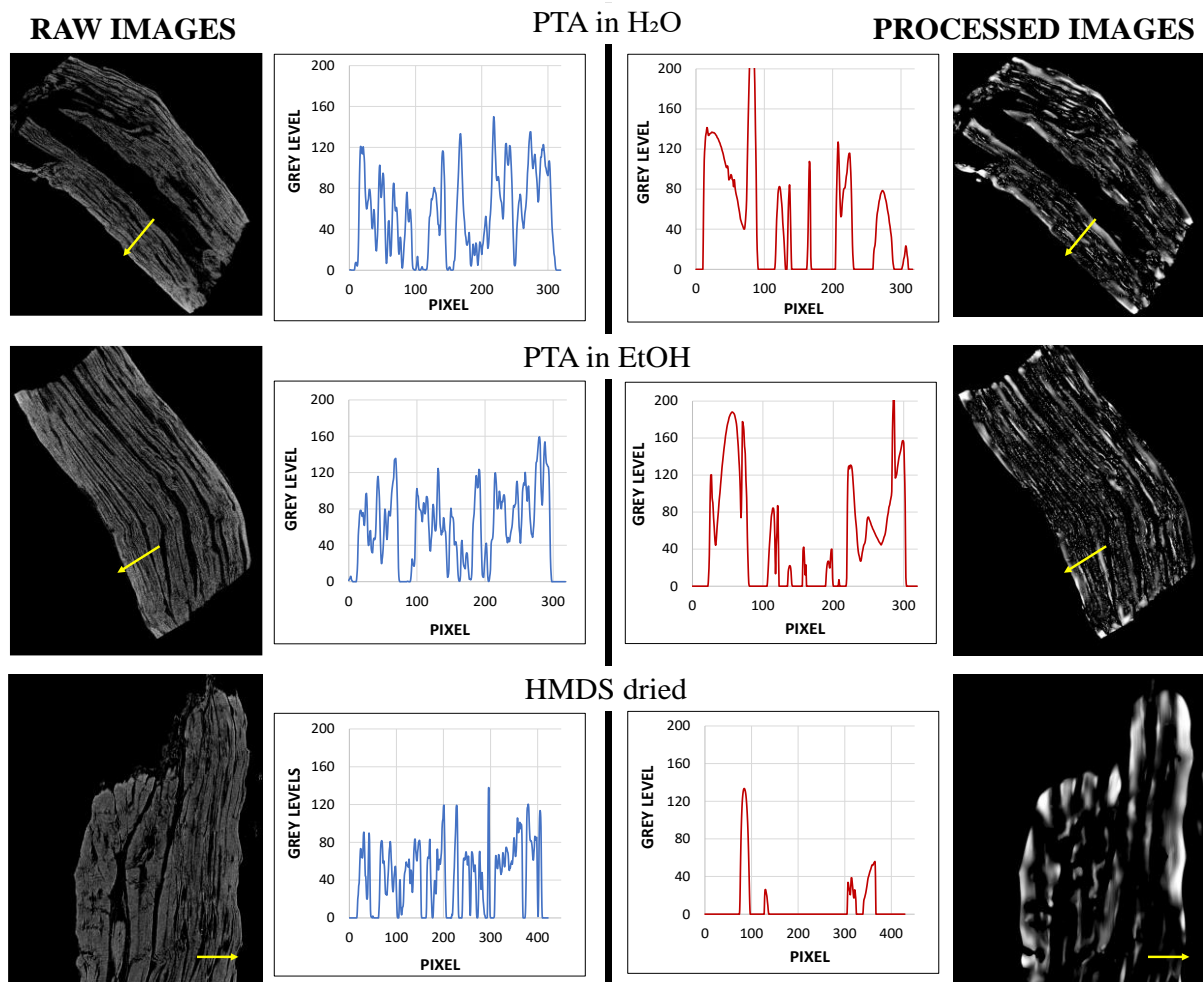| RAW IMAGES | PTA in H$_2$O | | PROCESSED IMAGES |

PTA in EtOH

HMDS dried

Figure 5. 16: Transverse plane slices of raw and processed microCT images coupled with contrast (grey level) profiles relative to the yellow arrow path on each image for the 5 days P TA in H$_2$O sample, 5 days P TA in EtOH and HMDS dried sample.

5.1.3 Qualitative validation via histology

Finally, histological sections permitted a visual, qualitative (not on the same physical sections), evaluation of the material and image processing in terms of fibrous tissue contrast enhancement and segmentation, Figures (5.20 and 5.21). In general, the fibrous and lobular arrangements, as obtained at the end of the image processing protocol, appeared in agreement with histological sections.

In terms of validation, measurements on histological images could represent a reliable standard control. For example, the observation under polarized light - as we reported here - allows the detection of anisotropic structures (visualized as bright or shiny objects on a dark background), which can be easily compared with microCT processed

images; the different colours of the collagenic network are usually associated with the predominance of a type of collagen (yellow-red strong birefringence with thick fibers for collagen type I, weak greenish birefringence with thinner fibers for collagen type III). However, many factors can influence birefringence colours, such that might alter the tissue and consequently introduce bias in histological comparison. For instance, chemical drying may induce a tissue alteration according to the aqueous content due to water evaporation; in fact, PTA exposition can favour a shrinkage of tissue [16]. Finally, we should highlight the different birefringence colour obtained in the different histological sections (Figures 5.20 and 5.21). which might be related to different sample preparations.

Figure 5. 17: Longitudinal plane slices of raw and processed microCT images coupled with contrast (grey level) profiles relative to the yellow arrow path on each image for the 5 days P TA in H_2O sample, 5 days P TA in EtOH and HMDS dried sample.
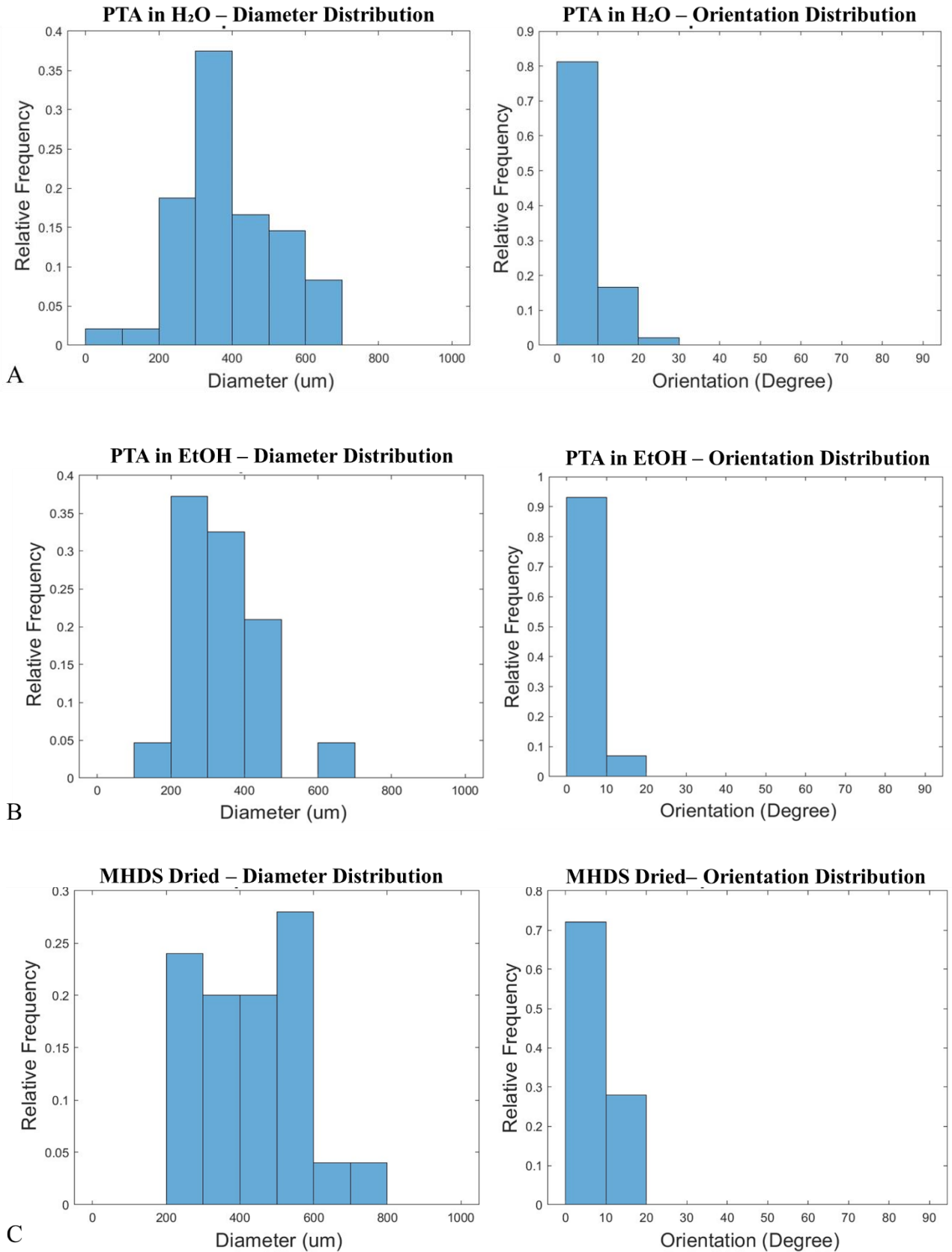
Figure 5. 18: Frequency histogram of the human hamstring fiber diameters (left line) and orientations (right line) for the (A) PTA in H_2O, (B) PTA in EtOH and (C) HMDS dried sample.
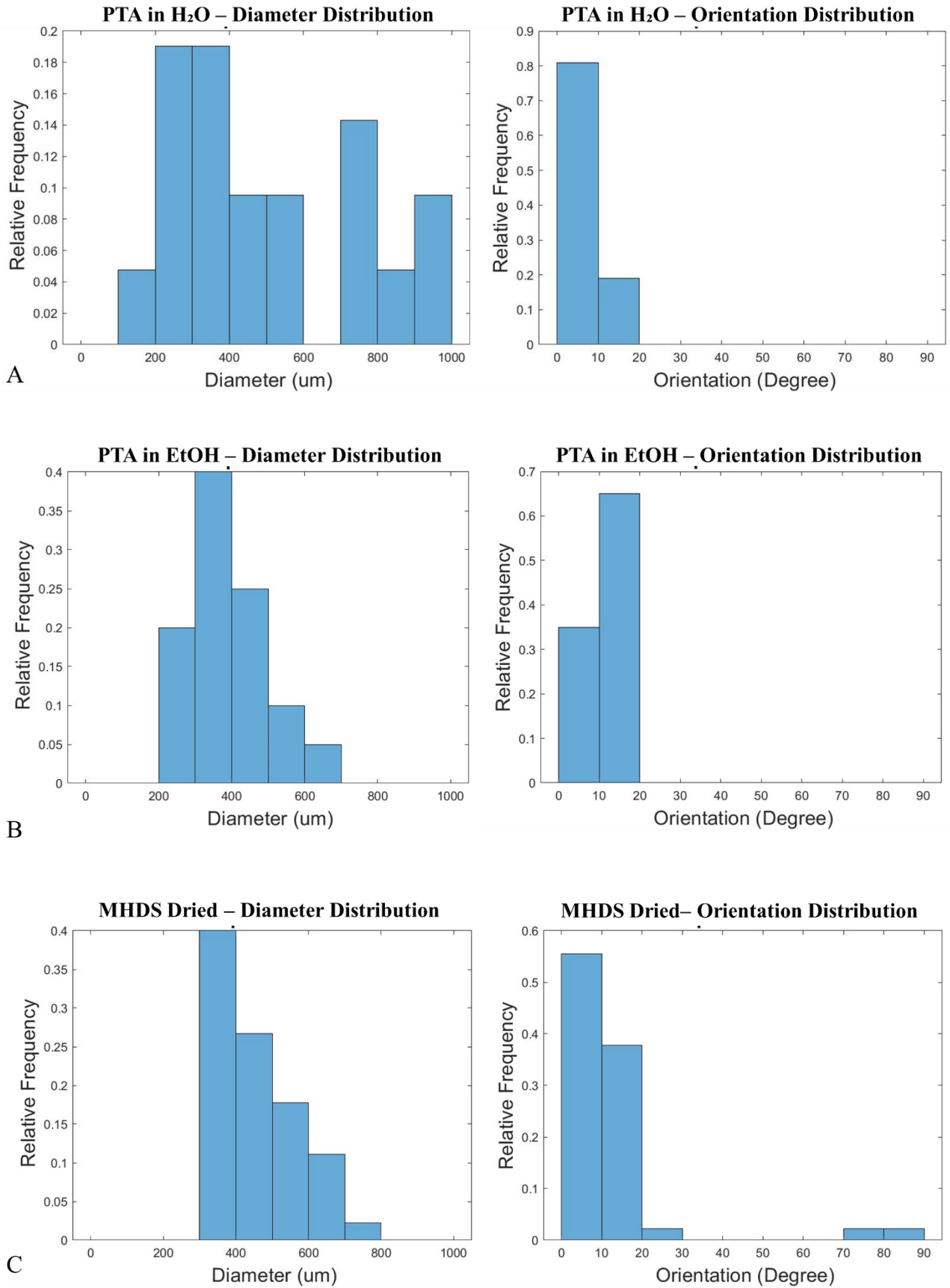
Figure 5. 19: Frequency histogram of the bovine collateral fiber diameters (left line) and orientations (right line) for the (A) PTA in H$_2$O, (B) PTA in EtOH and (C) HMDS dried sample.
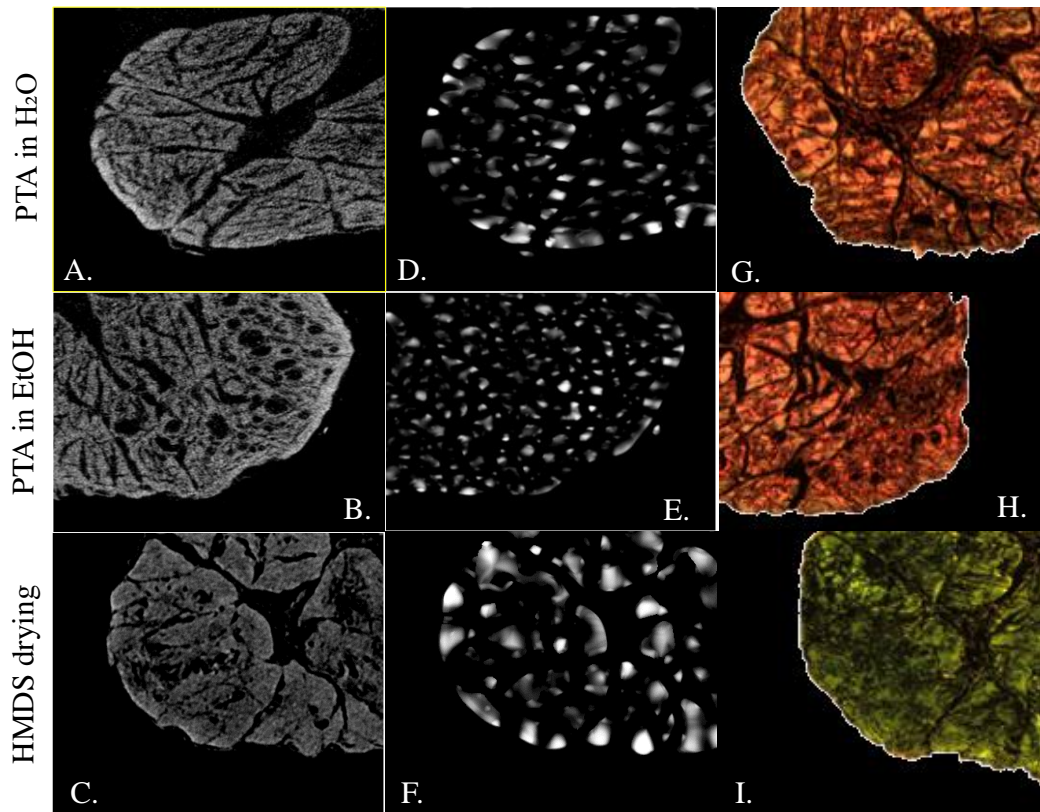
Figure 5. 20: Zoom on transversal microCT raw (A, D, G), processed (B, E, H) and picrosirius stained histological (C, F, I) sections for the PTA in H_2O (A, B, C), PTA in EtOH (D, E, F) and HMDS dried (G, H, I) sample.
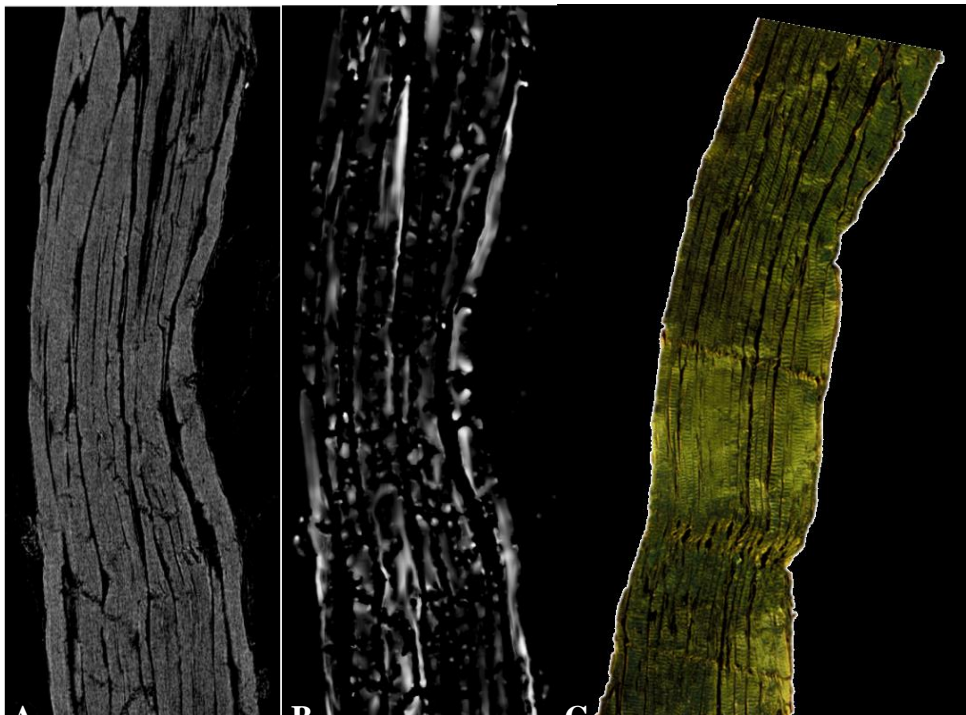

Figure 5. 21: Longitudinal microCT raw (A), processed (B) and picrosirius stained histological (C) section for the HMDS dried sample.

A further important aspect of the CE-microCT protocol here introduced is its capability to investigate big portions of tissue, in the order of cm, with a high spatial resolution in the order of µm. Indeed, even if not able to resolve the collagen nanofibers, fundamental element of the hierarchical structure of ligaments and tendons, this solution appears able to highlight their typical fascicular structure and bundle arrangement [64], in the order of hundreds of µm (Figure 5.18 and 5.19).

Therefore, even if not able to reach the quantitative fiber tracking obtained, for example, by Sartori and Stark with analogous, but more articulated, methods realized only on very small animal samples [23], this work represents an advancement with respect to similar applications [65,66]. Therefore, the presented integrated approach can have an important impact on the realization of physio-pathological and functional *ex vivo* studies on big animal models and human samples. The main limitation of this study relies on the fact that this work represents only a preliminary descriptive phase of the overall CE-microCT protocol; indeed, image processing shows margins of improvement in not losing tissue information and a strong quantitative validation based on a deeper histological analysis results to be mandatory. Concerning image processing, the misinterpreted fascicles in the processed VOI after applying Hessian filter can be mainly ascribed to background artifacts and noise; in fact, the merged fascicles are generally located on the sample edges, whereas the disconnected ones appear on the sample core where the intensity values are low due to absorption inhomogeneity. Hence, both the filter parameters themselves and the sample properties impact the performance of the Hessian filter [67].

A further limitation is related to the application of the protocol to only a human hamstring tendon and a bovine collateral ligament, while it should be tested on more kinds of soft tissues, including different tendons and ligaments. Further work to overcome all these limitations are recommended, nevertheless with this study we introduced an important tool for performing 3D microstructural analyses of soft fibrous tissues.

5.2 Case study 2: structure and mechanical behaviour of ACL

MicroCT images that were used in this project derives from two specimens harvested from two different subjects. The first one comes from a healthy subject (40 years old) without knee pathologies and the second one comes from a subject (69 years old) who underwent total knee replacement due to primary osteoarthritis. It should be noted that both specimens were tense at different levels of strain (e.g., 1, 2, 3, 4, 5, 6, 7 and 8 %), representing the T1 to T8 range and the T0 level of the tissue sample without any load.

5.2.1 Computerized microstructures enhancement and processing

The raw microCT images of the healthy and pathological samples without loading (T0 level) which are shown in figure (5.22) were processed in multiple stages to enhance the grayscale contrast between the fascicles and non-fascicles structures of the ACL tissues, as previously described. Then, the segmented microstructures were analyzed to get the volume, diameter, and orientation respect to e main longitudinal axis of each bundle. Finally, the statistical analysis for the fibers diameter – based on variance and for the orientation – based on entropy and energy were computed.
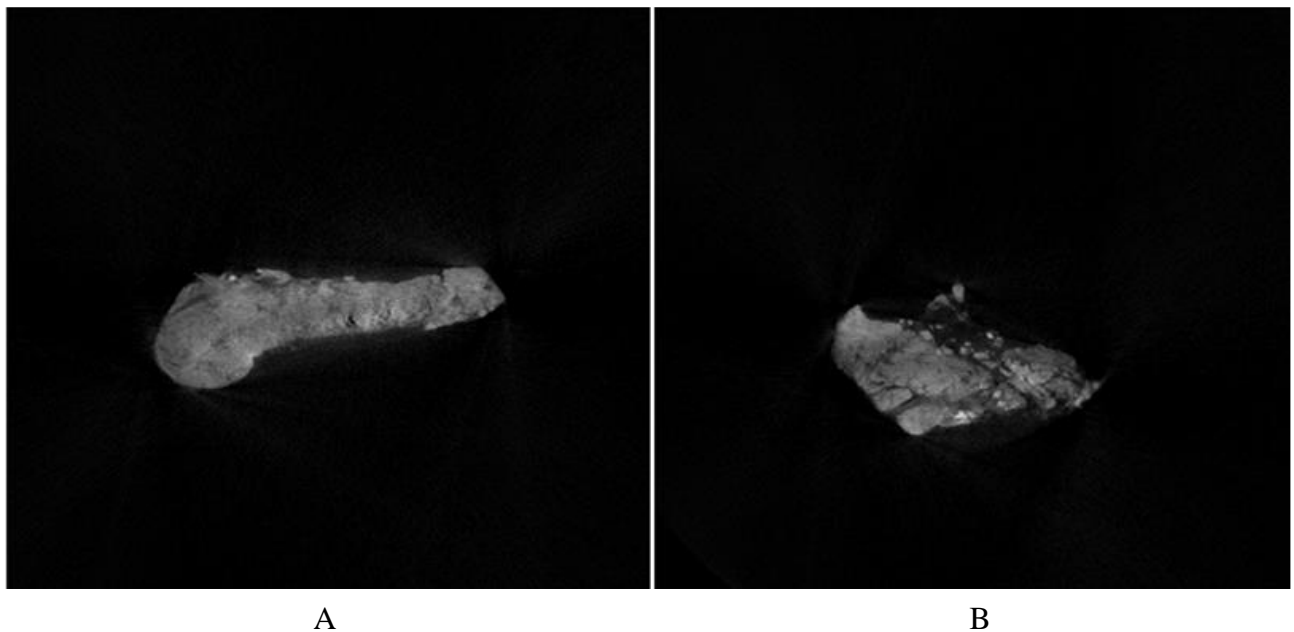

| A | B |

Figure 5. 22:Raw Micro CT cross section slice of the ACL (A) healthy specimen, and (B) pathological specimen.

Adaptive contrast enhancement is essential to enhance the image contrast before converting it into black and white. Figure (5.23) shows the processing with and without adaptive contrast enhancement. Due to it, the background artefact can be removed without affecting our ROI. An additional step to remove background noise is by using morphological operations. This technique was applied to contrast enhanced image Figures (5.24 and 5.25). Moreover, Figures (5.26, 5.27, 5.28 and 5.29) show the 3D images rendering of the pre-processed step.
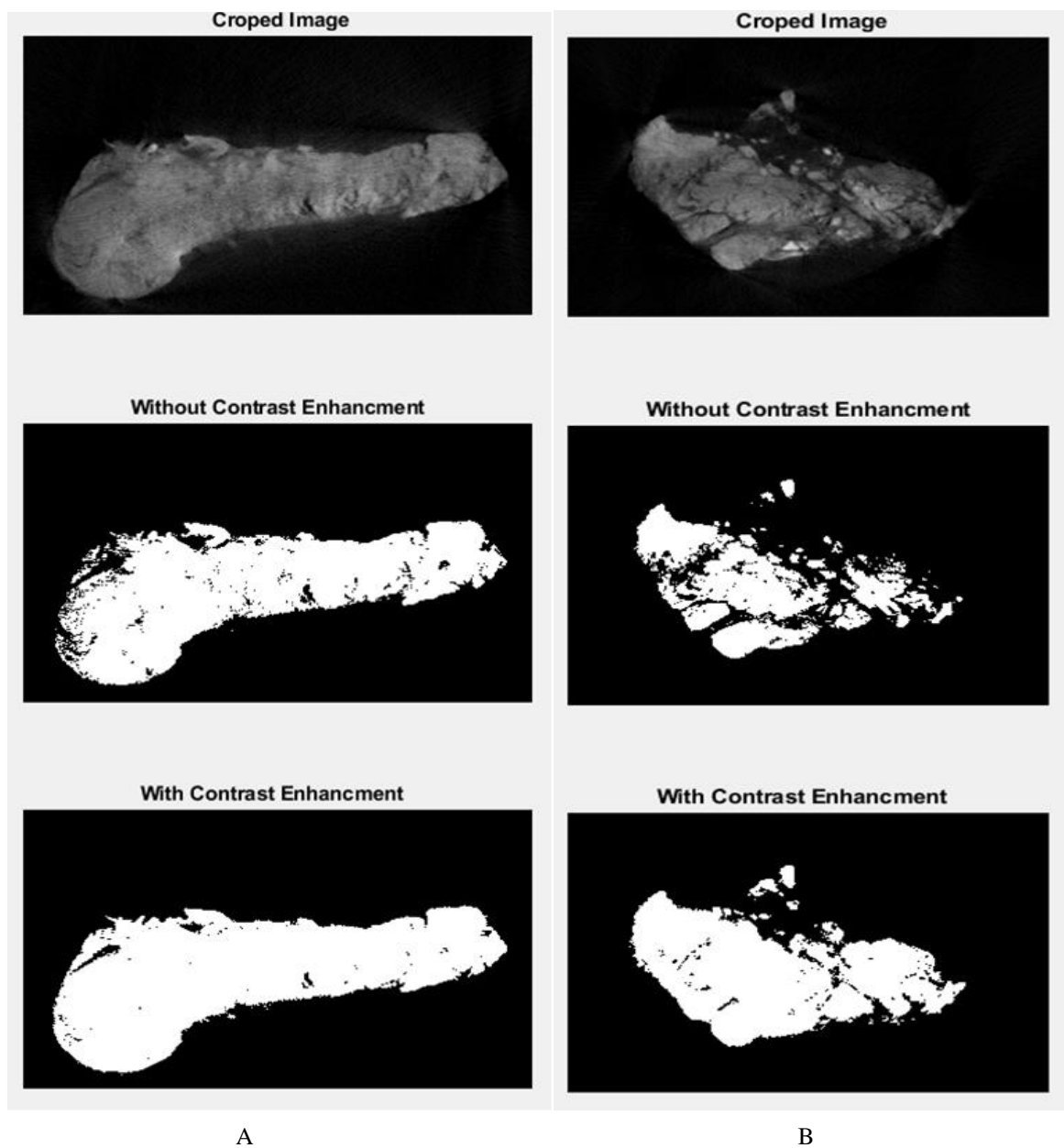
Figure 5. 23: MicroCT Images demonstrates the preprocessing steps from top to bottom cropped images and the effect of adaptive contrast enhancement on the binarization step (A) healthy specimen, and (B) Pathological specimen.
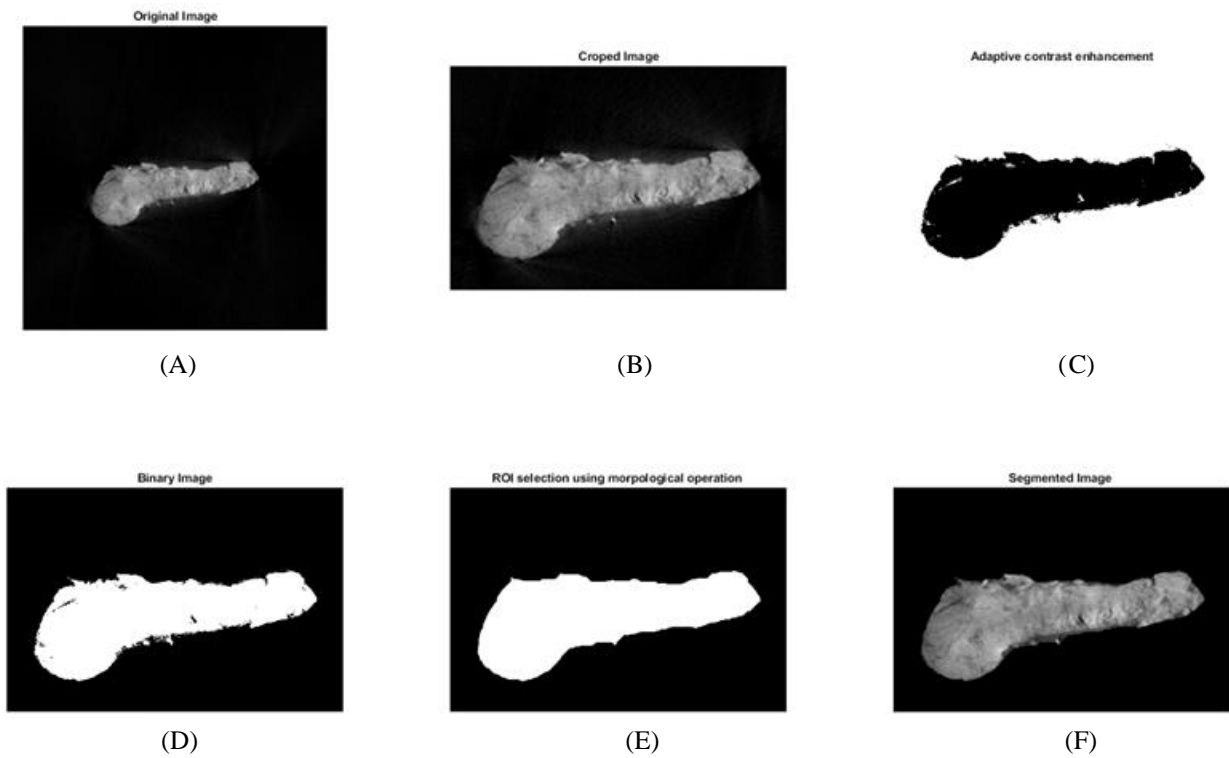
Figure 5. 24: The preprocessing steps of cross-sectional slice example for healthy specimen :(A) Input Image, (B) Cropped Image, (C)Enhanced image using adaptive contrast approach (D) Binary Image, (E) ROI selection using Morphological operation), and (F) Segmented Image.
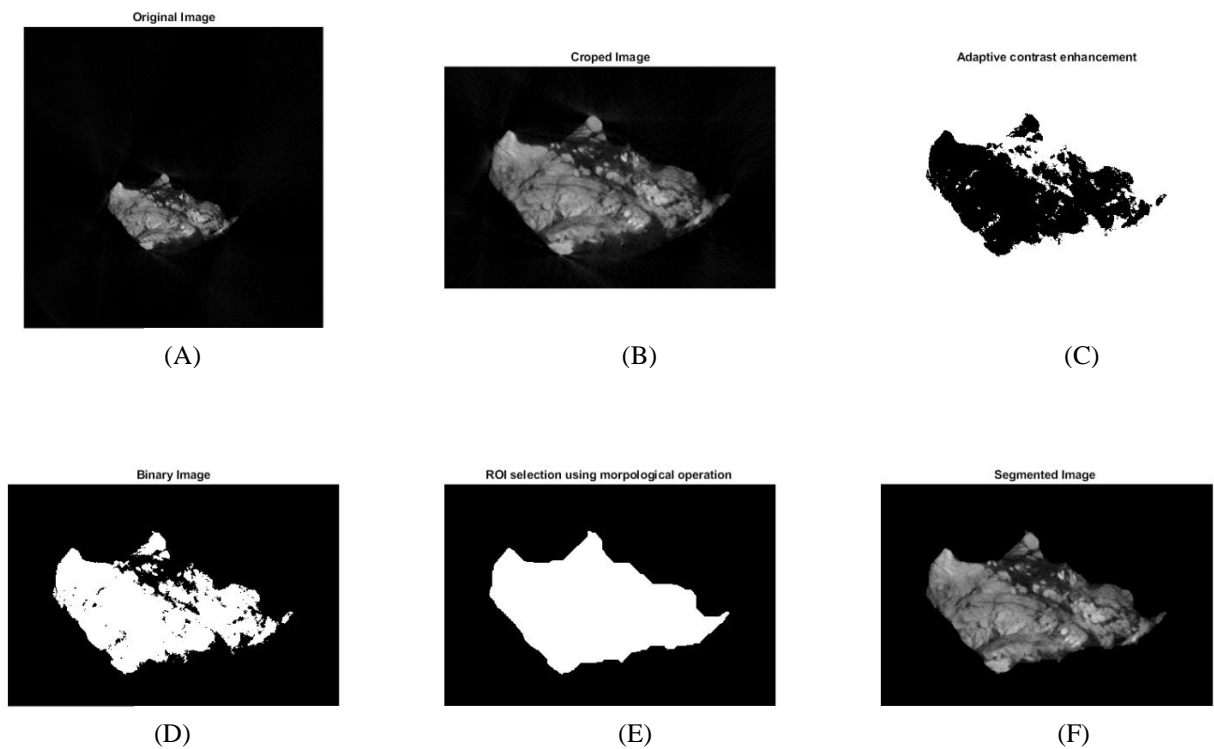

Figure 5. 25: The preprocessing steps of cross-sectional slice example for pathologic specimen :(A) Input Image, (B) Cropped Image, (C)Enhanced image using adaptive contrast approach (D) Binary Image, (E) ROI selection using Morphological operation), and (F) Segmented Image.
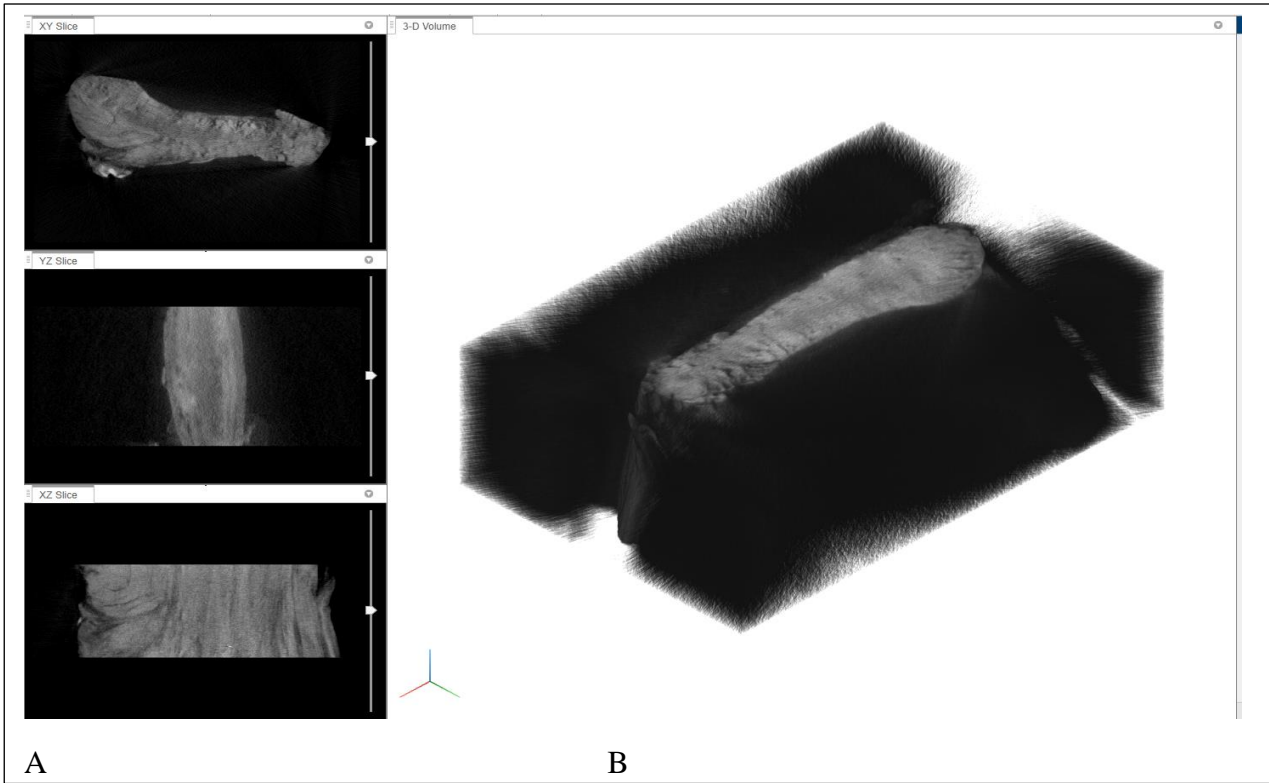
Figure 5. 26: Original cropped microCT image of the healthy specimen: (A) 2D view of the middle slice in XY, YZ, and XZ plane. (B)3D volume rendering.
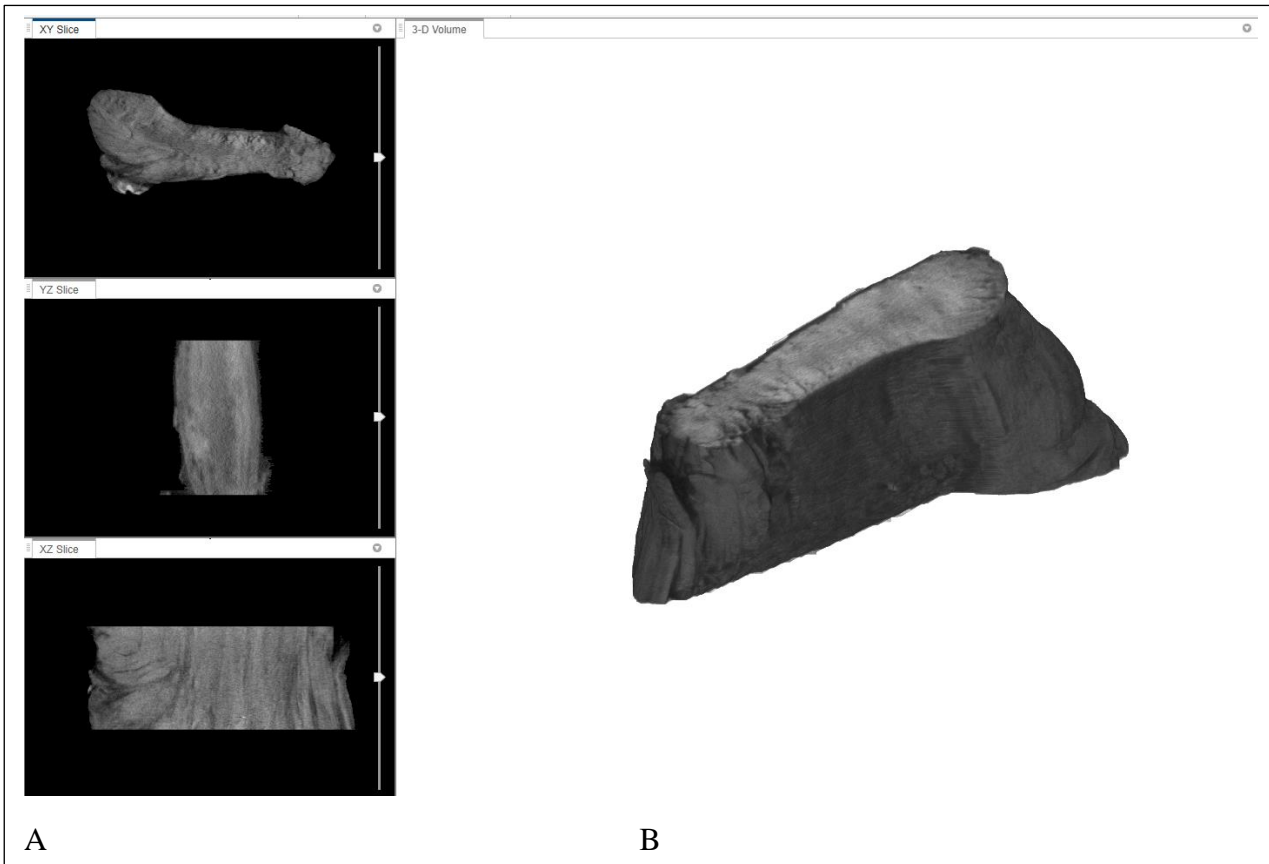

Figure 5. 27:Processed microCT image of the healthy specimen: (A) 2D view of the middle slice in XY, YZ, and XZ plane. (B)3D volume rendering.
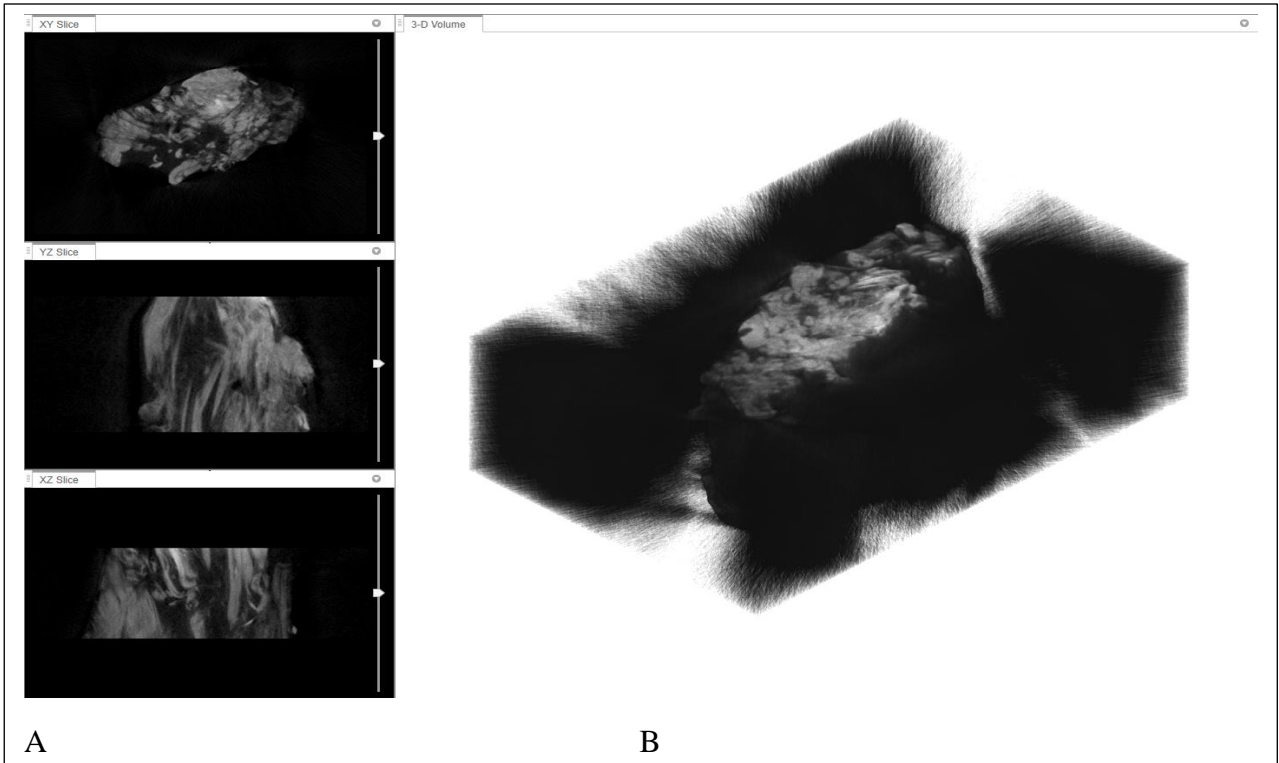
Figure 5. 28: Original cropped microCT image of the pathological specimen: (A) 2D view of the middle slice in XY, YZ, and XZ plane. (B)3D volume rendering.
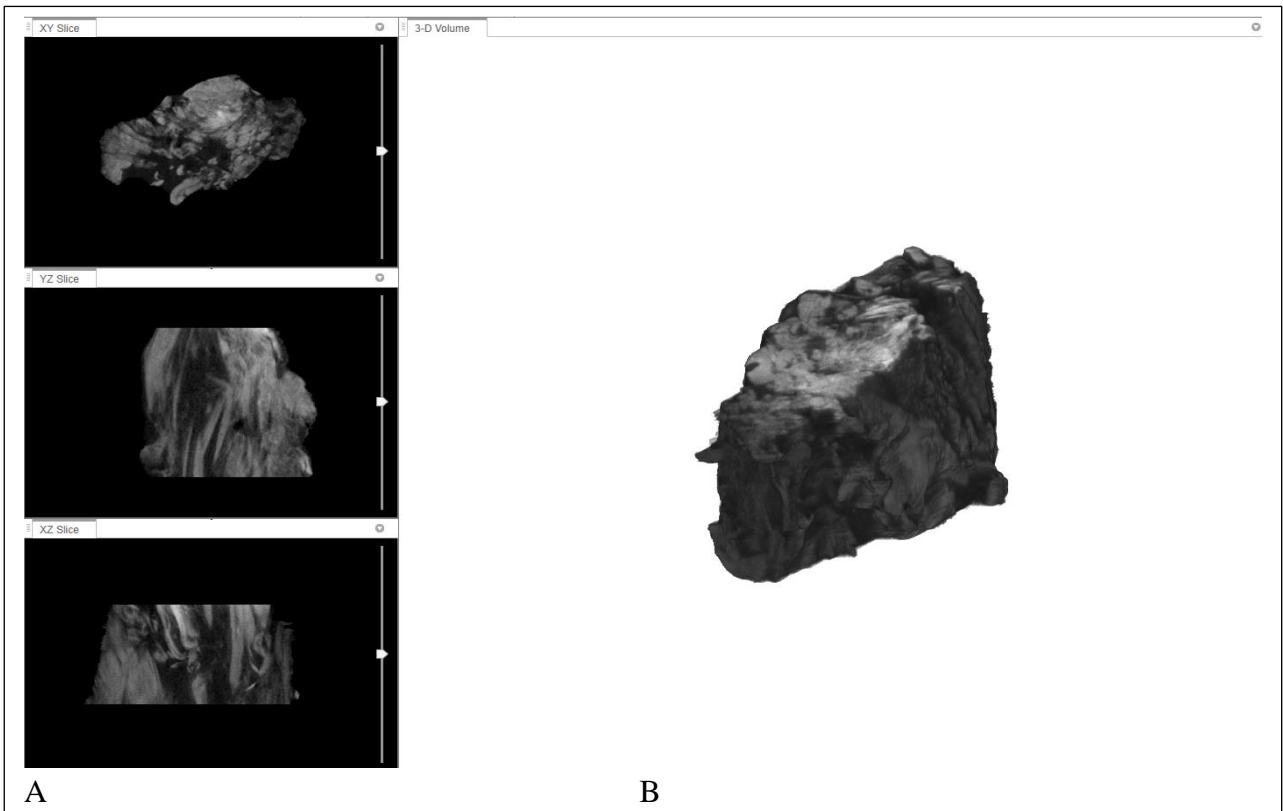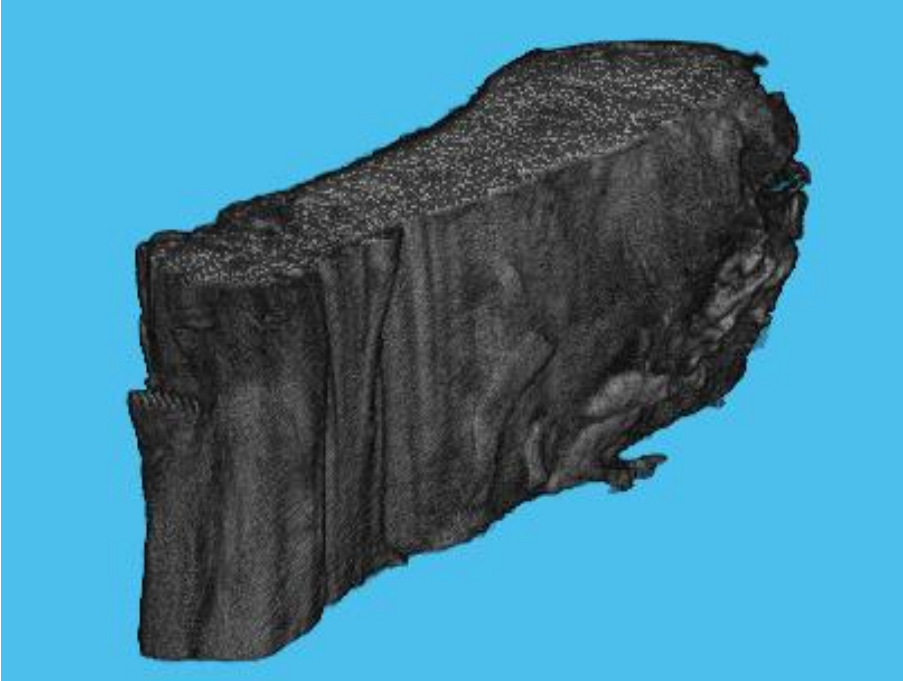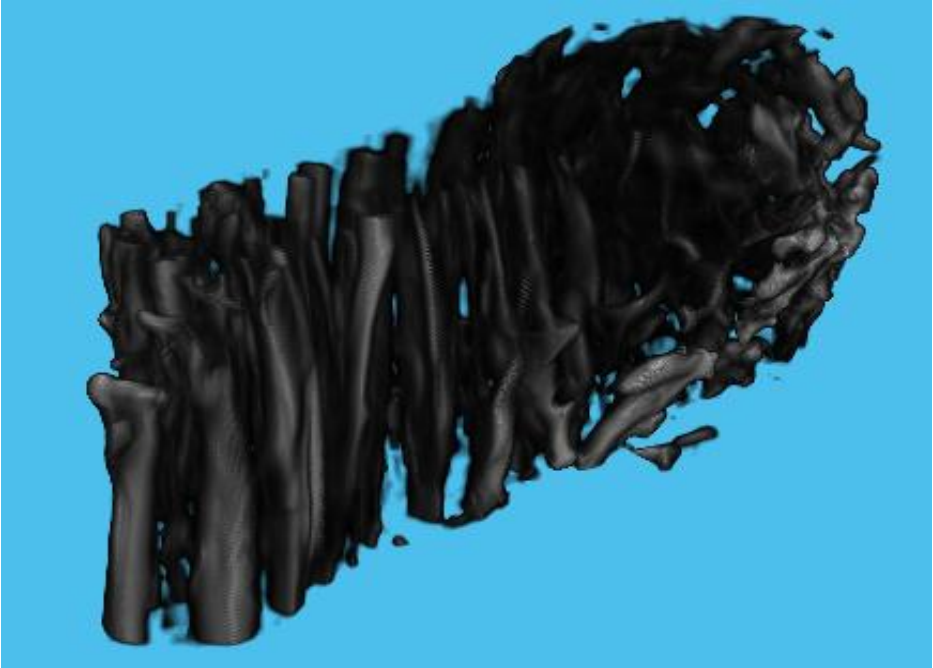

Figure 5. 29: Processed microCT image of the pathological specimen: (A) 2D view of the middle slice in XY, YZ, and XZ plane. (B)3D volume rendering.

3D Hessian -based multiscale filtering was applied for the processed 3D volume images. Figures (5.30 A and 5.31 A) illustrate the 3D rendering of the processed images, while Figures (5.30 B and 5.31 B) show the enhanced microstructures.
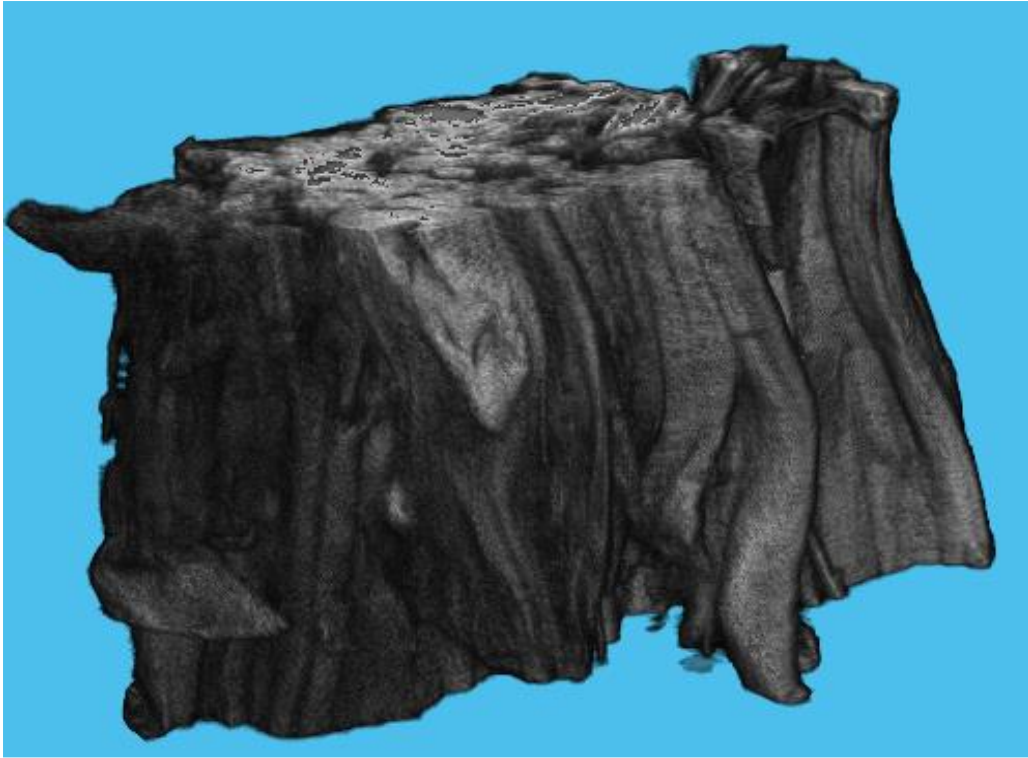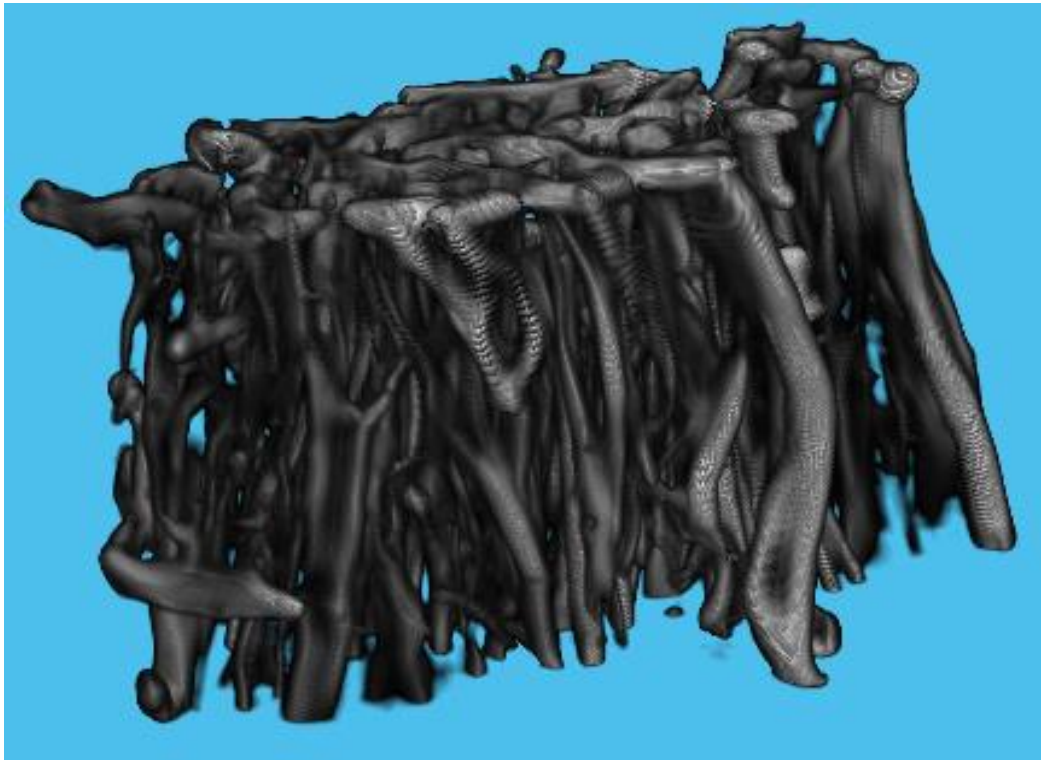

(A)

(B)

Figure 5. 30: 3D rendering of the healthy ACL at T0 (A) processed volume, and (B) Hessian enhancement volume.

(A)

(B)

Figure 5. 31: 3D rendering of the pathologic ACL at T0 (A) Processed volume, and (B) Hessian enhancement.

5.2.2 Feature extraction

At every strain level, the features of volume, diameter and orientation were estimated, as previously described. These morphological feature parameters are displayed using a histogram distribution with corresponding strain level (T0 to T8), as highlighted in figures (5.32, 5.33, 5.34, and 5.35).

Figures (5.32 and 5.33) illustrate the diameter distribution from T0 to T8 for both healthy ACL sample and pathological ACL sample. It has been clear that the diameter of fascicles is distributed between 0.05 to 0.2 mm for both samples. In addition, the number of fascicles with a small diameter increase proportionally with the strain level.

Figure 5. 32: Diameter distribution for the healthy ACL sample among T0 to T8.
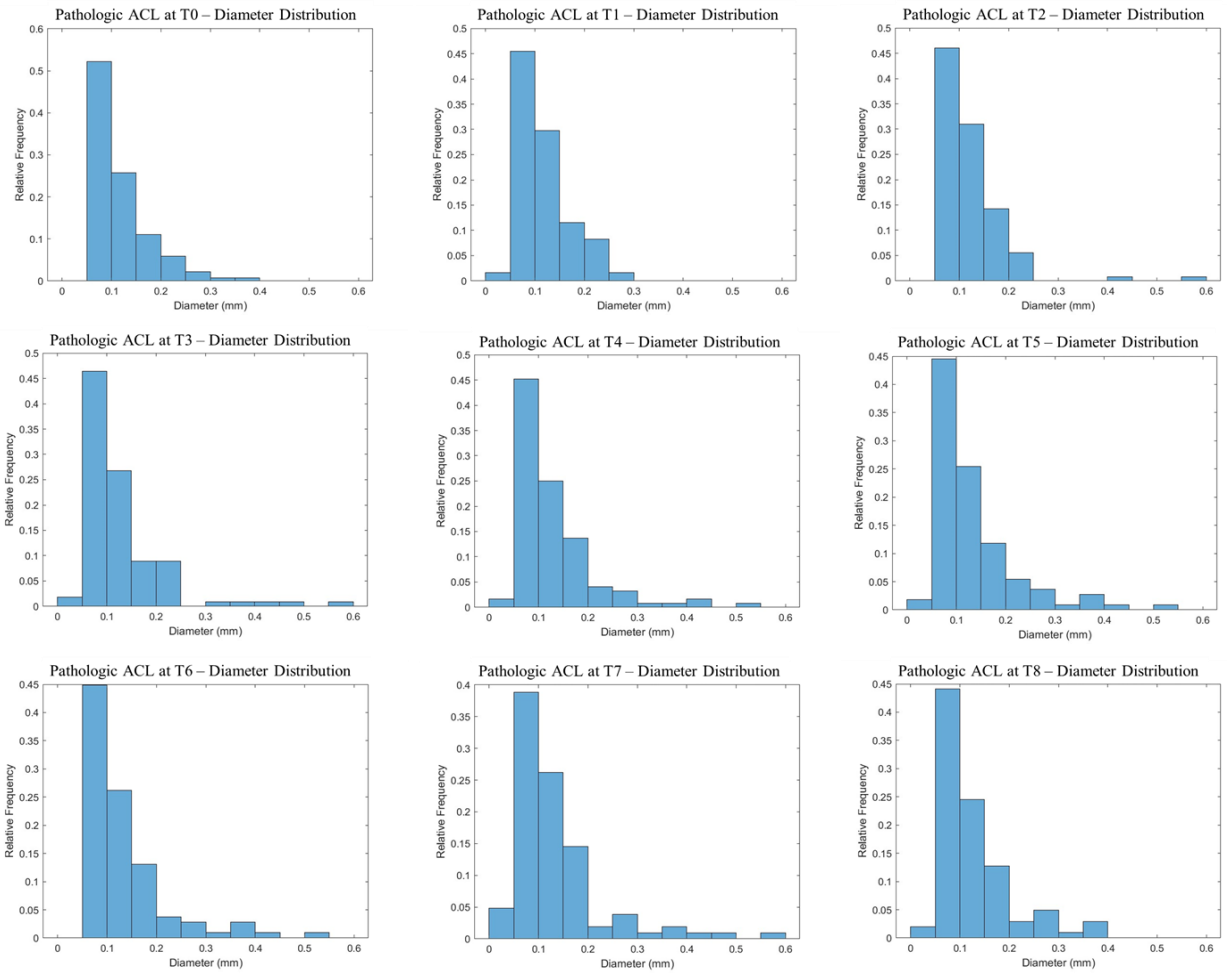
Figure 5. 33: Diameter distribution for the pathologic ACL sample among T0 to T8.

Figures (5.34 and 5.35) illustrate the orientation distribution from T0 to T8 for both healthy ACL sample and pathological ACL sample. It has been clear that the most of fascicles are aligned well to longitudinal axis for the healthy sample more than the pathologic sample. In addition, some objects misinterpreted as fascicles are distributed away from the longitudinal axis (20° to 90°). To overcome these issues, we excluded the smallest objects interpreting them as artefacts.
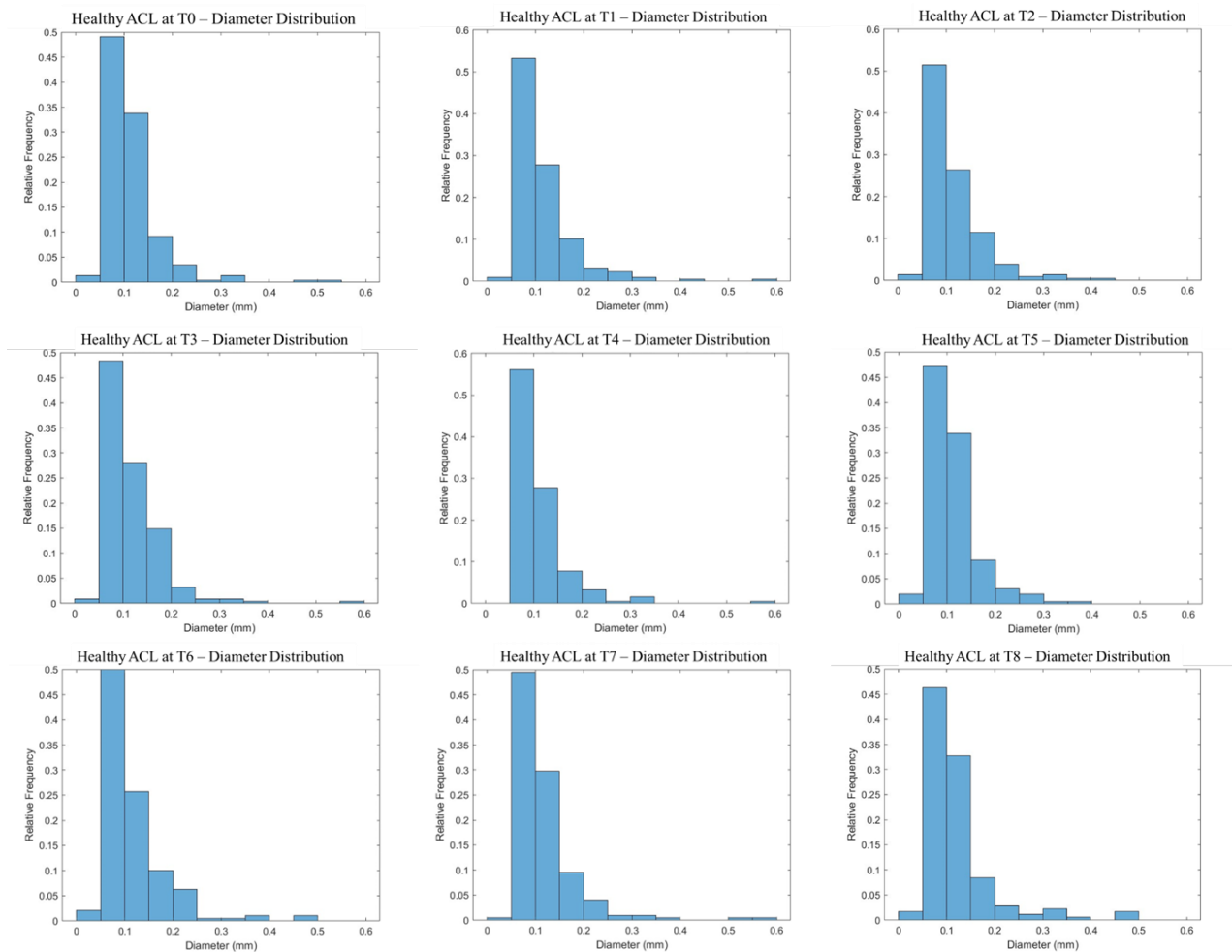
.
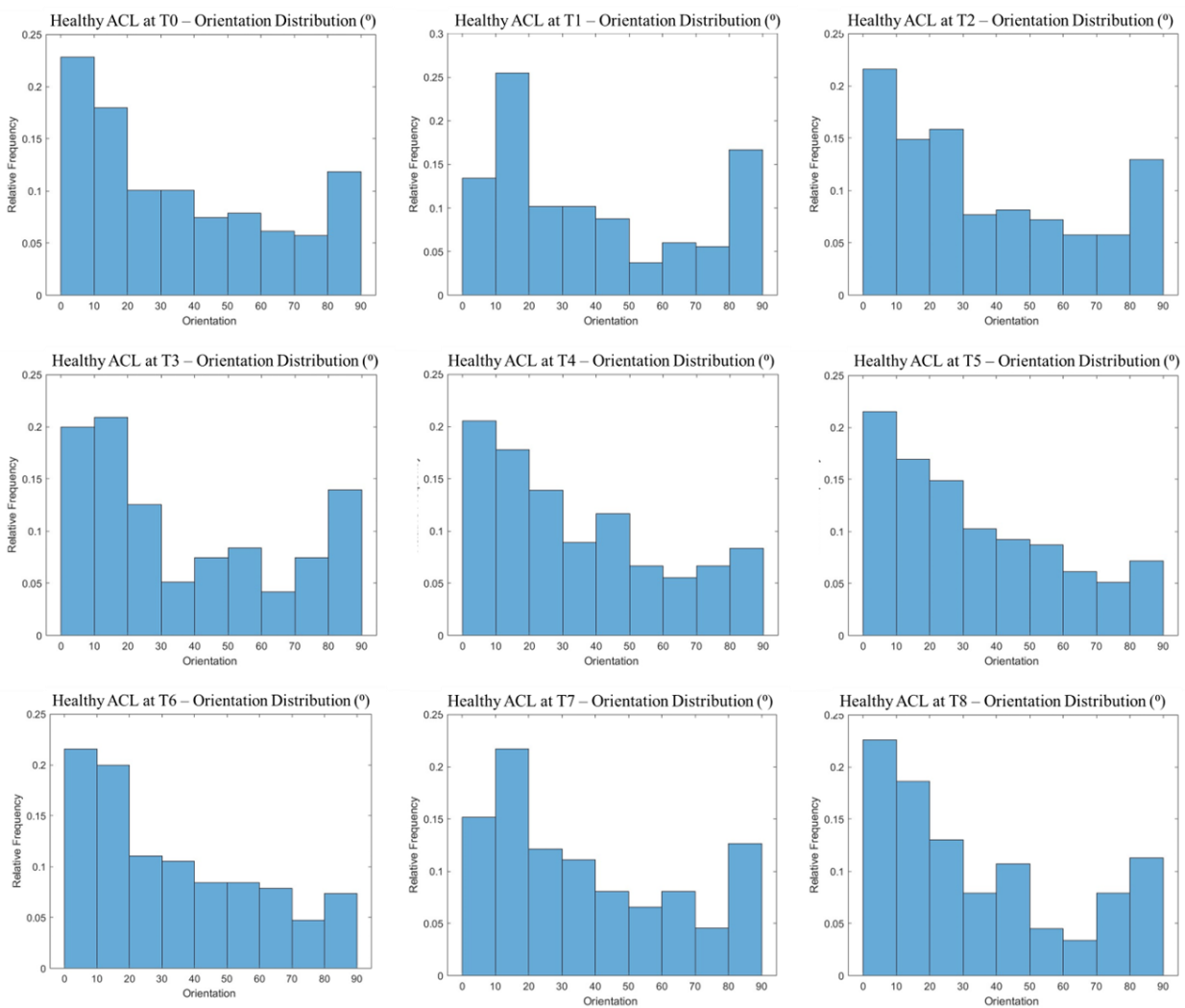
Figure 5. 34: Orientation distribution for the healthy ACL sample among T0 to T8.
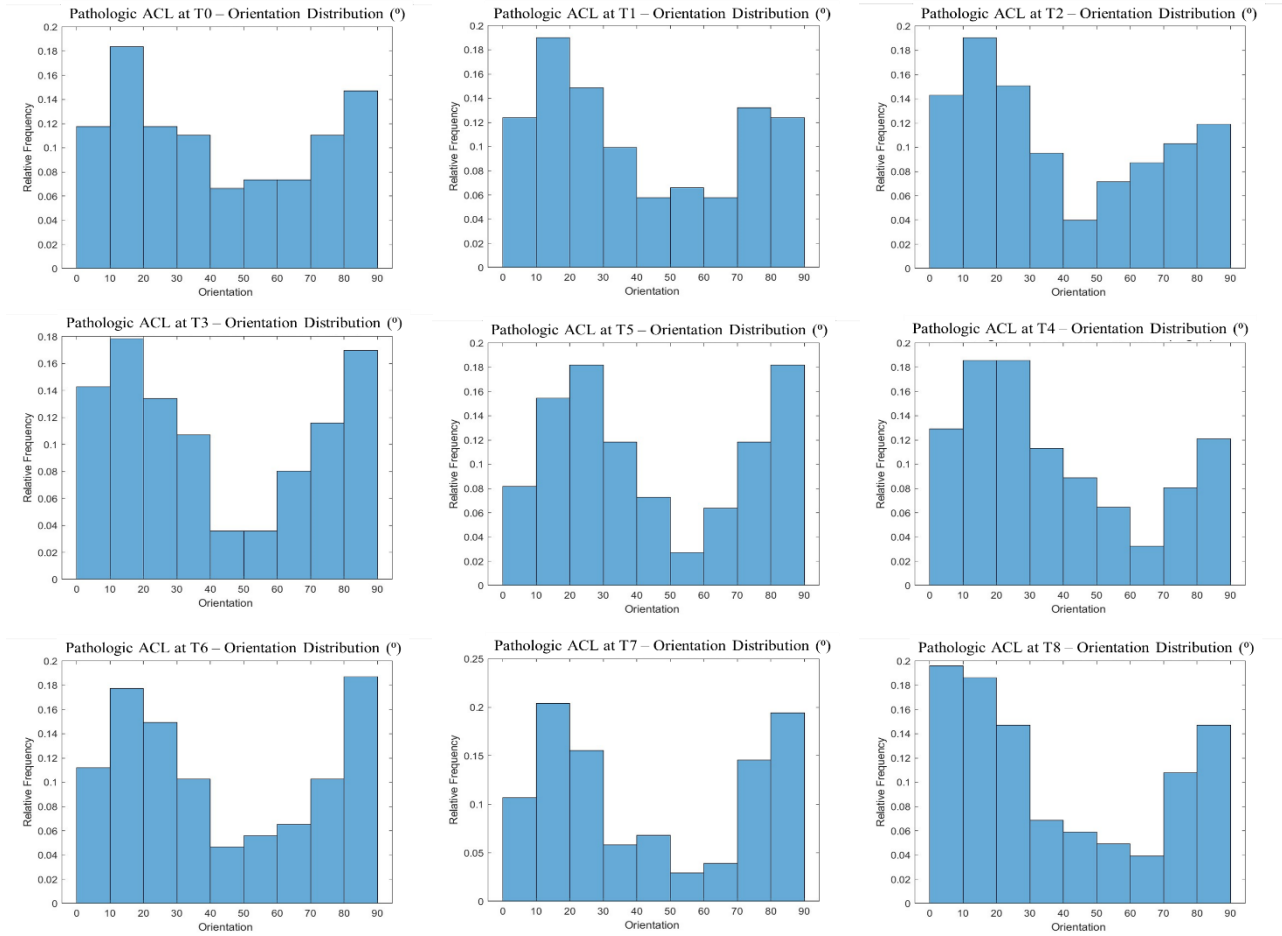
Figure 5. 35: Orientation distribution for the pathologic ACL sample among T0 to T8.

5.2.3 Statistical analysis

Statistics are used in this work are the variance of fascicles diameter and the entropy and energy of fascicles orientation.

The line chart in figure (5.36) illustrates the variance of the fascicle diameter distribution in different strain levels from T0 to T8 measured in mm. Overall, fascicle diameter has shown variance increasing with increasing strain levels. Healthy ACL presented less variance than the pathological one.

Regarding healthy ACL, the variance of fascicle diameters at T0 without any loading is about 0.1 mm. Then the variance increased dramatically at loads T1 and T2, while it decreased in the pathological sample at the same loads. In the healthy sample, the diameter remained stable from T2 to T4, when values began to increase again. On the

other hand, the diameter increased dramatically at T4 before decreasing again at T7 and T8.

In contrast, high variance indicates that fascicles are spread out and away from the mean. The variance in the pathologic ACL reaches its highest value at T6, which is approximately 0.28 mm and 0.2 mm in the pathological and healthy samples, respectively.

In conclusion, we can see that the diameter variance in the healthy specimen throughout the whole applied strain is always smaller than the pathological one. Interestingly, the diameter variance can indicate the fascicle progressive alignment with increasing strain.
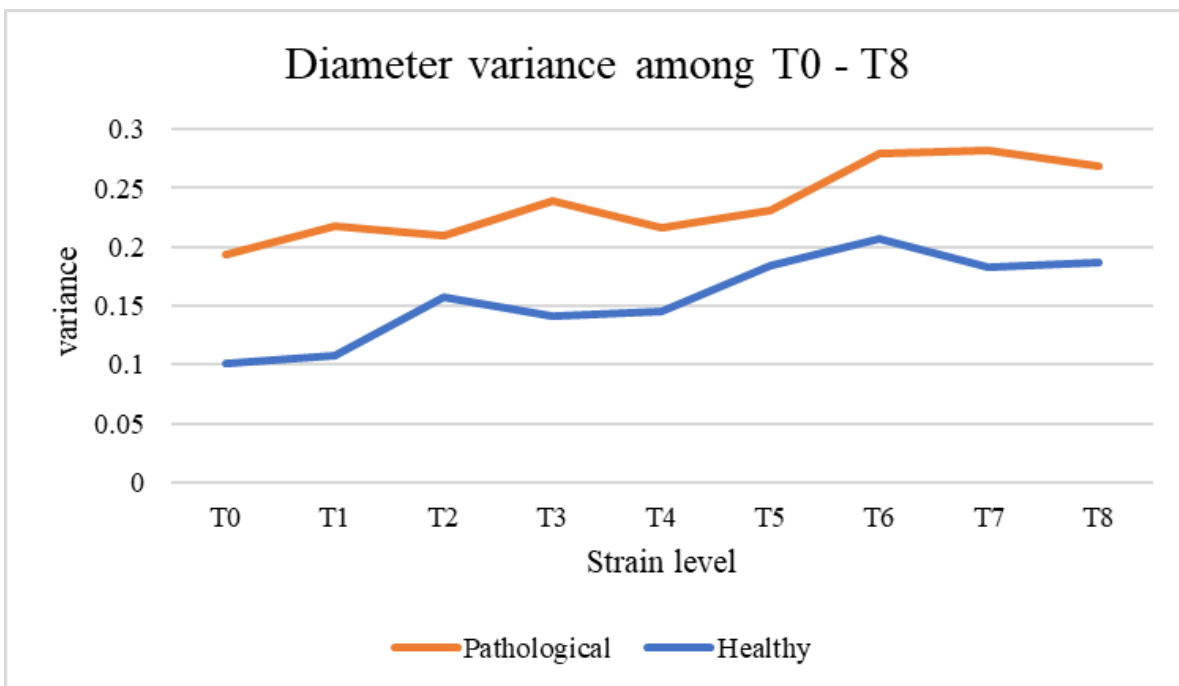
Figure 5. 36: The variance of fascicles diameters measures in (mm) of the healthy and pathologic ACL.

Figures (5,37 and 5.38) show the entropy and the energy of the orientation for both samples. The entropy measures the randomness of the fascicles orientation distribution whereas the energy represents the homogeneity.

Overall, the fascicle orientation has shown decreases in entropy with the increasing strain levels. Thus, it indicates the improved alignment of the fascicles concerning the longitudinal axis with progressive the strain rates.
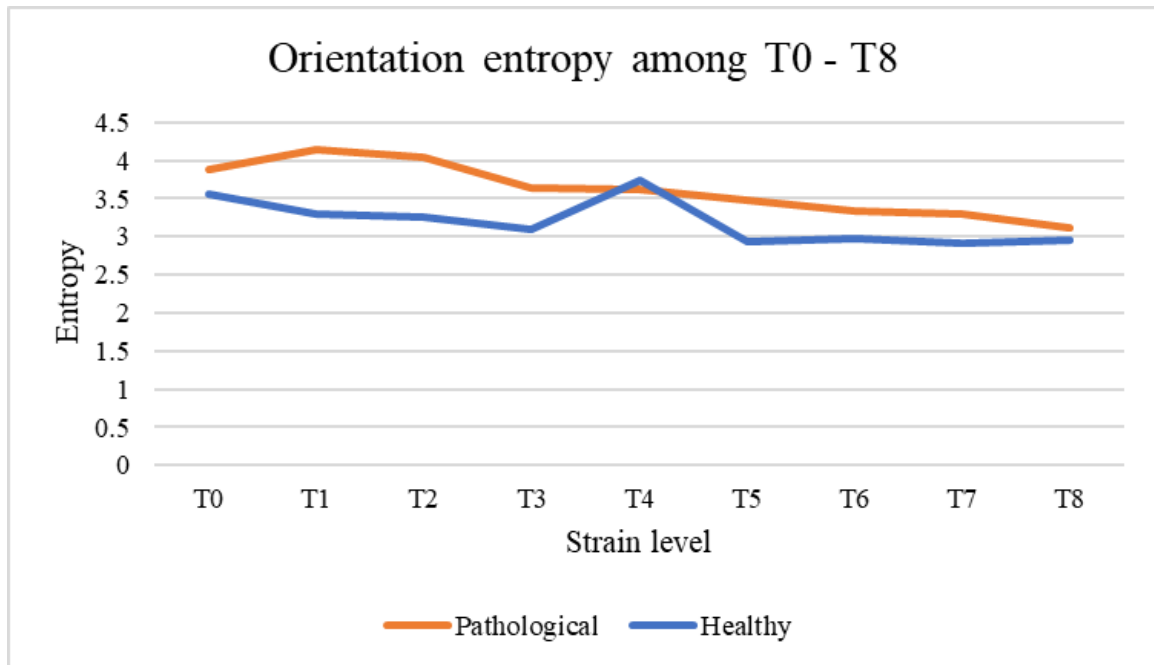

Figure 5. 37: The energy of the fascicles orientation of the healthy and pathologic ACL.
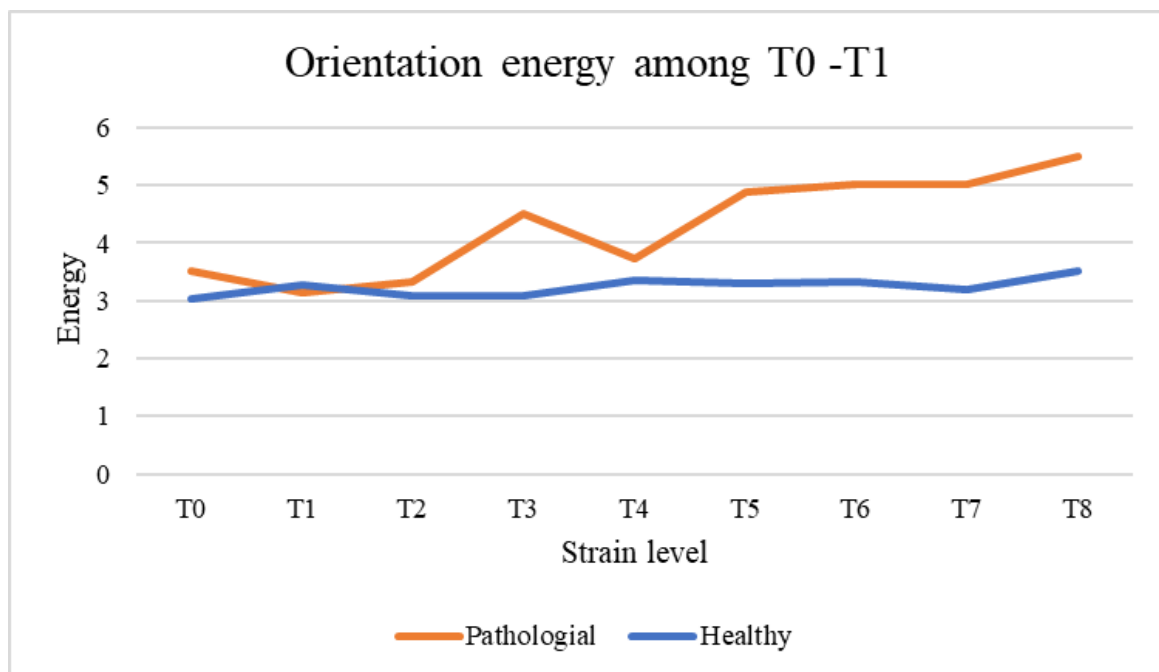

Figure 5. 38: The energy of the fascicles orientation of the healthy and pathologic ACL.

Normal sample entropy values are low, while abnormal sample entropy values are high. With respect to the healthy ACL, the entropy value reaches the peak at T4 and decreases to the value of 0.5 at T5. The trend remains steady after T5, see Figure (5. 37).

On the other hand, the energy values remain stable in the healthy specimen throughout the whole applied strain, while in the abnormal sample, they fluctuate among the levels T0 and T5; after this level, energy is stable see, Figure (5. 38).

In conclusion, entropy can discriminate between the normal and abnormal status while the energy is not before the T2 strain level.

5.2.4 Stress-strain relationship

An increase in extensional deformation from T0 to T8 was applied to evaluate the mechanical characteristics of healthy and pathologic ACL tissue. Fibres/fascicles orientation distribution functions can be used to calculate the effective elastic properties. In this case, we used weighted orientation instead of orientation. This can be achieved through the volume fraction for each orientation interval. For example, at 0^0 to 10^0 orientation intervals, the volume fraction can be calculated by dividing each fascicle volume by the total volume of the fascicle contribution in this interval.

Stress is estimated using the microstructural model and the constitutive law presented at paragraph 4.3.4. Figures (5.39 and 5.40) show the strain-stress relationship of the healthy and the pathologic ACLs.

A stress-strain curve of ACL structure under tensile loading can have: in the X-axis the percentage of deformation (elongation) expressed as strain and , or the axial stretch ratio (figures 5.39 and 5.40), in agreement with constitutive laws (paragraph 4.3.4; in the Y-axis the stress, or load per unit of area (MPa), which refers to the tensile strength of the tissue. A modulus of elasticity (N/mm^2 or MPa) is obtained from the linear slope of the stress-strain curve between two limits of strain (deformation). The toe

region represents "un-crimping" of the collagen fibrils; toe region ends at about 5% of strain, when all crimpled fibers straighten.
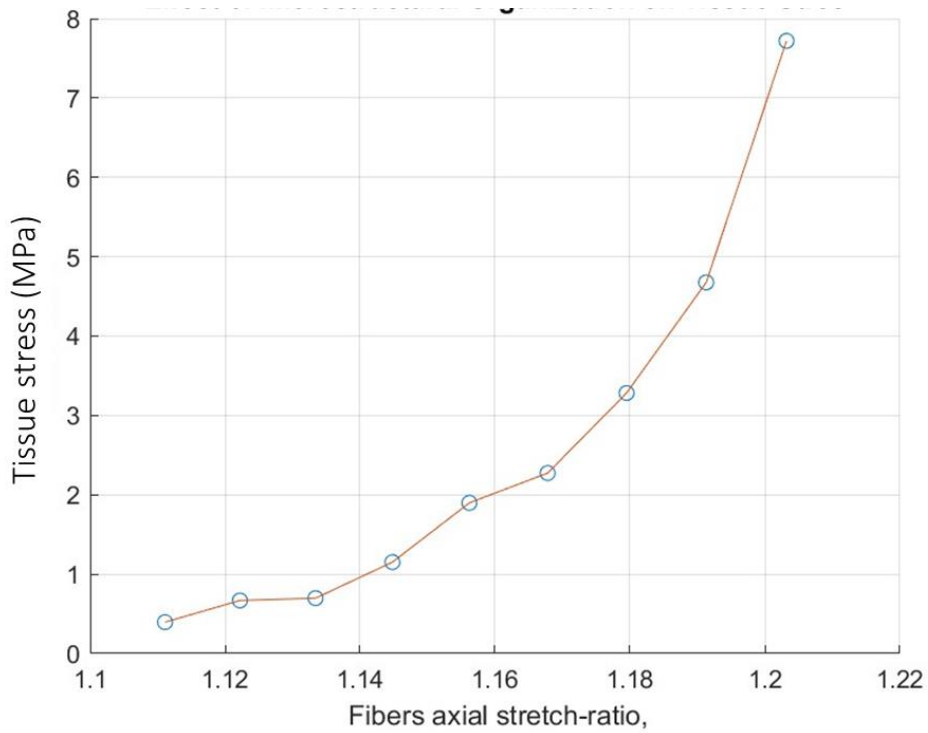
Figure 5. 39: Stress-strain curve of the healthy ACL. Modulus (E_f) is represented by the slope of the curve.
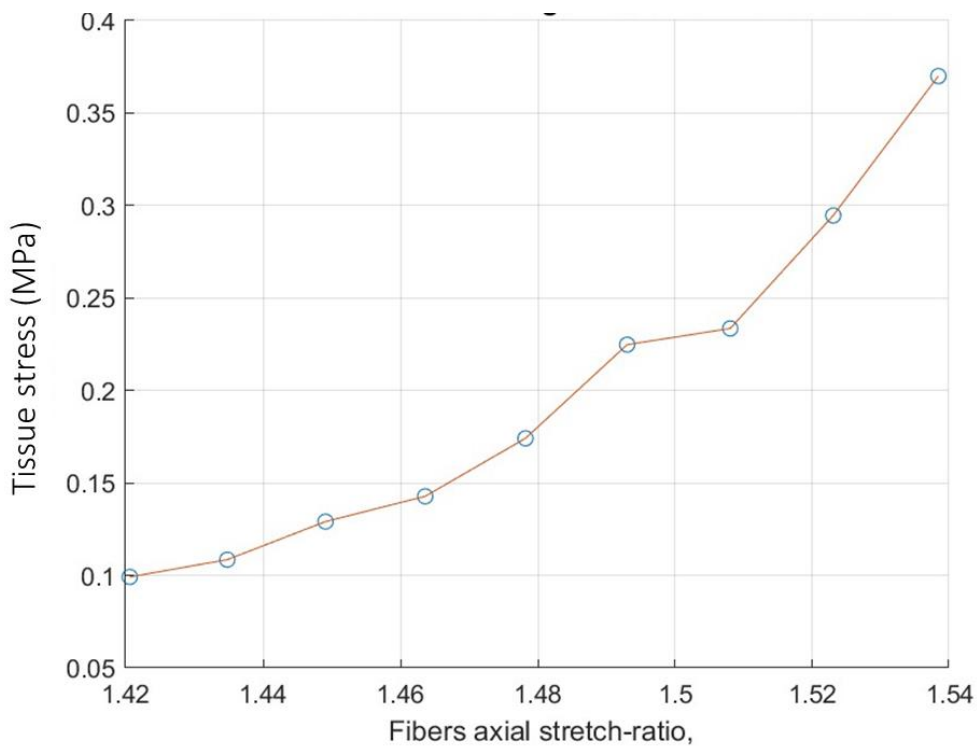
Figure 5. 40: Stress-strain curve of the pathologic ACL. Modulus (E_f) is represented by the slope of the curve.

Table 5.1 illustrates the elastic modulus (E_f) extracted for the healthy and the pathologic sample. E_f of the healthy ACL resulted 60.8 MPa. This value is close to values reported in other studies (123 MPa of ACL fibres [68], 100 to 360 MPa, [69], nevertheless, our method allows determination of E_f for each individual bundle, for both healthy and unhealthy ACL based on image processing algorithms applied to microCT images scanning each strain levels. Moreover, we estimated E_f of the fiber/fascicle scale while other research focused on fibrils (the Bovine Achilles tendon collagen type I presented an elastic modulus of 14.7 GPa (order of nm) in [70], and of 5.9 GPa, in [71]).

Table 5.1 Model elastic modulus comparison between healthy ACL and pathologic ACL

Tissue	Elastic module (MPa)
Health ACL	60.8
Pathologic ACL	7.7

6 CONCLUSIONS AND RECOMMENDATIONS

MicroCT represents an effective tool for detecting 3D features within fibrous tissues. Such an approach could readily be applied to image the effect of development, disease, or damage and repair in ligaments and tendons, as well as in collagen-rich fibrous tissue- engineered constructs.

In this study, we demonstrate the capability of the microCT to resolve the internal microscale morphology of contrast-enhanced tendons and ligaments. In other words, we proposed a new integrated approach for analysing tendons and ligaments both quantitatively – by identifying geometrical features - and qualitatively. Additionally, we implemented and deployed a mechanical constitutive model for the ACL and evaluated specific biomechanical characteristics of both healthy and pathologic samples.

In the first case study, where we implemented the CE-microCT approach, chemical staining together with proper image processing was demonstrated to facilitate the discrimination between different aspects of soft fibrous tissues and this enables quantitative measurement of fibre alignment and diameter. Therefore, to visualize and quantify differences in the 3D internal structure of tendons and ligaments, we used microCT imaging to identify key geometrical differences in the arrangement of fascicles within human hamstring tendon and bovine collateral ligament that had either been treated through chemical dehydration or 2% of PTA staining in two solutions: water (H_2O) and 70% ethanol (EtOH). Several factors must be considered when determining optimal staining technique, including contrast agent type, staining times and tissue type. PTA provided adequate contrast for identifying fascicular microstructure in hamstring tendon and bovine collateral ligament through microCT acquisition, so as to allow 3D visualizations and obtain quantitative information about sample structural features. On the other hand, sample drying using the HMDS protocol, as here presented, highlighted a fibrous microstructure as well, although it resulted less

specific with respect to collagen. Furthermore, qualitative validation via histological images highlighted good reliability of the proposed approach, nevertheless more research into using digital image processing techniques to better identify 3D fascicular microstructures is recommended, so as to obtain proper and reliable quantitative information.

According to the second case study, we implemented a proper application of the integrated approach; we illustrated that micro-scale resolutions can be achieved by imaging fixed soft tissues subjected to varying loading conditions, specifically of the healthy and pathological ACL. By analyzing the orientation and diameter of the fascicles, it is possible to understand how ACL tissue structure and function change with stress. We proposed a general structural mathematical stress-stretch model for ligament mechanical response. This model will be particularly useful in helping to understand how changes in fibrous structure (e.g., disease or treatment) affect ligament mechanical response.

The implemented stress-strain model has some limitations that need to be addressed in the next work. The main limitation is that this model assumes tissue volume in a complete fibers uncrimping configuration. Indeed, starting hypothesis is that the strain stress curve's toe region was covered by preload before microCT acquisition. However, experimental data showed that the final part of the toe region is still present, so the model should be updated in future work integrating fiber recruitment.

To simplify the constitutive equation, we assumed a discrete orientation value of the fibers rather than a continuous one [21]. For example, all fibers have an orientation between 0 and 10 in one interval, 10 and 20 in another, etc. Therefore, each object (i.e., fiber) orientation should be considered to overcome this issue (use integral instead of summation).

The stress in the tissue was calculated by summing the contributions of each fiber in the cross-section of the tissue volume. Thus, the obtained stress depends on how

objects (i.e., fibers) are segmented, resulting in an imprecise identification of parameters.

In the area of fiber extraction from microCT images, there are some open research issues. Firstly, in the current work we were focused on well-defined fibers, therefore we lost some information regarding fibers that are not evident to follow (maybe due to some noise or resolution limitations). Secondly, when the fiber density is very high, two fibers may be aligned perfectly on a line, and be mistakenly merged into one fiber by the break-merge method. Thirdly, the resolution and contrast issue may pose an additional challenge to extract fibers from the background of the microCT image. In such settings, it is imperative to investigate how to segment fibers accurately and extract morphological information. Finally, the merged fascicles are generally located on the sample edges, whereas the disconnected ones appear on the sample core where the intensity values are low due to contrast agent absorption inhomogeneity. Therefore, the lack of quality data, i.e., noisy data and incomplete data, influences our result, which are essential for the algorithm to build accurate and reliable model.

Artificial Intelligence (AI) algorithms could be effective in detecting fibers or fascicles; however, they need to be trained, and they would need access to a lot of data in order to become efficient.

To conclude, the CE-microCT approach here presented represents an important tool for developing an understanding of geometrical differences in the arrangement of fibers in ligament and tendon. In a peculiar application to ACL, the information obtained with the protocol was used to implement a mechanical model of fibrous tissues, thus estimating the biomechanical behaviour of the healthy and pathological tissues.

References

[1] Asahara, Hiroshi, Masafumi Inui, and Martin K. Lotz. "Tendons and ligaments: connecting developmental biology to musculoskeletal disease pathogenesis." *Journal of Bone and Mineral Research* 32.9 (2017): 1773-1782

[2] Moshiri, A., and A. Oryan. "Tendon and ligament tissue engineering, healing and regenerative medicine." J Sports Med Doping Stud 3.2 (2013): 126.

[3] Frank, Cyril B. "Ligament structure, physiology and function." *Journal of Musculoskeletal and Neuronal Interactions* 4.2 (2004): 199.

[4] Kirkendall, D. T., and W. E. Garrett. "Function and biomechanics of tendons." *Scandinavian journal of medicine & science in sports* 7.2 (1997): 62-66.

[5] Martin, R. Bruce, et al. "Mechanical properties of ligament and tendon." *Skeletal tissue mechanics*. Springer, New York, NY, 2015. 175-225.

[6] Benjamin, M., and J. R. Ralphs. "Invited Review Tendons and ligaments-an overview." *Histol Histopathol* 12 (1997): 1135-1144.

[7] Kannus, Pekka. "Structure of the tendon connective tissue." Scandinavian journal of medicine & science in sports 10.6 (2000): 312-320.

[8] Chiverton, John P., et al. "Automatic diameter and orientation distribution determination of fibrous materials in micro–X-ray CT imaging data." Journal of microscopy 272.3 (2018): 180-195

[9] McLean, James P., et al. "High-speed collagen fiber modeling and orientation quantification for optical coherence tomography imaging." Optics Express 27.10 (2019): 14457-14471.

[10] Shearer, Tom, et al. "Three-dimensional visualisation of soft biological structures by X-ray computed micro-tomography." *Journal of cell science* 129.13 (2016): 2483-2492.

[11] Gignac, Paul M., et al. "Diffusible iodine-based contrast-enhanced computed tomography (diceCT): an emerging tool for rapid, high-resolution, 3-D imaging of metazoan soft tissues." Journal of anatomy 228.6 (2016): 889-909.

[12] Heimel, Patrick, et al. "Iodine-enhanced microCT imaging of soft tissue on the example of peripheral nerve regeneration." Contrast Media & Molecular Imaging 2019 (2019).

[13] Gaspar, Branislav, et al. "Micro-Computed Tomography Soft Tissue Biological Specimens Image Data Visualization." Applied Sciences 12.10 (2022): 4918.

[14] de Bournonville, Sébastien, Sarah Vangrunderbeeck, and Greet Kerckhofs. "Contrast-enhanced MicroCT for virtual 3D anatomical pathology of biological tissues: a literature review." *Contrast media & molecular imaging* 2019 (2019).

[15] Kestilä, Iida, et al. "Three-dimensional microstructure of human meniscus posterior horn in health and osteoarthritis." Osteoarthritis and cartilage 27.12 (2019): 1790-1799.

[16] Balint, Richard, Tristan Lowe, and Tom Shearer. "Optimal contrast agent staining of ligaments and tendons for X-ray computed tomography." PloS one 11.4 (2016): e0153552.

[17] Jehoon, O., et al. "Use of micro-X-ray computed tomography with phosphotungstic acid preparation to visualize human fibromuscular tissue." JoVE (Journal of Visualized Experiments) 151 (2019): e59752.

[18] Marchiori, G., et al. "Integration of microCT and uniaxial loading to analyse the evolution of 3D microstructure under increasing strain: application to the anterior cruciate ligament." Materials Today: Proceedings 7 (2019): 501-507.

[19] Lim, Wei Lee, et al. "Current progress in tendon and ligament tissue engineering." Tissue engineering and regenerative medicine 16.6 (2019): 549-571.

[20] Marieswaran, M., et al. "A review on biomechanics of anterior cruciate ligament and materials for reconstruction." Applied bionics and biomechanics 2018 (2018).

[21] Hurschler, C., B. Loitz-Ramage, and R. Vanderby Jr. "A structurally based stress-stretch relationship for tendon and ligament." (1997): 392-399.

[22] Merveille, Odyssée, et al. "Tubular structure filtering by ranking orientation responses of path operators." European Conference on Computer Vision. Springer, Cham, 2014.

[23] Sartori, Julian, et al. "Three-dimensional imaging of the fibrous microstructure of Achilles tendon entheses in Mus musculus." Journal of Anatomy 233.3 (2018): 370-380.

[24] Ribitsch, Iris, et al. "Structure—Function relationships of equine menisci." PLoS One 13.3 (2018): e0194052.

[25] Clark, Jeffrey N., et al. "Propagation phase-contrast micro-computed tomography allows laboratory-based three-dimensional imaging of articular cartilage down to the cellular level." Osteoarthritis and cartilage 28.1 (2020): 102-111.

[26] Disney, C. M., et al. "Visualising the 3D microstructure of stained and native intervertebral discs using X-ray microtomography." Scientific reports 7.1 (2017): 16279.

[27] Karhula, Sakari S., et al. "Effects of articular cartilage constituents on phosphotungstic acid enhanced micro-computed tomography." PloS one 12.1 (2017): e0171075.

[28] Ravagli, Enrico, et al. "Imaging fascicular organization of rat sciatic nerves with fast neural electrical impedance tomography." Nature Communications 11.1 (2020): 6241.

[29] Beisbayeva, Zhuldyz, et al. "Change in collagen fibril diameter distribution of bovine anterior cruciate ligament upon injury can be mimicked in a nanostructured scaffold." Molecules 26.5 (2021): 1204.

[30] Chakraborty, Souvik, Debabrata Mondal, and Mohammad Motalab. "Constitutive modeling of the human Anterior Cruciate Ligament (ACL) under uniaxial loading using viscoelastic prony series and hyperelastic five parameter Mooney-Rivlin model." AIP Conference Proceedings. Vol. 1754. No. 1. AIP Publishing LLC, 2016.

[31] Wan, Chao, Zhixiu Hao, and Shizhu Wen. "The effect of the variation in ACL constitutive model on joint kinematics and biomechanics under different loads: a finite element study." Journal of biomechanical engineering 135.4 (2013).

[32] De Vita, Raffaella, and William S. Slaughter. "A structural constitutive model for the strain rate-dependent behavior of anterior cruciate ligaments." International Journal of Solids and Structures 43.6 (2006): 1561-1570.

[33] Pioletti, Dominique P., et al. "Viscoelastic constitutive law in large deformations: application to human knee ligaments and tendons." Journal of biomechanics 31.8 (1998): 753-757.

[34] Nordin, Margareta, and Victor Hirsch Frankel, eds. Basic biomechanics of the musculoskeletal system. Lippincott Williams & Wilkins, 2001.

[35] Kjaer, Michael. "Role of extracellular matrix in adaptation of tendon and skeletal muscle to mechanical loading." Physiological reviews 84.2 (2004): 649-698.

[36] Zhang, Shichen, et al. "Hierarchical ultrastructure: An overview of what is known about tendons and future perspective for tendon engineering." Bioactive Materials 8 (2022): 124-139.

[37] Benjamin, M., E. Kaiser, and S. Milz. "Structure-function relationships in tendons: a review." Journal of anatomy 212.3 (2008): 211-228.

[38] Citeroni, Maria Rita, et al. "In vitro innovation of tendon tissue engineering strategies." International Journal of Molecular Sciences 21.18 (2020): 6726.

[39] Amiel, D., et al. "Tendons and ligaments: a morphological and biochemical comparison." Journal of Orthopaedic Research 1.3 (1983): 257-265.

[40] Snell, Richard S. Clinical and functional histology for medical students. Little, Brown Medical Division, 1984

[41] Woo, Savio L-Y., et al. "Injury and repair of ligaments and tendons." Annual review of biomedical engineering 2.1 (2000): 83-118.

[42] Dourte, LeAnn M., Andrew F. Kuntz, and Louis J. Soslowsky. "Twenty-five years of tendon and ligament research." Journal of Orthopaedic Research 26.10 (2008): 1297-1305.

[43] Woo, SL-Y. "Anatomy, biology, and biomechanics of tendon, ligament, and meniscus." Orthopaedic basic science (1994): 45-88.

[44] Fung, Y. C. "Elasticity of soft tissues in simple elongation." American Journal of Physiology-Legacy Content 213.6 (1967): 1532-1544.

[45] Viidik, A. "Elasticity and tensile strength of the anterior cruciate ligament in rabbits as influenced by training." Acta Physiologica Scandinavica 74.3 (1968): 372-380.

[46] Silver, Frederick. Biomaterials, Medical Devices and Tissue Engineering: An Integrated Approach: An Integrated Approach. Springer Science & Business Media, 1993.

[47] Kennedy, J. C., et al. "Tension studies of human knee ligaments. Yield point, ultimate failure, and disruption of the cruciate and tibial collateral ligaments." *JBJS* 58.3 (1976): 350-355.

[48] Noyes, Frank R., and Edward S. Grood. "The strength of the anterior cruciate ligament in humans and Rhesus monkeys." JBJS 58.8 (1976): 1074-1082.

[49] Rafael C. González, Richard Eugene Woods (2007). Digital Image Processing. Prentice Hall. p. 85. ISBN 978-0-13-168728-8.

[50] Thorpe, Chavaunne T., et al. "Tendon physiology and mechanical behavior: structure–function relationships." *Tendon regeneration*. Academic Press, 2015. 3-39.

[51] Frangi, Alejandro F., et al. "Multiscale vessel enhancement filtering." International conference on medical image computing and computer-assisted intervention. Springer, Berlin, Heidelberg, 1998.

[52] Orłowski, Piotr, and Maciej Orkisz. "Efficient computation of Hessian-based enhancement filters for tubular structures in 3D images." Irbm 30.3 (2009): 128-132.

[53] Lorenz, Cristian, et al. "Multi-scale line segmentation with automatic estimation of width, contrast and tangential direction in 2D and 3D medical images." CVRMed-MRCAS'97. Springer, Berlin, Heidelberg, 1997.

[54] Sato, Yoshinobu, et al. "Three-dimensional multi-scale line filter for segmentation and visualization of curvilinear structures in medical images." Medical image analysis 2.2 (1998): 143-168.

[55] Sato, Yoshinobu. "Hessian-based multiscale enhancement, description, and quantification of second-order 3-D local structures from medical volume data." Handbook of Biomedical Image Analysis. Springer, Boston, MA, 2005. 531-589.

[56] Jerman, Tim, et al. "Enhancement of vascular structures in 3D and 2D angiographic images." *IEEE transactions on medical imaging* 35.9 (2016): 2107-2118.

[57] Alharbi, Shuaa S., et al. "The multiscale top-hat tensor enables specific enhancement of curvilinear structures in 2D and 3D images." Methods 173 (2020): 3-15.

[58] Solomon, Chris, and Toby Breckon. Fundamentals of Digital Image Processing: A practical approach with examples in Matlab. John Wiley & Sons, 2011.

[59] Kestila I, Folkesson E, Finnila MA, Turkiewicz A, Onnerfjord P, Hughes V, et al. Three-dimensional microstructure of human meniscus posterior horn in health and osteoarthritis. Osteoarthritis and Cartilage 27(12):1790–1799, 2019.

[60] O J, Kwon HJ, Choi YJ, Cho TH, Yang HM. Three-dimensional structure of the orbicularis retaining ligament: an anatomical study using micro-computed tomography. Scientific Reports 8(1):1–8, 2018.

[61] NRecon Reconstruction Software - User Manual.

Luke Xie (2023). 3D structuring element (sphere), MATLAB Central File Exchange. Retrieved January 4, 2023, (https://www.mathworks.com/matlabcentral/fileexchange/47937-3d-structuring-element-sphere),

[62] Li, Jie, Mengda Zhang, and Yongpeng Gao. "Vessel segmentation of liver CT images by hessian-based enhancement." International Conference on Image and Graphics. Springer, Cham, 2019.

[63] Mishurova, Tatiana, et al. "Evaluation of the probability density of inhomogeneous fiber orientations by computed tomography and its application to the calculation of the effective properties of a fiber-reinforced composite." International Journal of Engineering Science 122 (2018): 14-29.

[64] Goh, Kheng Lim, Anne Listrat, and Daniel Béchet. "Hierarchical mechanics of connective tissues: Integrating insights from nano to macroscopic studies." Journal of biomedical nanotechnology 10.10 (2014): 2464-2507.

[65] Grassi, Alberto, et al. "Case Report: Anterior Cruciate Ligament Calcification in a Patient With Chondrocalcinosis: Micro-Computed Tomography Presentation." Frontiers in Surgery 8 (2021): 680234.

[66] Shearer, Tom, et al. "X-ray computed tomography of the anterior cruciate ligament and patellar tendon." Muscles, ligaments and tendons journal 4.2 (2014): 238.

[67] Longo, Antonia, et al. "Assessment of hessian-based Frangi vesselness filter in optoacoustic imaging." Photoacoustics 20 (2020): 100200.

[68] Orozco, Gustavo A., et al. "The effect of constitutive representations and structural constituents of ligaments on knee joint mechanics." Scientific reports 8.1 (2018): 2323.

[69] [Dutov, Pavel, et al. "Measurement of elastic modulus of collagen type I single fiber." PloS one 11.1 (2016): e0145711.

[70] Yang, Lanti, et al. "Micromechanical bending of single collagen fibrils using atomic force microscopy." Journal of Biomedical Materials Research Part A 82.1 (2007): 160-168.

[71] Yang, Lanti, et al. "Micro-tensile testing of individual native and cross-linked collagen type I fibrils." MECHANICAL PROPERTIES OF COLLAGEN FIBRILS AND ELASTIC FIBERS EXPLORED BY AFM (2008): 81.